Title
On the Future of Head-Based Microactuators in Hard Disk Drives

Author
Wernow, Josiah Natan

Publication Date
2012

Peer reviewed|Thesis/dissertation

On the Future of Head-Based Microactuators in Hard Disk Drives

By

Josiah Natan Wernow

A dissertation submitted in partial satisfaction of the

requirements for the degree of

Doctor of Philosophy

in

Engineering—Mechanical Engineering

in the

Graduate Division

of the

University of California, Berkeley

Committee in Charge:

Professor Roberto Horowitz, Chair
Professor Liwei Lin
Professor Yuri Suzuki

Spring 2012

On the Future of Head-Based Microactuators
in Hard Disk Drives

by

Josiah Natan Wernow

Abstract

On the Future of Head-Based Microactuators
in Hard Disk Drives

by

Josiah Natan Wernow

Doctor of Philosophy in Mechanical Engineering

University of California, Berkeley

Professor Roberto Horowitz, Chair

Dual-stage actuation is an important technology enabler for advancing hard disk drive capacity and performance. This thesis describes the ongoing trend of decreasing track pitches required for areal density growth and increasing disturbances arising from rising spindle speeds, demonstrating that future dual-stage actuators will need to overcome the bandwidth limitations faced by the current suspension-based devices. First, the state of the art for dual-stage actuation is presented in the form of a literature review. This is followed by an overview of a new servo-mechanical design and analysis technique which is a hybrid of Galerkin beam elements and optimal linear quadratic Gaussian control analysis. This new technique is used to demonstrate the potential performance benefits of head-based actuation over suspension-based actuation. With the driving goal of designing a new head-based actuator, the constraints posed by industry are presented and discussed in detail. This is followed by an overview of the various actuation mechanisms evaluated, including several electrostatic and piezoelectric devices. The two most significant challenges identified through this analysis are the introduction of a gap at the trailing edge of the air-bearing and the necessity to actuate traces with sufficiently high actuation force.

A quasi-shear mode piezoelectric actuator is proposed as a cost-effective head-based actuator which meets the given criteria and can be implemented at the wafer-scale. A new prototype was fabricated at the Berkeley Nanofabrication Laboratory with a measured bandwidth above 50 kHz. Since the proposed head-based actuation scheme requires a gap in the air-bearing surface, a second actuation mode is also presented. It is shown that the gap width between the slider body and read/write head can be controlled independently of track-following displacement in order to minimize pressure loss at the air-bearing surface. It is also shown that the directionality along each actuation mode of this device is greater that 1:10, although the resolution of measurement tools makes it difficult to determine how much greater the directionality is.

The two key figures of merit for this project are microactuator bandwidth and static displacement gain. For the prototype presented herein, the bandwidth is shown to be greater than 50 kHz, which is the highest frequency measurable by the available equipment. The static gain is measured to be approximately 1 nm/V. With sol-gel based stacking methods, however, the static gain could be scaled as high as 20 nm/V or more, although this will require further investigation by industry to develop. The intellectual merits of this project include a newly developed servo-mechanical design tool, modified beam equations with piezoelectric energy taken into account, and several new fabrication methods. The new fabrication methods include chemical mechanical polishing of PMN-PT, eutectic bonding of PMN-PT to silicon, scribing high aspect-ratio geometry in PMN-PT with a dicing blade, epoxy drop deposition with flipchip bonding, and fabrication of tall MEMS structures with sacrificial copper plating with a wet etch release.

To my parents, my leaders and my peers.

Contents

List of Figures

List of Tables

Acknowledgements

I am extremely grateful for the support I have received from my advisor, Roberto Horowitz, during the past five years while I have been in Berkeley. I have received excellent advice in my research, in my course work, and even more generally, with respect to life as a graduate student. I am grateful for the level of trust and care I have been given as a member of this research group. And I am grateful to my labmates, Sarah Felix, Richard Conway, Jianbin Nie, Deepan Raj Prabakar Muthirayan, Brian Phegley, Claus Danielson, Fu Zhang and Behrooz Shahsavari, for their collaboration, positive criticism, advice and for often lending a listening ear as I try to explain various challenges.

I am thankful for the members of the Computer Mechanics Laboratory (CML) for their assistance with various aspects of this project. Specifically, I have benefitted greatly from discussions with Shaomin Xiong and Liang Pan. I am also indebted to David Bogy and Dolf Mardan for their continual effort to maintain an open collaboration between industry and academia.

I am thankful to the industry sponsors who have contributed to this work through the CML and also to Western Digital for their special interest and financial support of this project. Additionally, I am grateful for the U.C. Discovery Grant which has provided a great deal of additional financial support. I am also indebted to Mark Bragen, who spear-headed this project, Nathan Emley, who provided bi-weekly advice and feedback, Nasir Jamil, for his assistance with mask design, and countless others for their tolerance and guidance of this project.

I would like to thank the Berkeley Microlab and Nanolab staff for their assistance and continued work to keep the lab running smoothly. Sia Parsa, Bob Hamilton and Matt Wasilik have been excellent sources of advice and direction. Danny Pestal has spent many hours repairing the flipchip bonder which has been so important for the final assembly step of this project. Joe Donnelly, Brian McNeill and Jay Morford have faithfully kept the sputtering and evaporation tools in excellent working condition with minimal down time. Overall, I am indebted to Bill Flounders and Katalin Voros for their relentless effort to keep these labs clean and safe with such a wide variety of projects and a broad spectrum of materials, processes and chemicals. I am also grateful to Joshua Chien and David Dornfeld from the Mechanical Engineering Department for their assistance with chemical mechanical polishing.

Finally, I grateful for support from my wife, my parents, sister, and grandparents, my brothers and sisters in IGSM, my leaders and peers, and especially, for Bernie Van Wie, Sunil Dwivedi, and Dave Turcic, who advised me to come to graduate school in the first place.

Thank you all,

Josiah Wernow

Chapter 1

Introduction

Dual-stage actuation is an important technology enabler for advancing hard disk drive (HDD) capacity and performance. This thesis begins with an introductory chapter motivating work in dual-stage actuation by summarizing past trends in HDD capacity and explaining the future roadmap for capacity and performance set by industry. The accompanying challenges posed to servo control in HDD's are discussed and head-based actuation is introduced as a higher bandwidth alternative to suspension-based dual-stage actuation. The remainder of this thesis will then be dedicated to designing, prototyping and testing a novel head-based actuator.

1.1 A New Era of Information Storage

For many thousands of years, people have stored information in written or printed form, often referred to as analog information storage. Indeed, it has been a very gradual transition from the primitive "tally sticks" [1] to Gutenberg's printing press [2]. In the span of just three decades, however, our world has been almost completely transformed from analog to digital information storage. A major study of 60 representative analog and digital technologies has catalogued a transition in the percentage of total information stored in a digital format from 0.8% in 1986 to 94% in 2007 [3].

Along with the digitization of information has come an accompanying growth in information storage capacity which is equally remarkable. This tremendous growth was documented with a worldwide capacity of 2.6 exabytes in 1986 to 295 exabytes in 2007 [4]. By 2007, over half of the total storage capacity was represented by HDD's. As of 2010, market research conducted by International Data Corporation (IDC) reported figures for total data storage capacity in the zettabyte range [5]. As seen in Fig. 1.1, these recent findings represent a 50% compound annual growth rate (CAGR), which is even higher than the 23% observed by Hilbert.

1.2 Kryder's Law

The only technologies which will be able to meet an ever-increasing demand for data-storage will be those which can effectively achieve exponential increases in capacity without accompanying increases in cost. This was the goal of Mark Kryder when he established the Magnetics Technology Center (MTC) in 1983 at the very start of the digital revolution [6]. For the HDD industry, the key to increasing storage capacity without increasing the cost was to set a technological roadmap for increasing the number of bits per square inch, also called areal density, which

prescribes an exponential growth curve that has often been referred to as “Kryder’s Law.” [6]

Since the invention of the very first commercial HDD in 1956, the IBM 305 RAMAC, the areal density has steadily risen at approximately 60% per year, which corresponds to the areal density doubling every 18 months, as shown in Fig. 1.2.

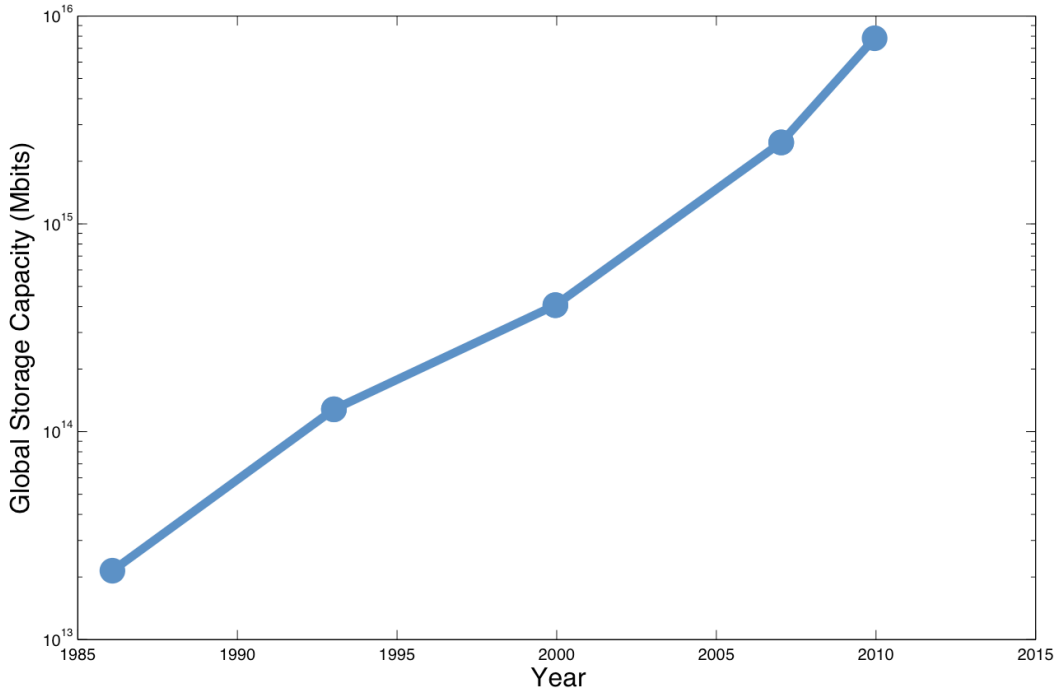

Figure 1.1: Since 1986, global storage capacity has grown at a rate of approximately 23% per year. Hilbert (2011) and Fang (2012)

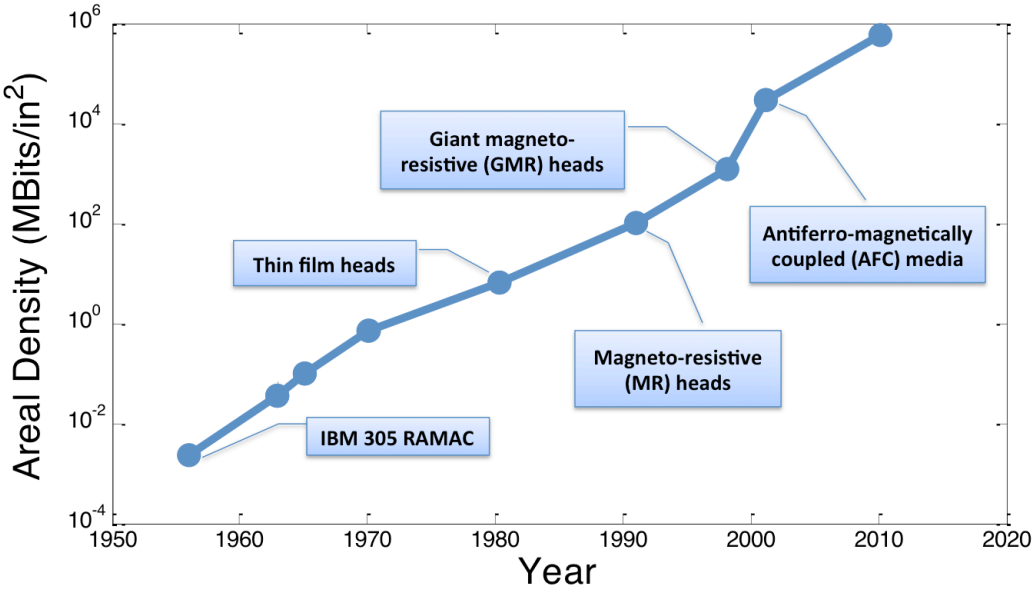

Figure 1.2: Since 1956, areal density in hard disk drives has grown at a rate of approximately 60% per year. Growchoski (1996) and Wood (2009)

1.3 Hard Disk Drive Architecture

Before discussing the technical challenges associated with maintaining the current areal density growth rates in HDDs, it is helpful to first review the basic architecture of an HDD. This architecture has remained surprisingly unchanged over the last 50 years. Fig. 1.3 shows the basic layout of a modern 3.5" desktop HDD with four platters.

Data is stored in positively or negatively magnetized regions on a rigid magnetic substrate call a "disk." This disk can either be made from a glass or a metal substrate. It is coated with several magnetic materials which, for the current perpendicular magnetic recording (PMR) technology, includes a multi-layer stack with a soft magnetic underlayer, anti-ferromagnetic coupling layer, another soft magnetic underlayer, several seed layers, and then the hard ferromagnetic recording medium with a carbon overcoat for protection. Bits of information are written by concentrating a strong magnetic field from write coils through a poling tip which flies directly above the disk surface to permanently magnetize regions of the ferromagnetic recording medium. [7]

To read the data, current HDDs employ spin-valve transducers based on the giant magneto-resistance effect discovered by Fert in 1988 [9]. These transducers convert magnetic fields directly over the recording medium to an electrical readback current. [7] The bitrate of this signal will depend on the spacing between written bits, called the linear bit density, and the angular velocity of the spindle motor, called the spindle speed, which is depicted by the blue arrows in Fig. 1.3.

The read and write elements are fabricated on the trailing edge of a slider as depicted in Fig. 1.4. The position of this slider is controlled both passively and actively. In the fly-height direction, the position is controlled by an air-bearing between the bottom of the slider and the top of the disk surface. Often, a low-bandwidth thermal actuator may also be added to adjust the fly-height in open-loop. In contrast, the track position is controlled in closed-loop by a voice-coil motor (VCM) which converts input current to torque on an actuator arm as depicted in Fig. 1.3. This torque must overcome pivot friction and slider drag as it induces rotational acceleration in the actuator arm, suspension and slider to move the read-write head. [10]

Position feedback is obtained by demodulating periodic servo bursts distributed circumferentially around the disk in regions called servo sectors. This position error signal (PES) will therefore have a sample rate that depends on the number of servo sectors and the spindle speed. [10]

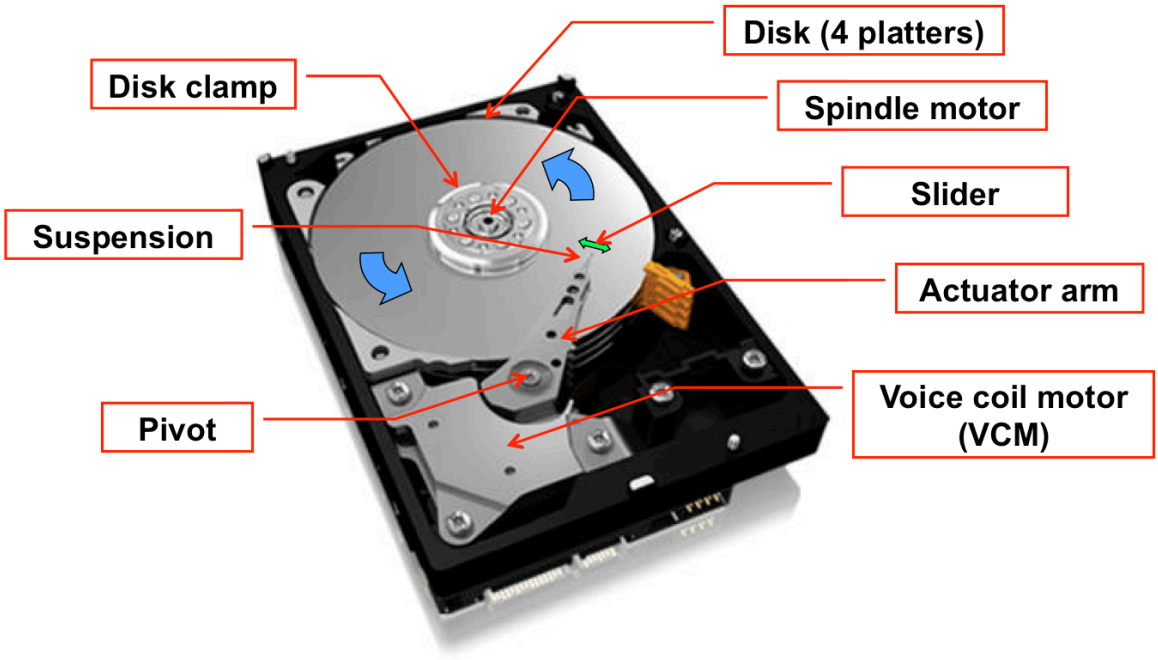

Figure 1.3: Architecture of a modern 3.5" desktop hard disk drive with four platters where blue arrows depict direction of spindle rotation and green arrow depicts direction of slider motion.

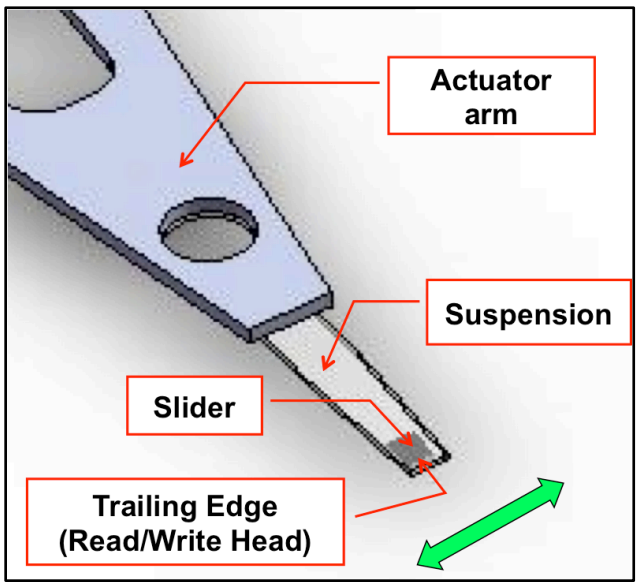

Figure 1.4: Location of trailing edge of a slider in modern hard disk drives with direction of slider motion depicted with the green arrow.

1.4 Servo Control Challenges for Next-Generation HDDs

For the next generation of HDDs to meet areal density targets in keeping with Kryder's Law, many significant mechanical engineering challenges arise. These can be put into two main categories: recording media and servo control. Significant progress is being made in improving recording media with heat-assisted magnetic recording (HAMR) and bit-patterned magnetic recording (BMPR) but these issues will not be addressed here. With respect to the servo control, effort is being made in improving servo hardware and control software. This dissertation will focus mainly on the improvements to servo hardware necessary for decreasing track widths.

1.4.1 Decreasing Track Widths

One of the most challenging consequences of increased areal density is that it requires more and more narrow track widths. Table 1.1 shows a brief list of representative HDDs from each decade. As seen in Fig. 1.5, HDD track widths have been decreasing at a rate of approximately 15% annually for concentric recording, in which bits are written in concentric segments across the radius of each disk. In order to follow Kryder's Law, this trend must continue at a rate of approximately 11% annually for current zoned or shingled recording techniques, in which bit area is now approximately the same across the disk. This can be shown by considering the total theoretical capacity of an HDD which is given by the ratio of disk area to bit area,

$$Capacity = \frac{\pi(D_O^2 - D_i^2)}{4(TW/LBD)} \tag{1.1}$$

where D_o is the outer track diameter, D_i is the inner track diameter, TW is the track width, and LBD is the linear bit density. For a given bit aspect ratio, BAR, the linear bit density will be,

$$LBD = \frac{BAR}{TW} \tag{1.2}$$

therefore Eq. (1.1) can be rewritten in terms of bit aspect ratio and track width,

$$Capacity = \frac{\pi(D_O^2 - D_i^2)}{4(TW^2/BAR)} \tag{1.3}$$

and the total theoretical capacity will only be a function of the track width and the bit aspect ratio. Note that the bit aspect ratio cannot deviate from unity by more than an order of magnitude without becoming magnetically unstable. If a constant bit aspect ratio is thus assumed, the capacity of a given diameter of HDD will scale proportionally to the inverse square of track width. This means that a 60% compound annual growth in capacity will necessitate an 11% compound annual decline in track width.

Table 1.1: Track width data collected from the leading hard disk drive models of each decade from 1956 to the present.

Year	HDD Model	Tracks Per Inch	Track Width (Inch)	Reference
1956	RAMAC 305 (IBM)	2.00E+01	5.00E-02	[11]
1965	2314 (IBM)	4.00E+01	2.50E-02	[12]
1973	Winchester 3340 (IBM)	1.74E+02	5.76E-03	[13]
1980	ST-504 (Seagate)	2.56E+02	3.91E-03	[14]
1989	3390 (IBM)	2.23E+03	4.49E-04	[15]
1998	Caviar 2.1 (WD)	3.00E+04	3.33E-05	[11]
2009	Barracuda (Seagate)	1.50E+05	6.67E-06	[16]

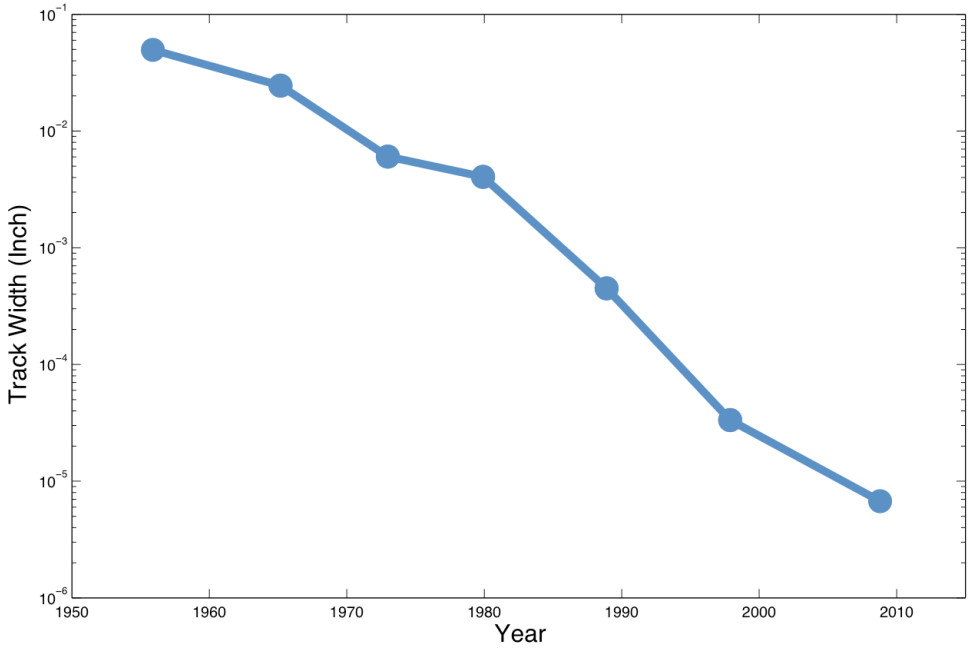

Figure 1.5: Since 1956, HDD track widths have been decreasing at a rate of approximately 15% compound annual decline.

As track widths are decreased, the allowable position error must decrease proportionally to remain within track misregistration (TMR) tolerances. Generally, TMR tolerances require the three-sigma position error signal to be within 10% of the total track width [10]. Given the annual decline in track width from Fig. 1.5, this means the standard deviation of position error will also need to be reduced at a rate of approximately 11% annually. Given that current track widths are as low as approximately 4.7 micro-inches (120 nm), then the extension of Kryder's Law to the next decade of HDDs will entail track widths of 1.9 micro-inches (47 nm). To maintain TMR tolerances, the three-sigma position error signal must be reduced to 190 nano-inches (4.7 nm). Table 1.2 presents a brief summary of this PES roadmap for shingled recording.

Table 1.2: PES Roadmap for shingled recording based on Kryder's Law

Year	Tracks Per Inch *(TPI)*	Track Width *(Inches)*	Three-sigma PES *(Inches)*	Three-sigma PES *(nm)*
2010	2.1E+05	4.7E-06	4.7E-07	11.94
2015	3.0E+05	3.3E-06	3.3E-07	8.42
2020	5.4E+05	1.9E-06	1.9E-07	4.70
2025	9.7E+05	1.0E-06	1.0E-07	2.63
2030	1.7E+06	5.8E-07	5.8E-08	1.47

1.4.2 Data Access Time and Data Transfer Rate

Two more key figure of merit which must be taken into consideration are data access time and data transfer rate. Simply put, data access time refers to the sum of the seek and settle times. This is complicated by the fact that the HDD must wait until the head reaches the beginning of the desired track which is, on average, one half revolution away. This wait time is called latency. For a spindle speed of 10,000 RPM, the average latency will be approximately 3 milliseconds, which is generally larger than the sum of seek and settle time. The data transfer rate is the rate at which bits can be read from the HDD and it corresponds directly to the rate at which bits pass under the read head. [10]

Data access time and data transfer rate can both be improved by increasing the spindle speed. For data access time, an increased spindle speed will result in an inversely proportional reduction in latency because it directly increases the speed at which the beginning of the next data track arrives. Data transfer rate will be increased directly proportionally to the increase in spindle speed because, for a given track position, it depends only on the linear bit density at the corresponding disk radius and the spindle speed of the HDD. For this reason, the trend has been to increase the spindle speeds with recent high-performance HDDs achieving 10,000 and even 15,000 RPM.

1.4.3 Airflow-Excited Vibration

While there are tremendous performance benefits associated with increasing spindle speeds, there are also significant challenges associated with the associated servo control. It has been observed that as spindle speed increases, high-frequency off-track disturbances, called windage, become larger and larger components of the position error signal. Windage is generated by turbulent airflow in the air-bearing surface and is therefore determined by the Reynolds number [17] which is, in turn, a function of the airflow velocity and thus a function of the velocity of the disk. Simulations in computational fluid dynamics (CFD) have shown that off-track windage force in the 10 kHz frequency range increases 10 dB when spindle speed is increased from 7,200 to 10,000 RPM [17]. Since many of the mechanical modes from the VCM actuator to the slider-head are in the 5 to 15 kHz range, these modes will be excited by windage and PES will be increased for higher spindle speeds.

One of the proposed solutions to airflow-excited vibration has been to change the Reynolds number of the flow by filling HDDs with helium rather than standard air. It has been shown that helium-filled drives can reduce the entire windage disturbance spectrum by approximately 5 dB and suspension resonances can even be reduced by 10 dB or more. [18] However, long-term containment of helium has proven to be quite difficult and therefore industry does not presently utilize it as a viable solution.

A more promising solution for reducing airflow-excited vibration is to increase the servo gains in these higher frequencies of interest for disturbance attenuation or rejection. Although this cannot be done on the VCM, which is massive and consumes high levels of power, a second-stage actuator can be incorporated to boost servo gains in the regions of interest. This dual stage approach has already been successful and put into production since 2009, when Western Digital first introduced the Caviar Black 2TB.

1.5 A Novel Head-Based Actuator

This thesis presents work conducted with the objective of increasing servo bandwidth over current dual-stage actuation schemes. In chapter 2, three categories of dual-stage actuation schemes are presented and the state of the art is assessed for each. A new servo-mechanical technique for modeling and predicting optimal performance with multi-stage designs is presented and employed to determine the benefit provided by each dual-stage scheme from which a case will be made for head-based actuation. In chapter 3, the industry-specified requirements for head-based actuation are given, wherefrom several actuation mechanisms are evaluated, including electrostatic and piezoelectric mechanisms. A new quasi-shear mode piezoelectric actuation scheme is proposed with an analytical beam equation solution and a two-dimensional finite element model to predict the actuator stroke and bandwidth. Chapter 4 describes the prototype quasi-shear mode actuator which

was fabricated in the Berkeley Nanofabrication Laboratory and gives the details of the accompanying process development research. Frequency response testing for the final prototype is also presented. Chapter 5 summarizes the findings of this thesis and draws several conclusions about the future of the piezoelectric quasi-shear mode actuator and similar head-based actuator technologies.

Prior to this work, head-based actuation has appeared to be infeasible due to the complex challenges surrounding integration with the slider head. The quasi-shear mode piezoelectric actuator presented herein resolves two of the most prominent issues pertaining to head-based actuation, namely, trace stiffness and air-bearing pressure loss due to the necessary trailing edge gap. First, it resolves the key issue of trace stiffness by overcoming force limitations in previous electrostatic designs. Using a piezoelectric force in place of the weaker electrostatic forces, traces bonded to the head can now be moved with sufficient force. To ensure that this device can still be manufactured in production, a shear-like motion is achieved while driving the piezoelectric in the longitudinal mode, thereby avoiding the large-scale manufacturing complications involved in shear-directed poling in the plane of a large wafer substrate. For the second key issue, this novel actuator minimizes the air-bearing pressure loss from the trailing edge gap by allowing gap width to be controlled independently of track-following control. This allows the gap to be kept to a fraction of the boundary layer width without reducing the actuator stroke. The remaining work consists of the development of a multi-stack sol-gel process flow for increasing the device stroke and the development of a full manufacturing fabrication process flow for testing on an actual HDD head.

Chapter 2

Comparing Multi-Stage Actuation Schemes

This chapter summarizes the previous work conducted in each of the three dual-stage actuation schemes and gives the normalized stroke of each device. These values are then used to predict the optimal performance of an experimental HDD with various state-of-the-art actuators using a newly developed modeling method. This servo-mechanical model is a synthesis of beam elements utilizing the Galerkin method of weighted residuals and optimal control design with the linear quadratic Gaussian methodology. Based upon this analysis, head-based actuation is shown to be necessary for meeting the performance benchmarks given in chapter 1.

2.1 Previous Work in Dual-Stage Actuation

Current HDDs employ a swinging arm actuator in which a voice coil motor generates a torque on the actuator arm, as depicted in Fig. 2.1. Swinging arm type actuators have been used as the primary means of cross-track actuation since they were first invented by Heath in 1976. [19] These actuators have demonstrated servo bandwidths between 500 and 1,000 Hz, which was sufficient to eliminate unwanted vibrations for track densities below 15 kTPI; however, as track densities and spindle speeds both increased dramatically, it soon became apparent that a second actuator would be necessary to boost servo bandwidth and reject airflow-induced vibration. This need for dual-stage actuation was first recognized by Yen et al [20] as well by Zappe [21] and Fujita [22] and a prototype dual-stage actuator was built shortly thereafter by Mori [23].

Dual-stage actuators for HDDs can be placed into three categories:

1. Actuated suspension
2. Actuated slider
3. Actuated head

Fig. 2.2 illustrates the difference between these three actuation schemes. Note that the placement of the microactuator is different for each of these schemes. In the case of actuated suspensions, the entire suspension along with the head-gimbal assembly is actuated. For actuated sliders, an actuator is placed between the gimbal and the slider so that only the slider is actuated. The actuated mass is even further reduced with actuated heads in which the actuator is placed at the trailing edge of the slider body and only a small shuttle containing the read-write head is actuated.

The two most important figures of merit for a dual-stage actuator are device bandwidth and normalized stroke. For this analysis, bandwidth is defined as the first frequency at which the gain rolls off -3 dB from the steady-state gain. Normalized stroke refers to the nominal displacement across the actuator bandwidth normalized by the actuation voltage for that particular device. Table 2.1 summarizes the previous work in dual-stage actuation and lists both of these figures of merit as reported in literature.

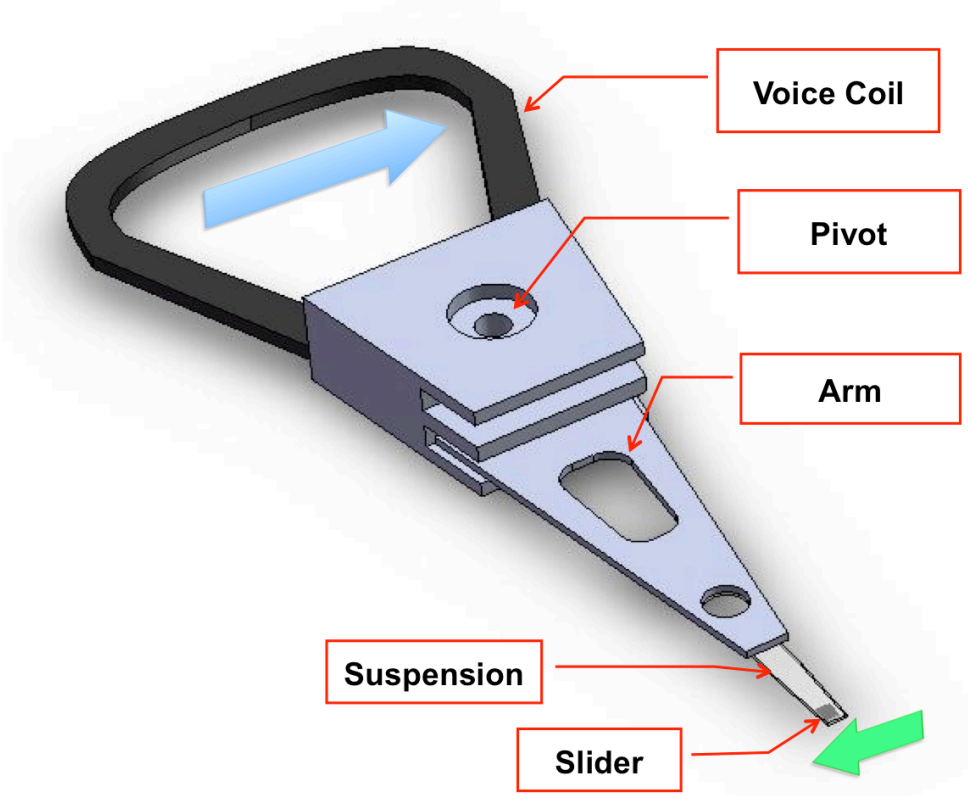

Figure 2.1: The swinging arm actuator uses a voice coil motor to generate torque (top left arrow) on the actuator arm which is then converted to motion in the slider (bottom right arrow)

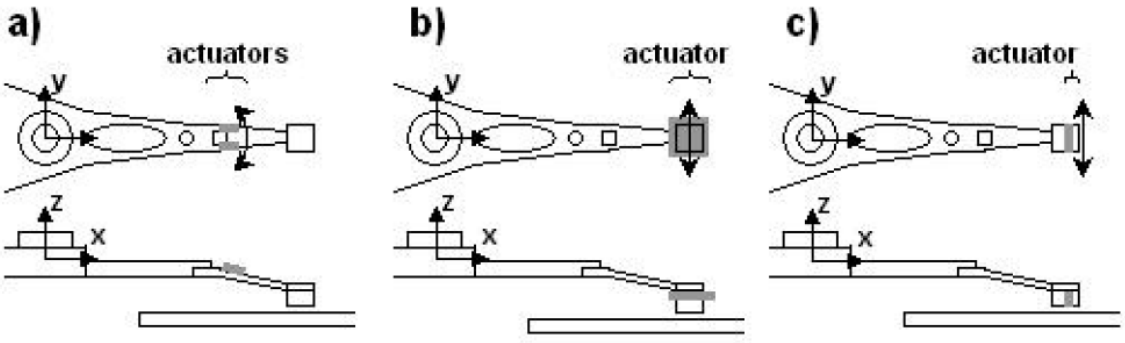

Figure 2.2: There are three categories of dual-stage actuation: (a) actuated suspension (b) actuated slider (c) actuated head. Schematic representation courtesy of Kenn Oldham

Table 2.1: Previous work in dual-stage actuation for HDD applications categorized by actuator location, mechanism and mode with bandwidth and normalized stroke as reported in the literature.

Actuator Location	Mechanism	Mode	Bandwidth	Normalized Stroke	Reference
Suspension	Piezoelectric	Lateral (d31)	1 kHz	96 nm/V	[24]
			7 kHz	28 nm/V	[25]
			10 kHz	300 nm/V	[26]
			10 kHz	280 nm/V	[27]
			20 kHz	50 nm/V	[28]
			20 kHz	200 nm/V	[29]
		Shear (d15)	2 kHz	14 nm/V	[30]
Slider	Piezoelectric	Lateral (d31)	7 kHz	15 nm/V	[31]
		Shear (d15)	No data	No data	[32]
	Electromagnetic	Rotational	1 kHz	No data	[33]
	Electrostatic	Translational	1.6 kHz	267 nm/V	[34]
			2.5 kHz	100 nm/V	[35]
			3.5 kHz	24 µm/V	[36]
			6 kHz	67 nm/V	[37]
		Rotational	1.6 kHz	35 nm/V	[38]
			10 kHz	No data	[37]
Head	Electrostatic	Translational	25 kHz	47 nm/V	[39]
			40 kHz	11 nm/V	[40]
	Piezoelectric	Shear (d15)	500 kHz	No data	[41]

2.2 Predicting Multi-Stage Performance Limitations

Currently, only suspension-based actuators are employed by industry. In general, suspension-based actuators exhibit the largest normalized stroke because they take benefit from the mechanical advantage provided by the length of the suspension. Although they must actuate a significantly larger mass than slider or head-based actuators do, there is more space available for the actuator and therefore more massive devices can be used to meet the force requirements. Their bandwidths, however, remain limited by the compliance of these same suspensions that provide a leverage arm for large normalized strokes. The primary system mode of these suspensions tends to be around 10 kHz, after which suspension-based microactuators exhibit a 20 dB/decade roll-off. This means that a microactuator with a normalized stroke of 300 nm/V as reported by Kobayashi will only produce a gain of 100 nm/V at 30 kHz. As spindle speeds continue to increase, airflow-induced vibration in frequencies beyond the bandwidth will become a more and more significant component of PES to the point where suspension-based actuation will no longer provide adequate attenuation. The rest of this chapter will be devoted to determining performance limitations for each actuation scheme. The purpose of this is to determine what spindle speed and areal density will require industry to switch to a new actuation scheme.

2.3 Transfer Function Derivation from Flexural Elements

A great deal of work has been done to model the frequency response of complex mechanical structures in vibration. [42] This technique, however, is not very compatible with control synthesis techniques, which require a well-defined plant transfer function rather than merely a plot of frequency response. For cases where performance must be optimized with regard to both the mechanical structure and the controller, this makes for a very lengthy cycle of iterations. Generally, this process is done manually, where one mechanical engineer determines the frequency response of a new design based on finite element analysis and then relays this to a control engineer who identifies an appropriate transfer function for the plant and synthesizes a controller based on it. The optimal performance of this structure is then compared with previous structures and the process is iterated until a suitable mechanical design is found.

Not only is this approach difficult to automate, it also lacks the transparency necessary for engineers to gain an intuitive understanding of the influence each component has on the overall plant response. Oldham shows a method for automating sensor design and placement by iterating between a very simple sensitivity analysis and predefined sensor geometries [43]. This method and similar approaches shows how such a problem may be automated; however, giving engineers the necessary transparency to make design choices requires a greater level of abstraction. In the following sections, a method will be proposed for

simplifying a mechanical structure, such as what is found in modern HDDs, into a series of beam elements with an equivalent uniform moment of inertia and beam length relative to a standard rectangular cross-sectional area. These beam elements will be used to formulate a global equation of motion and a method for finding the Laplace-domain solution will be proposed. In finite element models, the number of modes will correspond to the number of degrees of freedom, which is the number of nodes times the degrees of freedom for each node. By abstracting the mechanical structure into a series of beams, the number of resonant modes is reduced to a much more manageable set and a closed-form solution for the transfer function of this model can be easily found, as will be demonstrated below.

2.3.1 Equation of Motion for Beam Elements Based on Galerkin's Method

The equation of motion for a single beam in free oscillation with no damping is [44]:

$$\frac{\partial^2}{\partial x^2}\left(EI\frac{\partial^2 v}{\partial x^2}\right)+\rho A\ddot{v}=0 \tag{2.1}$$

where v is the lateral displacement of the beam as a function of x, the position along it's length, E is the Young's modulus, I is the cross-sectional moment of inertia, ρ the equivalent density and A is the equivalent area of the beam's cross-section. For cases where there are multiple components in this system and I and A will be changing with x, this becomes difficult to solve analytically. We will instead employ Galerkin's method of weighted residuals to approximate the shape of the beam with a series of elements defined as follows:

$$\begin{aligned} v(x)=v_1\left(1-\frac{3}{L^2}x^2+\frac{2}{L^3}x^3\right)+\theta_1\left(x-\frac{2}{L}x^2+\frac{1}{L^2}x^3\right)\\ +v_2\left(\frac{3}{L^2}x^2-\frac{2}{L^3}x^3\right)+\theta_2\left(-\frac{1}{L}x^2+\frac{1}{L^2}x^3\right) \end{aligned} \tag{2.2}$$

where v_1 and θ_1 are the lateral and angular displacement of the left node, respectively, and v_2 and θ_2 are the lateral and angular displacement of the right node, as shown in Fig. 2.3.

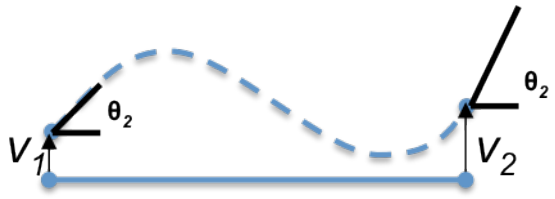

Figure 2.3 Motion at the nodes of each beam element from the original element (solid line) to the displaced element (dashed line)

It can be shown that, after integration along the length of the beam with these Galerkin profiles as done by Hutton [45], Eq. (2.1) will become:

$$\left[m^{(e)}\right]\{\ddot{q}\} + \left[k^{(e)}\right]\{q\} = \{Q\} \tag{2.3}$$

$$\{q\} \stackrel{\text{def}}{=} \begin{Bmatrix} v_1 \\ \theta_1 \\ v_2 \\ \theta_2 \end{Bmatrix} \tag{2.4}$$

where $m^{(e)}$ is the elemental mass matrix, $k^{(e)}$ is the elemental stiffness matrix, and Q contains the forces and moments acting externally to the corresponding left and right nodes, as defined below:

$$\left[m^{(e)}\right] = \frac{\rho AL}{420}\begin{bmatrix} 156 & 22L & 54 & -13L \\ 22L & 4L^2 & 13L & -3L^2 \\ 54 & 13L & 156 & -22L \\ -13L & -3L^2 & -22L & 4L^2 \end{bmatrix} \tag{2.5}$$

$$\left[k^{(e)}\right] = \frac{EI_z}{L^3}\begin{bmatrix} 12 & 6L & -12 & 6L \\ 6L & 4L^2 & -6L & 2L^2 \\ -12 & -6L & 12 & -6L \\ 6L & 2L^2 & -6L & 4L^2 \end{bmatrix} \tag{2.6}$$

$$\{Q\} = \begin{Bmatrix} -V_1(t) \\ -M_1(t) \\ V_2(t) \\ M_2(t) \end{Bmatrix} \tag{2.7}$$

and L is the length of the beam element. In order to incorporate damping, Eq. (2.3) is modified as follows:

$$\left[m^{(e)}\right]\{\ddot{q}\} + \left[c^{(e)}\right]\{\dot{q}\} + \left[k^{(e)}\right]\{q\} = \{Q\} \tag{2.8}$$

and the damping matrix $c^{(e)}$ is generally either estimated using the Rayleigh method [47] or identified experimentally as shown by Pilkey [46]. For the purposes of illustration here, a proportional damping matrix will be used according to the Rayleigh proportional damping method [47]:

$$\left[c^{(e)}\right] = \alpha\left[k^{(e)}\right] + \beta\left[m^{(e)}\right] \tag{2.9}$$

where α and β are the Rayleigh constants.

2.3.2 Derivation of an HDD Transfer Function

To consider various dual-stage actuation schemes, the following model is considered as illustrated in Fig. 2.4:

1. Four simplified beam elements representing (a) voice coil structure (b) actuator arm (c) suspension/gimbal and (d) slider.
2. These elements are connected end-to-end as shown with
3. Node (2) represents the pivot spring force, F_2, and pivot friction defined to be M_2
4. Node (1) is acted upon by an external force and moment , F_1 and M_1 which represent the VCM input
5. Node (3) contains the internal moment generated by the suspension-based actuator, M_3
6. Node (4) contains the internal translational force, F_4, and rotational moment, M_4, generated by the slider-level actuator
7. Node (5) is acted upon by an external drag force, F_5, and moment, M_5, which represents the windage forces combined with the much smaller force of intertia of the read-write head being actuated. Note here that the bandwidth of the read-write head is assumed to be arbitrarily wide.

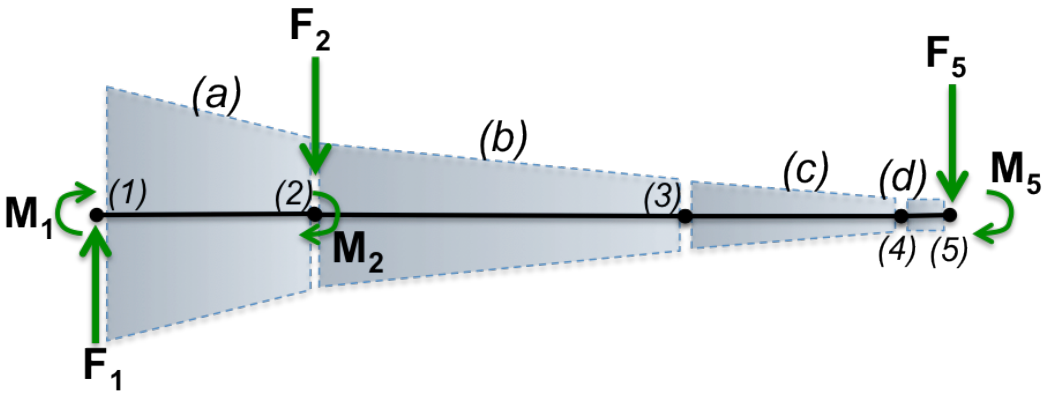

Figure 2.4: Beam element model of dual-stage actuation mechanics includes (a) voice coil structure (b) actuator arm (c) suspension/gimbal and (d) slider with head-based actuator at node (5) and pivot at node (2)

For this model, the global displacement vector can be defined as follows:

$$\{q_G\} \stackrel{\text{def}}{=} \{v_1\ \theta_1\ v_2\ \theta_2\ v_3\ \theta_3\ v_4\ \theta_4\ v_5\ \theta_5\}^T \tag{2.10}$$

where v_i and θ_i are the lateral and angular displacements of the i^{th} node. The mass, damping and stiffness matrices can then be expanded to global matrices to obtain the following global equations of motion for the j^{th} element:

$$\left[m_G^j\right]\{\ddot{q}_G\} + \left[c_G^j\right]\{\dot{q}_G\} + \left[k_G^j\right]\{q_G\} = \{Q_G^j\} \tag{2.11}$$

If these equations of motion are added together, the global equation of motion is found:

$$[m_G]\{\ddot{q}_G\} + [c_G]\{\dot{q}_G\} + [k_G]\{q_G\} = \{Q_G\} \tag{2.12}$$

where the forcing vector is:

$$\{Q_G\} = \{F_1\ M_1\ F_2\ M_2\ F_3\ M_3\ F_4\ M_4\ F_5\ M_5\}^T \tag{2.13}$$

Generally, the solution is found when considering only one force input, F_i or M_i, with a given frequency, ω, and unit amplitude; although this yields a frequency response plot of the model, it is more useful to derive a transfer function for subsequent control synthesis. This can be done by taking the Laplace transform of Eq. (2.11) as follows:

$$s^2[m_G]\{q_G(s)\} + s[c_G]\{q_G(s)\} + [k_G]\{q_G(s)\} = \{Q_G(s)\} \tag{2.14}$$

and the left-hand side of this equation can be simplified into an equivalent symbolic matrix, $[P_G(s)]$,

$$[P_G(s)]\{q_G(s)\} = \{Q_G(s)\} \tag{2.15}$$

The solution requires a symbolic matrix inversion:

$$\{q_G(s)\} = [P_G(s)]^{-1}\{Q_G(s)\} \tag{2.16}$$

where the resulting vector will contain the normalized transfer function from the force input, F_i or M_i, to the i^{th} node. Two methods can be used for inverting $[P_G(s)]$. The first method utilizes the symbolic matrix inverse command in MATLAB which follows the generalized matrix inversion rules. This method is very slow and inaccurate for models with more than 4 nodes; a more robust method was developed in which the concatenated matrix, $[P_G(s)\ q_G(s)]$, is transformed to reduced row echelon form using the symbolic MATLAB command, *rref*. Using row reduction, the solution was found to be nearly identical to the standard frequency response solution, as shown in Fig. 2.5.

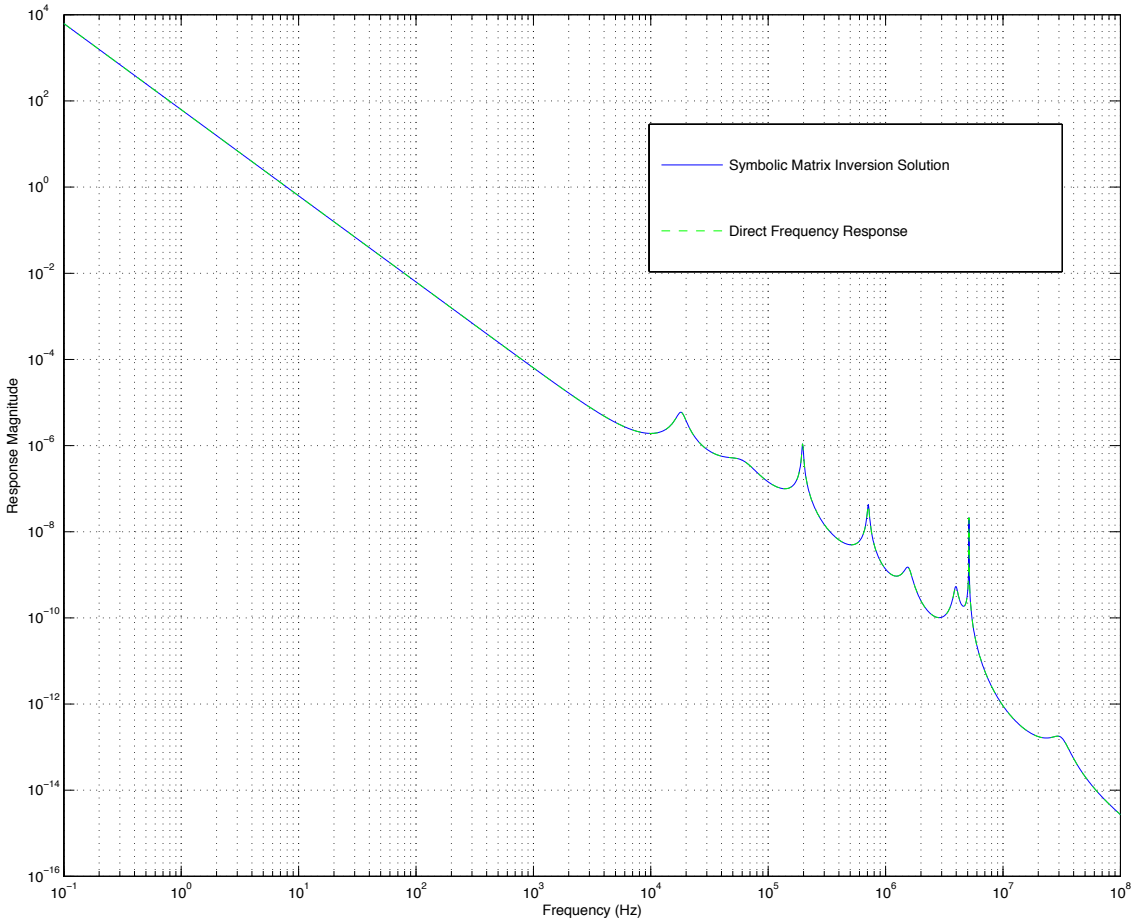

Figure 2.5: The frequency response generated from the symbolic matrix inversion approach is nearly identical to the frequency response computed using the direct approach

2.3.3 Physical Model Verification

Next, this model was verified with respect to an actual analytical solution of a cantilever beam. As shown in Fig. 2.6, this model consists of a massless undamped cantilever beam with end-mass. With these assumptions, the exact solution for the fundamental frequency of the cantilever beam can be found based on the natural frequency for a mass-spring system [48]:

$$\omega_n \stackrel{\text{def}}{=} 2\pi f_n = \sqrt{\frac{k}{m}}\ rad/s \tag{2.17}$$

where the stiffness of the spring, k, is given by the equation for stiffness of a beam under static loading [49]:

$$k \stackrel{\text{def}}{=} \frac{P}{\delta} = \frac{3EI}{L^3} \tag{2.18}$$

and where the end mass, m, is modeled as a beam with a rectangular cross-section of height, h, and width, w, as well as density, ρ, and a length L which is much less than the height and width. The parameters used for this model verification are shown in table 2.2:

Table 2.2: Parameters used for model verification

Parameter	Symbol	Units	Element 1	Element 2
Young's Modulus	E	Gpa	200	1000
Density	ρ	kg/m^3	0	7850
Rayleigh Alpha	α	-	0	0
Rayleigh Beta	β	-	0	0
Length	L	mm	3	0.1
Height	h	mm	3	10
Width	w	mm	1	10
Relative Moment of Inertia	I_{rel}	-	1	1

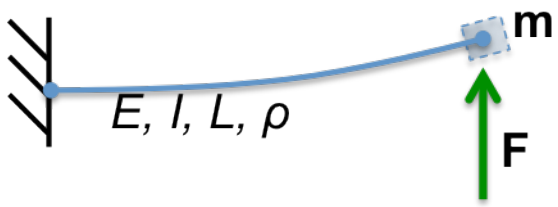

Figure 2.6: Schematic of cantilever beam used for verifying the accuracy of the beam model

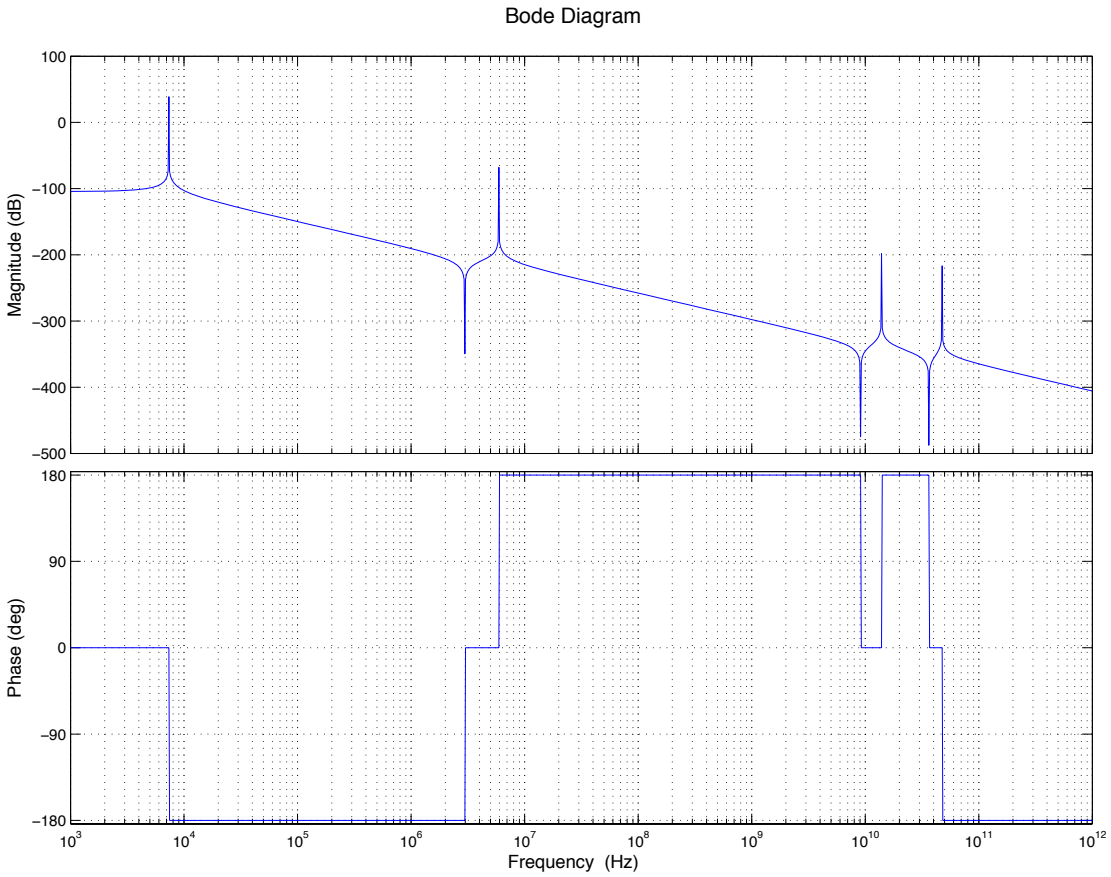

Figure 2.7: Verification of the physical model using a cantilever beam reveals a primary system mode at 46,191.2 rad/s which is very close to the theoretical value of 46,364.7 rad/s (7.38 kHz) based on Eqs. (2.17) and (2.18)

The transfer function for this test system was derived by applying the symbolic matrix inversion method described above. Based on the imaginary component of the lowest complex pole of this transfer function, the fundamental frequency was estimated to be 46,191.2 *rad/s*, compared with the theoretical value of 46,364.7 *rad/s* (7.38 *kHz*) based on Eqs. (2.17) and (2.18). Note that this corresponds to the first peak observed in Fig. 2.7, which is a Bode plot of the derived transfer function from force at the end mass, F to displacement at the end mass, v_3. Also, note that the steady-state response of *-104 dB* corresponds directly to the static deflection, $\delta_{dB} = 20\log_{10}(F/k)$ where F is normalized to 1 N/m and k was calculated to be 1.6875e+05 N/m. Furthermore, the magnitude of this plot rolls off at -40 *dB/decade* as expected for a mass-spring system above the natural frequency. The next antiresonance and resonance pair is the result of higher order modes. After this, the remaining antiresonance and resonance pairs are the result of the compliance of the end mass. In total, there are 8 complex roots and 6 complex zeros in this test system. The roots correspond to the 12 state variables in the expanded $\{q^E(s)\}$ vector minus the 2 translational and 2 rotational terms at node 1 which are fixed at zero.

2.4 Multi-Stage Performance and HDD Design

Two HDD models will be considered, an experimentally characterized HDD and a modified HDD structure, in order to illustrate how performance is affected by structural stiffness and damping in respective modes. The structure parameters are given in table 2.3. Furthermore, the effect of increasing spindle speed will be demonstrated with an analysis of 10, 15 and 20 kRPM drives with windage models derived from the relationship between shear torque of turbulent air-flow and spindle speed [18]. Lastly, the relationship between optimal performance and the number of servo sectors is also analyzed to demonstrate necessary improvements in position sampling rate.

Table 2.3 Structure parameters and associated constants

	Parameter	Symbol	Units	Experimental HDD Structure
Element 0 (Pivot)	Spring Constant	k_p	N/m	1.00E+13
	Damping Constant	c_p	N s/m	1.00E+01
	Pivot Stiction Constant	k_{pf}	N/rad	6.00E-01
	Pivot Viscous Damping	c_{pf}	N s	2.00E-04
	Torsion Spring Constant	k_{tors}	N m/rad	7.00E+09
	Torsion Damping Constant	c_{tors}		1.00E-02
Element 1 (Coil)	Equivalent beam length	L	m	2.00E-02
	Equivalent beam height	h	m	5.00E-03
	Equivalent beam width	w	m	1.00E-02
	Density	ρ	kg/m^3	7.85E+03
	Modulus of elasticity	E	Pa	2.00E+11
	Poisson ratio	v	-	2.90E-01
	Relative moment of inertia	I_r	-	3.00E+03
	Relative polar moment	J_r	-	1.00E+00
	Flexural Rayleigh Alpha	α	-	1.00E-08
	Flexural Rayleigh Beta	β	-	1.00E-08
	Torsional Rayleigh Alpha	α_{tors}	-	5.00E-07
	Torsional Rayleigh Beta	β_{tors}	-	5.00E-07
Element 2 (Arm)	Equivalent beam length	L	m	2.50E-02
	Equivalent beam height	h	m	2.00E-03
	Equivalent beam width	w	m	5.00E-03
	Density	ρ	kg/m^3	7.85E+03
	Modulus of elasticity	E	Pa	2.00E+11
	Poisson ratio	v	Pa	2.90E-01
	Relative moment of inertia	I_r	-	3.00E+01
	Relative polar moment	J_r	-	1.00E+00
	Flexural Rayleigh Alpha	α	-	1.00E-05
	Flexural Rayleigh Beta	β	-	5.00E-05
	Torsional Rayleigh Alpha	α_{tors}	-	1.00E-09
	Torsional Rayleigh Beta	β_{tors}	-	1.00E-09
Element 3 (Suspension)	Equivalent beam length	L	m	1.00E-02
	Equivalent beam height	h	m	1.00E-03
	Equivalent beam width	w	m	2.00E-03
	Density	ρ	kg/m^3	7.85E+03
	Modulus of elasticity	E	Pa	2.00E+11
	Poisson ratio	v	Pa	2.90E-01
	Relative moment of inertia	I_r	-	1.60E-01
	Relative polar moment	J_r	-	1.00E+00
	Flexural Rayleigh Alpha	α	-	1.00E-06
	Flexural Rayleigh Beta	β	-	1.00E-06
	Torsional Rayleigh Alpha	α_{tors}	-	1.00E-08
	Torsional Rayleigh Beta	β_{tors}	-	1.00E-08
Element 4 (HGA/Slider)	Equivalent beam length	L	m	3.00E-03
	Equivalent beam height	h	m	2.00E-04
	Equivalent beam width	w	m	2.50E-04
	Density	ρ	kg/m^3	7.85E+03
	Modulus of elasticity	E	Pa	3.70E+11
	Poisson ratio	v	Pa	2.90E-01
	Relative moment of inertia	I_r	-	1.60E-01
	Relative polar moment	J_r	-	1.00E+00
	Flexural Rayleigh Alpha	α	-	5.00E-06
	Flexural Rayleigh Beta	β	-	5.00E-06
	Torsional Rayleigh Alpha	α_{tors}	-	1.00E-09
	Torsional Rayleigh Beta	β_{tors}	-	1.00E-09

2.4.1 HDD Structure

The structure of an experimental HDD was identified based on the standard 3.5" HDD dimensions from table 2.3 with the force constants based on the highest gains documented in table 2.1. The single-stage structure model, with a frequency response as shown in Fig. 2.8, was obtained by adjusting the relative moment of inertia of each element to match simulated and observed modes in the HDD. Each of the modes that appears in the resulting structure is shown in Fig. 2.9. The commonly observed modes, as numbered on each bode plot, are:

(1) Pivot mode
(2) "Butterfly" mode
(3) Suspension/gimbal torsion modes
(4) Coil mode
(5) Secondary sway mode

The first mode is generally the pivot mode. It contains both viscous damping and bearing elasticity terms that combine to act as an underdamped resonance. For illustrative purposes, modes (2) and (5), the first two flexural modes, are shown in Fig. 2.10. Mode (2), which is commonly referred to as the "butterfly mode," contains a very large oscillation of the pivot, as modeled and identified by Liu [50]. Based on the analysis here, it is observed that the pivot oscillation may also be significantly out of phase with the "flapping" motion of the coil and arm, leading to an asymmetry between forward and backward motion.

According to Timoshenko beam theory, for microstrain deflections where warping due to beam deformation is negligible, the torsion modes are linearly independent from the flexure modes [51]. This means that the transfer functions for bending effects are combined in parallel with the transfer function for torsion. For the HDD structure given here, the torsion mode transfer function is smaller than the flexure mode everywhere except the modes around (3), and the phase drops or rises only locally at this frequency whereas it will always drop 180° at each of the flexure mode since this is the dominant component for the combined transfer function. Also, the combined HDD transfer function includes a model of the power amplifier in series with the structure transfer function. This amplifier is represented as follows:

$$G_{amp}(s) = k\frac{e^{-T_d s}}{T_{amp}s+1} \tag{2.19}$$

where k is the amplifier gain, T_d is the computational time delay, and T_{amp} is the amplifier time constant.

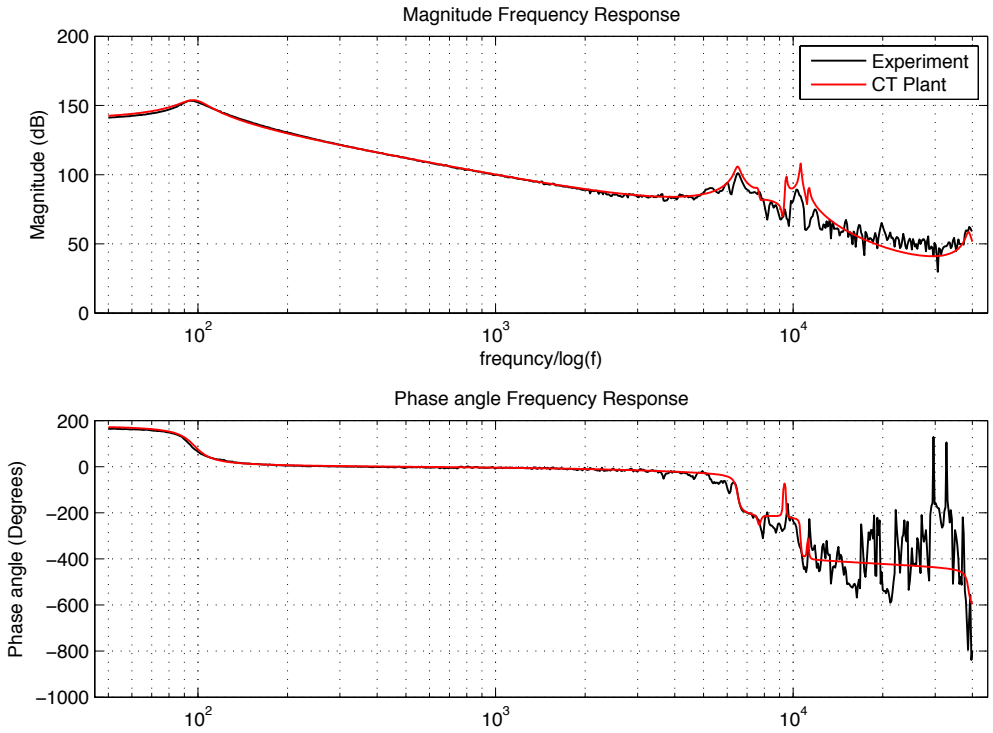

Figure 2.8: The structure of an experimental HDD was derived by adjusting the relative moments of inertia of elements to match simulated and observed modes

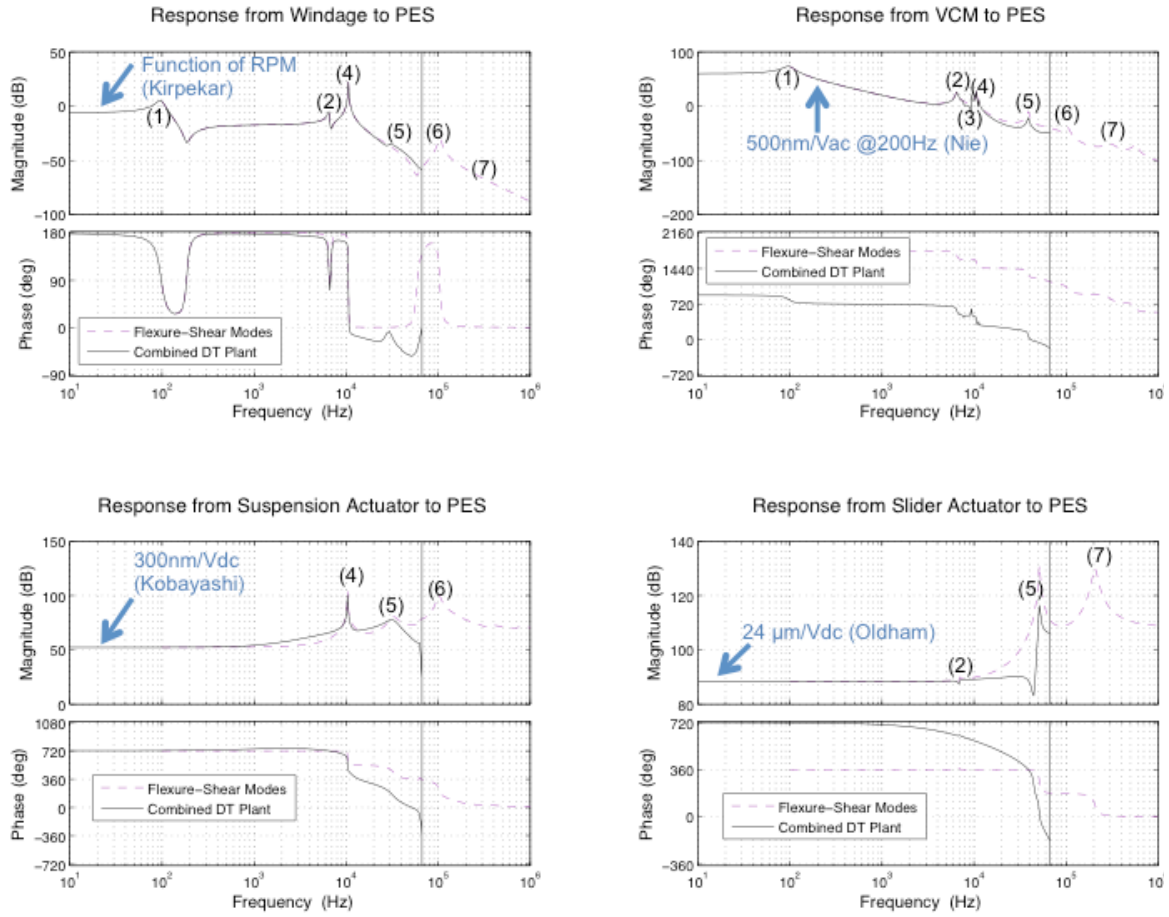

Figure 2.9: Bode plots of the experimental HDD structure with transfer functions of windage, VCM, suspension, and slider actuators to PES. The numbered common modes correspond to: (1) Pivot mode (2) Suspension sway mode (3)Torsion modes (4) Gimbal mode (5) Coil mode and (6) Secondary suspension sway mode. The vertical black lines indicate the Nyquist frequency for a 10,000 RPM drive with 800 sectors. The blue arrows are to describe how the force constant was calibrated for each input.

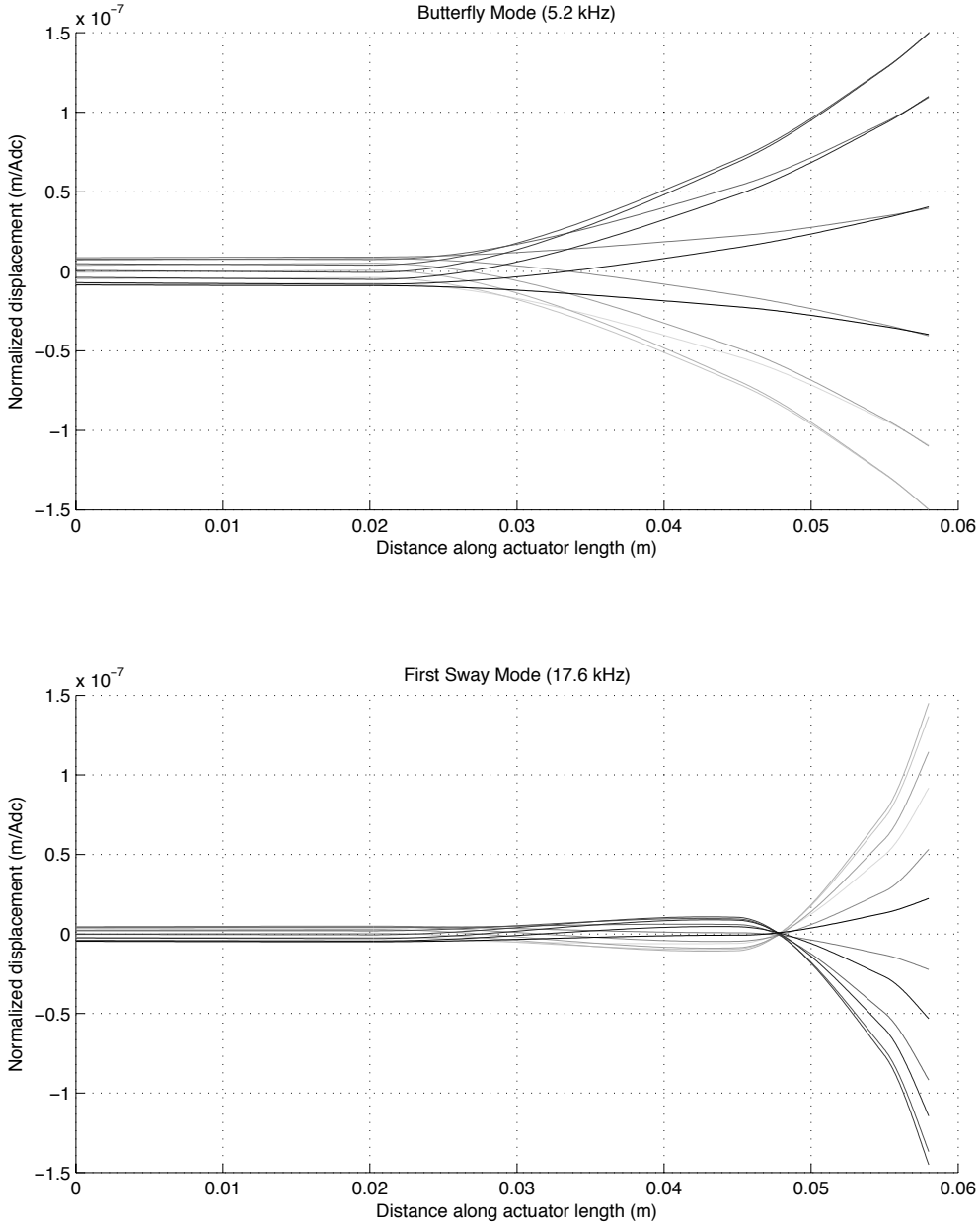

Figure 2.10: The butterfly mode makes a "flapping" motion of the arm and coil structures and contains no resonance nodes. The sway modes contain N resonance nodes and the pivot becomes an antinode.

2.4.2 Optimal Performance Analysis

The optimal performance is analyzed based on the single-input multi-output (SIMO) control structure given in Fig. 2.11. The HDD plant is represented by $\mathbf{G_{hdd}}$ and the optimal controller is represented as $\mathbf{K_{lqg}}$. In this configuration, the position measurement is contaminated by measurement noise, *n*, which is assumed to be less than 1% of the track width being evaluated. For practical track-following power reduction, upper bounds of 2V and 5V were placed on the variance of inputs to the VCM and microactuators, respectively, as is commonly done for track-following control designs [52]. The open-loop disturbance was assumed to be 16 nm, 33 nm, and 56 nm. These values were based on CFD simulations for HDD's at 10,000 RPM [17] and the corresponding increases in turbulent windage-shear torque with increasing spindle speeds to 15,000 and 20,000 RPM, respectively [18].

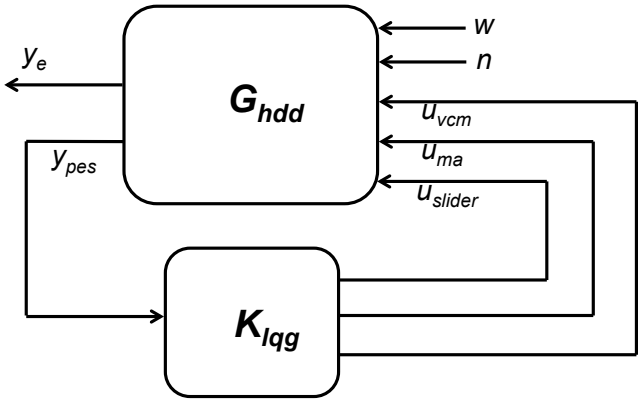

Figure 2.11: Example of the controller structure used to analyze optimal performance of a three-stage actuator

The stationary LQG controller is formulated in discrete time as the control input which minimizes the cost function:

$$J_s = \frac{1}{2} E\{x^T(k)Qx(k) + u^T(k)Ru(k)\} \tag{2.20}$$

given

$$x(k+1) = Ax(k) + Bu(k) + B_w w(k) \tag{2.21}$$

$$y(k) = Cx(k) + Dn(k) \tag{2.22}$$

where A, B, and C are the multi-input single-output (MISO) state-space representation of $\mathbf{G_{HDD}}$. Also, B_w is the airflow disturbance and Q and R are weighting

matrices selected through an iterative procedure to minimize the PES output *y(k)* subject to the input constraints on *u(k)*. This analysis is carried out using the previously developed MATLAB command, *constrlqg* [53].

2.4.3 Comparison of Optimal Performance of each Multi-Stage Scheme

Using the above control structure and the structure parameters given in table 2.3, the optimal performance of the experimental HDD structure is evaluated for five different actuation schemes:

1. Single Stage: only the VCM is actuated
2. Suspension Dual Stage: a PZT suspension-based actuator is incorporated as demonstrated by Kobayashi
3. Suspension/Slider Three Stage: along with a PZT suspension-based actuator, an actuated slider is included as presented by Oldham.
4. Head Dual Stage: a hypothetical second stage actuator is added at the read-write head and is assumed to have a 100 kHz bandwidth with a gain of 20 nm/V
5. Suspension/Head Three Stage: the hypothetical head-based actuator is combined with the PZT suspension-based actuator

From table 2.4, it can be seen that head-based and slider-based actuation schemes achieve comparable performance. In fact, if the gain of the suspension actuator or VCM actuator were large enough without saturating the voltage constraints, these could also achieve this performance. This is the performance limit for the system given the structure parameters and, hence, the result of the windage response during the time between samples. In order to improve performance of these high-bandwidth actuators, the sample time must be decreased. This can be done by either increasing the spindle speed or increasing the number of servo sectors. Both of these solutions are problematic. An increase in spindle speed will lead to an increase in shear torque according to the following relation [18]:

$$M = 0.0311\rho\nu^{1/5}R^{23/5}\omega^{9/5} \tag{2.23}$$

where M is the magnitude of the shear-torque, ρ is the density of air, ν is the kinematic viscosity of air, R is the disk radius, and ω is the spindle speed. This means that windage is roughly proportional to the spindle speed squared.

The servo sample time can also be decreased by increasing the number of servo sectors; however, the HDD industry is very reluctant to do this because it can cause a significant reduction in the total HDD storage capacity. Fortunately, as areal density increases, servo bursts are expected to become smaller and so the number of sectors may still be increased in the future. If this is not adequate, a secondary

position sensor may be incorporated into the HDD control structure with devices like instrumented suspensions in order to improve position sensing [54]. For this simplicity, only the position error signal from servo bursts are considered in this analysis.

Table 2.4 gives the optimal performance of the modeled experimental HDD for each multi-stage actuation scheme for 10, 15, and 20 kRPM spindle speeds with 1500, 3000, and 7500 servo sectors per disk. Fig. 2.12 shows that for the modeled HDD, suspension-based dual stage actuation appears to be adequate for 10 kRPM drives provided that the sample rate remains large enough. For the 15 kRPM drives and up, the increase in windage is large enough that there will be a significant performance benefit in switching to slider or head-based actuation.

Table 2.4 Results of optimal performance analysis of the structure obtained from an experimental HDD for 10, 15, and 20 kRPM spindle speeds and 1500, 3000, and 7500 servo sectors. A suggested time-frame for these HDD's is given in the left column and the (*) indicates that the performance for this particular HDD would not meet the PES roadmap given in chapter 1.

	Three-Sigma Position Error at Optimal Performance (nm)		
	10 kRPM	**15 kRPM**	**20 kRPM**
Year 2010 : Max 3σ PES = 12 nm	**N = 1000 sectors**	**N = 1000 sectors**	**N = 1000 sectors**
Single Stage	23.9*	171*	677*
Suspension Dual Stage	12.1	26.6*	60.2*
Suspension/Slider Three Stage	0.354	0.581	0.773
Head Dual Stage	0.354	0.581	0.773
Suspension/Head Three Stage	0.354	0.581	0.773
Year 2015 : Max 3σ PES = 8.4 nm	**N = 1500 sectors**	**N = 1500 sectors**	**N = 1500 sectors**
Single Stage	13.3*	88.8*	361*
Suspension Dual Stage	5.17	16.8*	39.1*
Suspension/Slider Three Stage	0.184	0.258	0.311
Head Dual Stage	0.184	0.258	0.311
Suspension/Head Three Stage	0.184	0.258	0.311
Year 2025 : Max 3σ PES = 2.6 nm	**N = 3000 sectors**	**N = 3000 sectors**	**N = 3000 sectors**
Single Stage	5.44*	29.3*	118*
Suspension Dual Stage	2.36	8.37*	20.0*
Suspension/Slider Three Stage	0.061	0.073	0.081
Head Dual Stage	0.061	0.073	0.081
Suspension/Head Three Stage	0.061	0.073	0.081
Year 2010 : Max 3σ PES = 1.5 nm	**N = 7500 sectors**	**N = 7500 sectors**	**N = 7500 sectors**
Single Stage	1.962*	7.85*	26.9*
Suspension Dual Stage	0.952	3.45*	8.16*
Suspension/Slider Three Stage	0.018	0.020	0.021
Head Dual Stage	0.018	0.020	0.021
Suspension/Head Three Stage	0.018	0.020	0.021

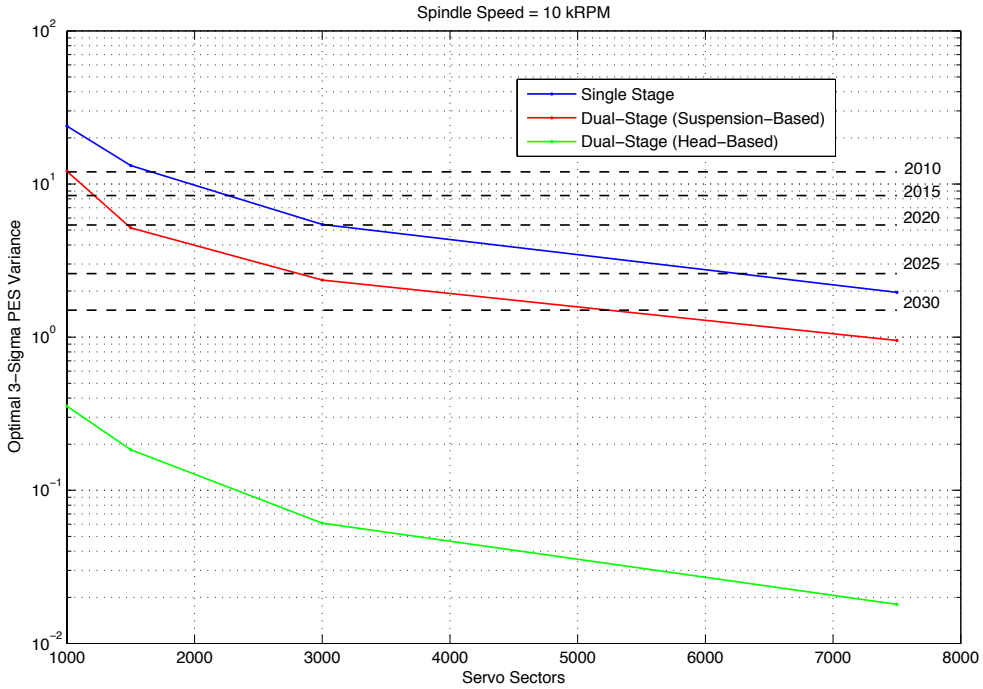
Spindle Speed = 10 kRPM
Single Stage
Dual−Stage (Suspension−Based)
Dual−Stage (Head−Based)
2010
2015
2020
2025
2030
Optimal 3−Sigma PES Variance
Servo Sectors
10^{2}
10^{1}
10^{0}
10^{-1}
10^{-2}
1000
2000
3000
4000
5000
6000
7000
8000

(a)

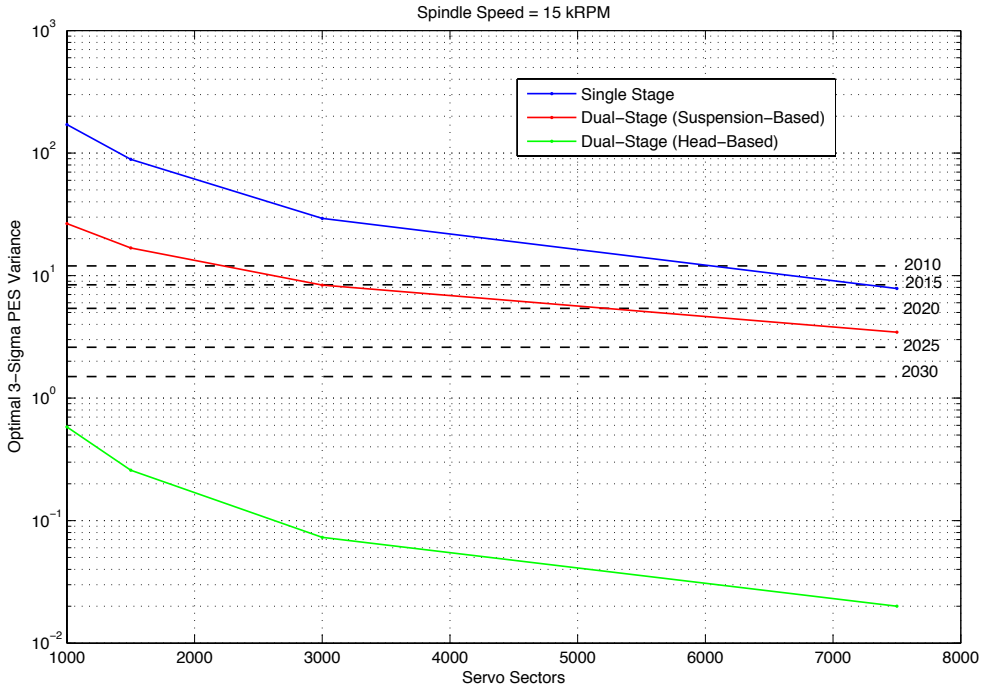
Spindle Speed = 15 kRPM
Single Stage
Dual−Stage (Suspension−Based)
Dual−Stage (Head−Based)
2010
2015
2020
2025
2030
Optimal 3−Sigma PES Variance
Servo Sectors
10^{3}
10^{2}
10^{1}
10^{0}
10^{-1}
10^{-2}
1000
2000
3000
4000
5000
6000
7000
8000

(b)

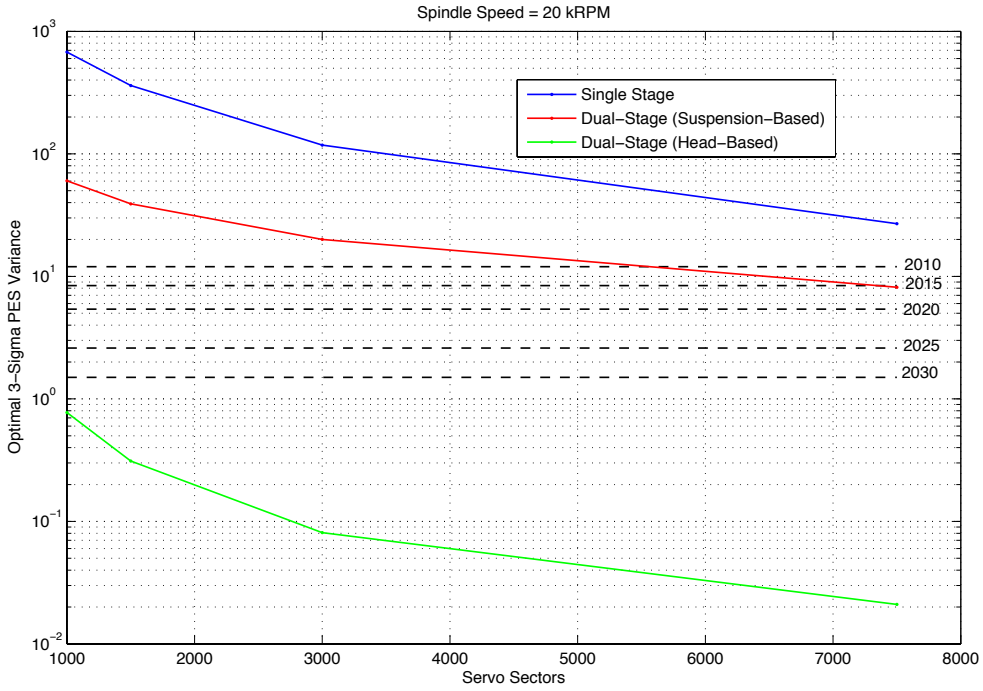

(c)

Figure 2.12: Results of optimal performance analysis of the structure obtained from an experimental HDD demonstrate that dual-stage actuation is necessary for (a) 10 kRPM HDD's and that head-based actuation may be required for (b) 15 kRPM and (c) 20 kRPM HDD's.

2.5 Likely Prospects for Future Microactuation in HDD's

In this chapter, it has been demonstrated that with increasing spindle speeds and areal densities, there will be a point at which suspension-based actuation will no longer be able to attenuate windage disturbances sufficiently. This can be delayed by increasing the number of servo sectors but, at some point, it will inevitably be more economical to switch to a new actuation scheme. This analysis has shown that slider-based and head-based actuation are both viable candidates for this new scheme. It has also shown that three-stage actuation with VCM, PZT actuated suspension, and an actuated head, will probably be unnecessary for at least the next two decades because head-based dual stage actuation proves to be sufficient without the additional actuated suspension.

One word of caution ought to be made with respect to this simplified analysis. It has only sought to demonstrate the optimal performance for a nominal plant whose structural parameters are fixed. For industry application, designing one controller for every plant would be quite infeasible and so a robust control methodology must be employed. Not only so, but the structural parameters will vary with time due to changes such as in temperature and pressure. As a result, the actual controller employed by industry will be much more conservative and the actual performance will be worse. Part of the performance can be recovered using online system identification and mode tracking. Also, the problem will be less pronounced for the head-based actuator because the system modes are significantly higher than the range of interest for windage disturbances.

On the other hand, the overall performance may also be better than what is presented here because the structural parameters may be optimized, depending on which constraints are still necessary and which constraints can be revised. For example, a 1% performance improvement can be gained by decreasing the length of the arm by 5 mm. But this may not be feasible for a specified diameter of disk and therefore the problem of optimizing the HDD structure requires a great deal of engineering intuition. This chapter has only presented the tip of the iceberg when it comes to parametric optimization of the HDD structure with hopes that it will one day become a useful design technique for industry.

Chapter 3

Head-Based Microactuator Design

In chapter 2, a case has been made for the eventual transition from suspension-based actuation to either slider-based or head-based actuation. The driving motivation behind this transition is to increase track-following performance to maintain ever-decreasing position error tolerances with ever-increasing windage disturbances. Another major benefit arises for head-based actuation with regard to integration cost and it is therefore the preferred option. Chapter 3 outlines the constraints given by industry which a head-based actuator must satisfy and evaluates the existing actuation mechanisms with respect to the given constraints. This chapter also proposes a novel head-based actuator to satisfy these constraints and presents analytical and finite element models to predict device stroke and bandwidth.

3.1 Cost Benefits for Head-Based Actuation

Currently, suspension-based actuators must be assembled by a pick-and-place operation in which strips of lead zirconate titanate (PZT) are bonded to hinges in the suspension. Interconnects must then be placed very carefully and accurately so as to avoid shorting the PZT, causing it to crack, or creating a non-Ohmic electrical contact. Even more complexity arises for mounting the slider-based microactuator, where the slider must be mounted on the gimbal, the interconnect traces, and to the actuation platform at the same time. Each pick-and-place, bonding and solder ball bonding operation dramatically increases the assembly time and hence the net cost of an HDD. For head-based actuators, on the other hand, it is possible to directly integrate a microactuator with the head-fabrication process. By microfabricating such an actuator beneath the read/write elements, interconnects can be placed at the trailing edge where they are easily ball-bonded along with all of the other head interconnects, as shown in Fig. 3.1. Because head-based actuators would be microfabricated at the wafer scale, the device fabrication cost would be divided among thousands of heads at once and the net cost per HDD would be much lower than that of current suspension-based actuators. Consequently, the remainder of this thesis will be dedicated to investigating viable head-based actuation schemes.

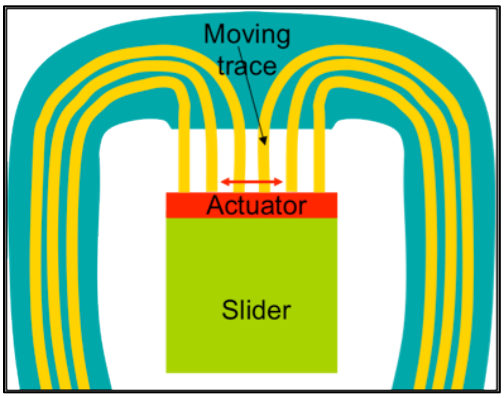

Figure 3.1: For head-based microactuators, interconnects can be bonded at the same time as the rest of the interconnects at the trailing edge of the slider

3.2 Constraints as Posed by Industry

As shown in table 2.2, relatively little research has been conducted on head-based actuation. This may be attributed primarily to the level of difficulty involved in demonstrating the concept in an actual HDD. After fabricating the actuator, the entire head fabrication would also need to be performed so that the concept can be tested using the real readback signal for PES. Furthermore, meeting the necessary conditions for implementation in an actual HDD is very difficult. A list of primary constraints was compiled in collaboration with Western Digital Corporation, shown in table 3.1. Each of these constraints and accompanying rationale will be discussed in detail.

Table 3.1: Constraints posed by Western Digital

Description	Value	Units
1. Minimum servo bandwidth	5	kHz
2. Minimum microactuator stroke	±35	nm
3. Maximum allowable fly-height deviation	±0.3	nm
4. No trailing edge gap in air-bearing surface		
5. Ultra-high fatigue life for actuator and all interconnects		
6. Scalable to large-scale manufacturing processes		

3.2.1 Minimum Servo Bandwidth

The value for minimum servo bandwidth was chosen based on the highest bandwidth that suspension-based microactuators have achieved to date. This was based on the criteria that there must at least be some improvement to warrant the costly transition to head-based actuation. Servo bandwidth is defined here as the

point at which the actuator gain first drops -3dB below the steady-state gain. In actuality, however, this minimum servo bandwidth criterion will depend on the gain of the head-based actuator. This is because suspension-based actuators are still capable of attenuating disturbances above their bandwidths as illustrated in Fig. 3.2. If the gain of the suspension-based actuator is 300 nm/V and the gain of the head-based actuator is 30 nm/V (10 dB less), and if both actuators roll off at 40dB/dec approximately at their bandwidth, then the minimum head-based actuator must have a servo-bandwidth of at least 10 dB (3.16) times the suspension-based bandwidth. This means that, for the situation described above, the minimum servo bandwidth ought to be greater than 15.8 kHz.

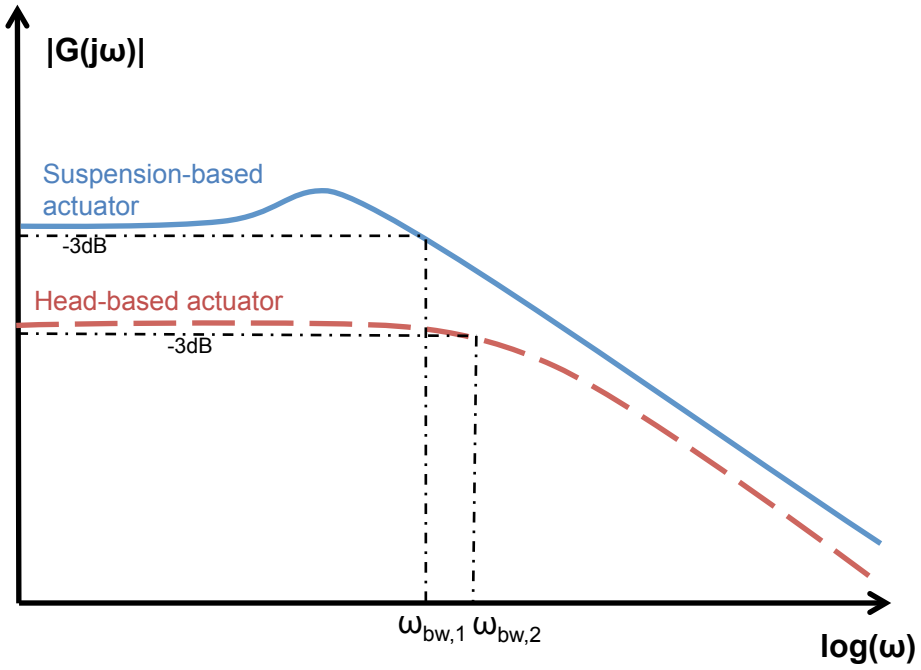

(a)

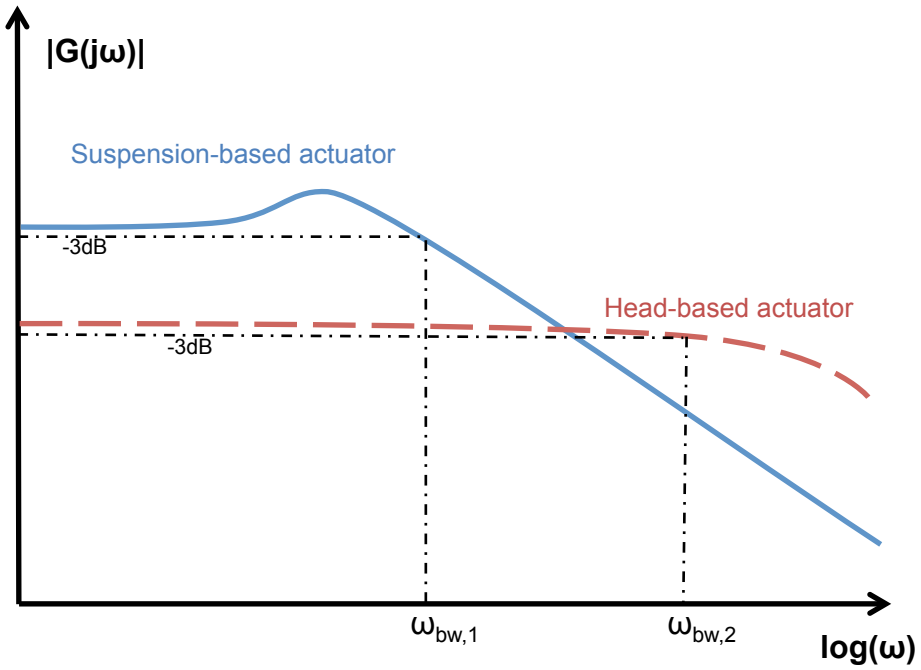

(b)

Figure 3.2: Illustration of a magnitude frequency responses when (a) the head-based actuator has a slightly higher bandwidth than the suspension-based actuator but will have less disturbance rejection and (b) the head-based actuator has higher bandwidth and better disturbance rejection in high frequency regions

3.2.2 Minimum Microactuator Stroke

The minimum microactuator stroke of ±35 nm was based on the forecasted track width of 50 nm if the roadmap in table 1.2 is taken approximately 10 years out. This low-frequency gain is intended to allow for rapid single-track seeks. By performing a 20 nm track offset with the VCM before and after and a nearly instantaneous track seek with the microactuator only, the latency for consecutive track seeks can be reduced from the 1 millisecond range to approximately 20 microseconds, depending on servo sample time. The maximum microactuator voltage was specified as an ancillary to the minimum stroke specification. In order to reduce the chances of electrostatic discharge with the HDD, a maximum potential of ±20V was specified. For a stroke of ±35 nm, this corresponds to a gain of 1.8 nm/V, which is well within the range of gains found in literature for head-based actuators in track-following which are 11 nm/V [39] and 47 nm/V [40].

Recall from chapter 2 that power constraints required that the maximum track-following voltage have a variance less than or equal to 5V and the head-based microactuator gain used for analysis was 20 nm/V. This value was, therefore, the target for head-based actuator design, although the gain based on the minimum stroke constraint could be as low as 1.8 nm/V and, if the bandwidth is high enough, high frequency attenuation could still improve closed-loop performance.

3.2.3 Maximum Allowable Fly-Height Deviation

Fly-height deviation is one of the primary concerns for head-based actuators. Normally, the air-bearing surface (ABS) will damp any fly-height vibrations from the microactuator but with head-based actuators, this vibration occurs between the ABS and the head. If the fly-height stiffness is not sufficiently high, air-flow induced vibration in the vertical direction may cause the head to crash on the disk. It was determined that a deviation of ±10% at a 3 nm fly-height would be small enough to avoid increasing wear at the head-disk interface (HDI). This corresponds to a fly-height deviation of ±0.3 nm.

Furthermore, any imperfections in the actuator geometry may result in an incidental component of actuation in the fly-height direction. For an actuation stroke of ±35 nm, this corresponds to a directionality of approximately 1:100.

3.2.4 No Trailing Edge Gap

The ABS is crucial in passively controlling the fly-height of the head to within several nanometers. To maintain such a tight control on the fly-height, high pressure regions on the order of over 20 atmospheres are localized beneath the read-write head [55]. The shape of the ABS is very important in achieving such high pressures and any gaps or recessions caused by the microactuator would result in a dramatic

loss in the ABS pressure at the head. This will be referred to as a "closed ABS" since, along the track direction, there is no opening or outlet for airflow to escape except at the trailing edge of the slider. The difference between a closed and open ABS is illustrated in Fig. 3.3.

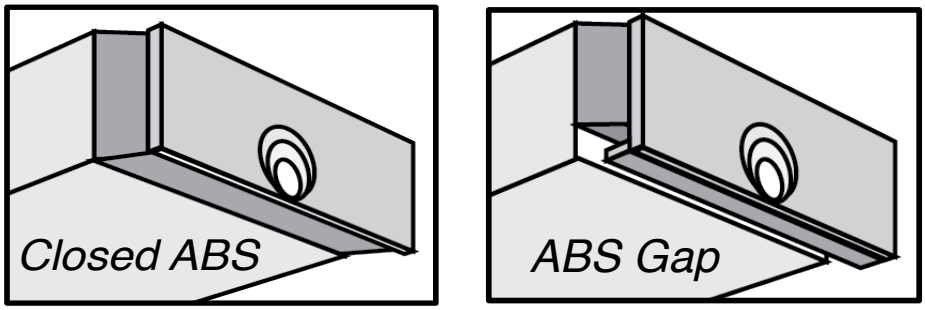

Figure 3.3: Illustration of the difference between a closed and open air-bearing surface (ABS)

3.2.5 Ultra-High Fatigue Life for Actuator and all Interconnects

Fatigue life is an important concern which must be considered early on in the design process because a 100 kHz bandwidth actuator can easily reach the order of 10^{12} cycles in 10,000 hours of operation. Fatigue life considerations may considerably limit the actuation and flexure materials available and hence the possible actuation mechanisms. For example, certain ceramic piezoelectrics like PZT might seem promising until their fatigue life is analyzed and their crack growth rate for the proposed stress levels will need to be taken into account. Also, if a metal flexure or interconnect is proposed, similar considerations must be made.

3.2.6 Scalable to Large-Scale Manufacturing Processes

Wafer-level fabrication is necessary for integration costs to be reduced with head-based actuation. This means that all actuator materials must be either deposited on or bonded to the aluminum titanium carbide (AlTiC) substrate wafer used for head-fabrication. Furthermore, the actuator must be able to survive a series subsequent steps including:

- High-temperature anneal (400°C)
- Several ultra-sonic cleaning steps
- Row bar dicing
- ABS etching
- Slider dicing
- Head-gimbal assembly
- Conductive ball-bonding for interconnects

3.3 Electrostatic Actuators

Electrostatic actuators are very common in MEMS devices because they can be fabricated with almost any conductive materials and in a few very basic fabrication steps. Generally, these devices consist of arrays of capacitive plates utilizing the electrostatic forces of attraction between them to drive the microactuator. A restoring force is added by fabricating bending beams, called flexures, in the same fabrication step as the electrodes. These devices are particularly attractive for MEMS because, as the gap between electrodes decreases to the μm range, the attractive forces become very large.

3.3.1 Linearized Parallel Plate Actuator

The simplest electrostatic actuator in terms of fabrication is the parallel plate actuator. It consists of a plate at some constant voltage and another plate with an oscillating voltage, as schematically depicted in Fig. 3.4(a).

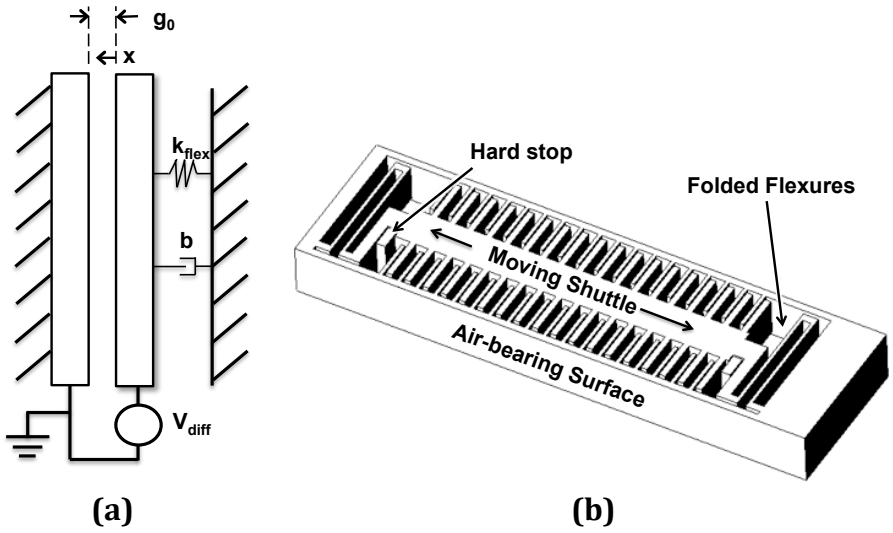

Figure 3.4: (a) Schematic depiction of a parallel-plate actuator and (b) design example for a head-based actuator where the read-write elements would be fabricated on a surface on top of the moving shuttle

The equation of motion for this actuator is given by:

$$m_{head}\ddot{x} = F_e(x, V) - k_{flex}x - b\dot{x} \tag{3.1}$$

where x is the head position, m_{head} is the mass of the head, F_e is the electrostatic force as a function of position and voltage, V, and where b is the total damping in the

actuator. Flexures in beam-bending mode are typically used to provide the spring force with a spring constant given by:

$$k_{flex} = \frac{24EI}{L^3} \tag{3.2}$$

where E is the Young's modulus, I is the bending moment of inertia and L is the beam length. The electrostatic force is given by:

$$F_e(x,V) = \frac{1}{2}\frac{\epsilon A_p N_p}{(g_0 - x)^2}\ (V)^2 \tag{3.3}$$

where V is the voltage differential between the plates, ϵ is the permittivity of free space, A_p is the area of one plate, N_p is the number of plates, and g_0 is the initial (zero spring force) gap between the plates. Note that the electrostatic force is nonlinear with respect to both V_{diff} and x. A linearization filter can be placed on the input, V_{diff}, as follows:

$$V = K_{lin}(x,u)\ v(t)$$

$$K_{lin}(x,V) = \sqrt{\frac{2(g_0 - x)^2}{u(t)\epsilon A_p N_p}} \tag{3.4}$$

and the equation of motion becomes,

$$m_{head}\ddot{x} + b\dot{x} + k_{flex}x = v(t) \tag{3.5}$$

where $v(t)$ has units of Newtons. It must always be positive and can be defined as follows:

$$v(t) = \bar{v} + \tilde{v}\,u(t) \tag{3.6}$$

where $\bar{v}$ and $\tilde{v}(t)$ are constants and $u(t)$ is the non-dimensional control input which must be between -1 and 1 for all t. The values of these terms can be determined from the maximum and minimum voltage,

$$v_{max} = \frac{1}{2}\frac{\epsilon A_p N_p}{g_0 - x_{min}} V_{max} \tag{3.7}$$

$$v_{min} = \frac{1}{2}\frac{\epsilon A_p N_p}{g_0 - x_{max}} V_{min} \tag{3.8}$$

As a design example, an actuator is considered with 37 pairs of parallel plates, each 180um in length and 55 um in width. The parallel plates are separated by an initial gap of 1um and actuation voltages are required to remain within 0.5 and 5 V. The actual input voltage and the linearization gain are both linearly related to the

position, *x*. As expected, Fig. 3.5 shows the resulting inverse-square relationship between the input, *v(t)*, and the linearization gain, K_{lin}.

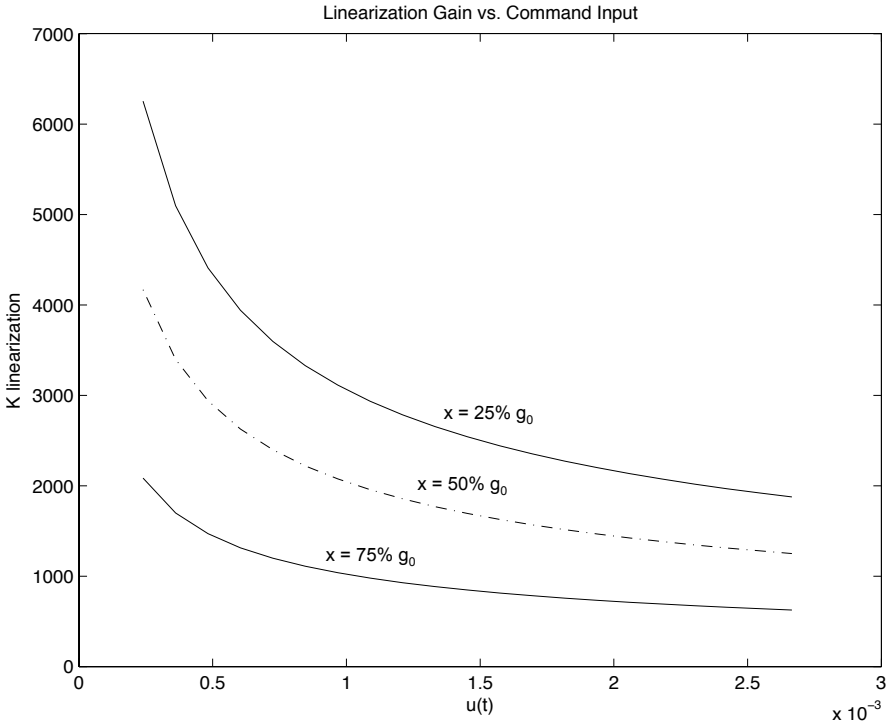

Figure 3.5: The linearization gain, K_{lin}, follows an inverse square relation to the magnitude of the input, u(t), where the dashed line corresponds to the center-gap position, $x_c=g_0/2$, the top solid line represents the minimal position, x_{min}, and the bottom solid line corresponds to the maximal position, x_{max}.

The actuator performance will depend on the static gain and the actuator bandwidth. For the parallel-plate actuator, the bandwidth can be approximated as the natural frequency,

$$\omega_{bw} \cong \omega_n = \sqrt{\frac{k_{flex}}{m_{head}}} \tag{3.9}$$

where the mass of the moving head, m_{head}, is approximately 40 μg, and the flexure stiffness, k_{flex}, will need to be 15.8 kN/m to achieve an actuator bandwidth of approximately 100 kHz. The actuator transfer function will be,

$$G_{pp} = \frac{\tilde{v}}{ms^2+bs+k_{flex}} \tag{3.10}$$

Based on G_{pp} the equivalent static gain can be found at the center-gap position, $x_c=g_o/2$, by the following formula:

$$G_{static} = \frac{\tilde{v}}{k_{flex}} \frac{1}{V_{max}/2} \tag{3.11}$$

As this equation shows, the static gain is inversely proportional to k_{flex} and there will be a trade-off between static gain and bandwidth, which is also dependent on k_{flex}. For the example described above, the static gain is 30 nm/V which meets the target of 20 nm/V discussed earlier.

3.3.2 Comb-Drive Actuator

One of the most difficult aspects of implementing the parallel plate actuator is the linearization filter, K_{lin}, which must be placed on the control input. An alternative approach is to fabricate a comb-drive structure, depicted in Fig. 3.6.

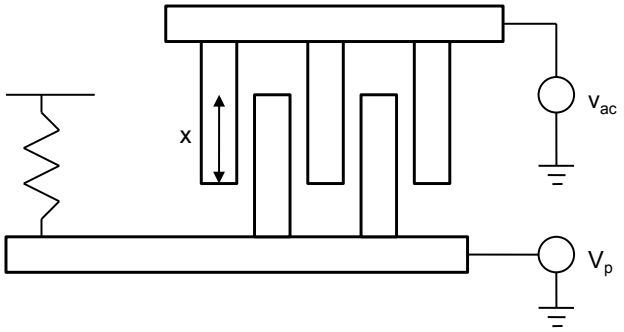

Figure 3.6: Schematic depiction of comb-drive structure

The electrostatic force is a result of the minimization of electrostatic energy which favors large values of x which will increase the overlap between fingers. Consequently, if $V_p >> v_{ac}$, and if fringing fields are neglected, the electrostatic force becomes linear with respect to the control input v_{ac} as follows:

$$F_e = \frac{\epsilon_0 t N_f}{d} V_P^2 - 2V_P \frac{\epsilon_0 t N_f}{d} v_{ac} \tag{3.12}$$

where N_f is the number of fingers, t is the thickness of each finger, and d is the gap between fingers. For a head-based actuator, the equation of motion can be rewritten,

$$m_{head}\ddot{x} + b\dot{x} + k_{flex}x = C_1 + C_2 v_{ac} \tag{3.13}$$

with constants $C_1 = \frac{\epsilon_0 t\, N_f}{d} V_P^2$ and $C_2 = -2V_P \frac{\epsilon_0 t\, N_f}{d}$. The actuator transfer function will be,

$$G_{cd} = \frac{-C_2}{ms^2+bs+k_{flex}} \tag{3.14}$$

and the static gain will be,

$$G_{static} = \frac{2V_P\epsilon_0 t\, N_f}{k_{flex}\, d} \tag{3.15}$$

As an example, consider a comb-drive actuator with 100 fingers, each 50 μm thick with 1 μm separation between them and a bias voltage, V_P, of 20V. If the same flexures are used as in the analysis of the parallel plate, a total static displacement gain of 0.1 nm/V is calculated. This demonstrates that although the response of a comb drive is linear, the static displacement is much smaller than the parallel plate actuator and is not sufficient to reach the 20 nm/V target.

3.3.3 Differential Parallel Plate Actuator

The differential parallel plate actuator was developed in an attempt to achieve both linearity and large displacement gains [56]. Deep trench isolation is used to separate each finger on the driving side into a positive and negative electrode, as shown in Fig. 3.7.

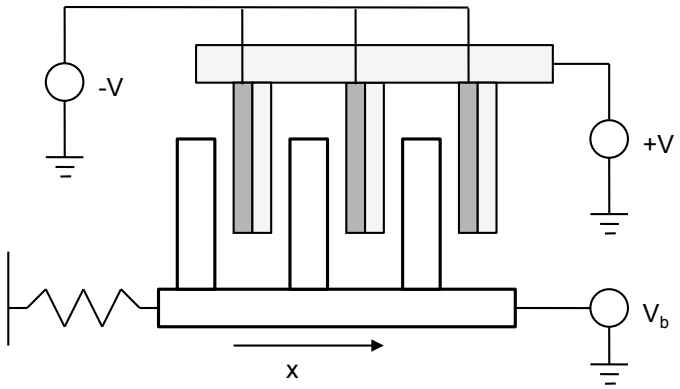

Figure 3.7: Deep trench isolation is used to separate each finger into two electrodes for the differential parallel plate actuator

As a result using this differential configuration, the electrostatic force becomes,

$$F_e = -\frac{1}{2}\epsilon_0(V-V_b)^2\left(\frac{tL_dN_f}{(g_0+x)^2}\right) + \frac{1}{2}\epsilon_0(-V-V_b)^2\left(\frac{tL_dN_f}{(g_0-x)^2}\right) \tag{3.16}$$

where t is the finger thickness, L_d is the finger overlap length, g_0 is the initial gap between fingers, N_f is the number of fingers and V_b is the bias voltage. It has been shown that this force can be linearized about $x=0$ to yield the following approximate electrostatic force [56],

$$F_e = 2\epsilon_0 V_b \left(\frac{tL_d N_f}{{g_0}^2}\right)\delta V - 2\epsilon_0 V_b^2 \left(\frac{tL_d N_f}{g_0^3}\right)\delta x \tag{3.17}$$

where $V<<V_b$, δV is a small perturbation in driving voltage and δx is a small displacement. Under these conditions, the equation of motion becomes

$$m_{head}\ddot{x} + b\dot{x} + \left(k_{flex} + C_1\right)x = C_2 v_{ac} \tag{3.18}$$

where constants $C_1 = 2\epsilon_0 V_b^2 \left(\frac{tL_d N_f}{g_0^3}\right)$ and $C_2 = 2\epsilon_0 V_b \left(\frac{tL_d N_f}{{g_0}^2}\right)$. The actuator transfer function will be,

$$G_{cd} = \frac{C_2}{ms^2 + bs + (k_{flex} + C_1)} \tag{3.19}$$

and the static gain will be,

$$G_{static} = \frac{C_2}{(k_{flex} + C_1)} \tag{3.20}$$

As an example, consider a differential parallel plate actuator with 100 fingers, each is 50 μm thick with, 100 μm overlap, 1 μm separation between them and a bias voltage, V_b, of 20V. For these parameters, the static gain becomes 11 nm/V. While this does not quite meet the aforementioned target of 20 nm/V as easily as with the parallel plate actuator, the necessary twofold increase could reasonably be achieved by slightly increasing the number of fingers, the overlap and finger thickness. The advantage of this actuator is that the nonlinearities and resulting hysteretic and "negative quality factor" effects [57] have been removed without the need of a linearizing filter as was the case with the parallel plate actuator.

3.3.4 Electrostatic Actuators as Head-Based Devices

It has been shown that parallel plate actuators can easily meet the static displacement target of 20 nm/V with a bandwidth of 100 kHz and, with some careful design, differential parallel plate actuators can also meet this target; however, comb drive actuators are much too weak. These results are summarized in table 3.2.

Table 3.2: Performance comparison of the three electrostatic actuator designs considered

Actuation Mechanism	Static Displacement	Bandwidth
Parallel Plate	30 nm/V	100 kHz
Comb Drive	0.1 nm/V	100 kHz
Differential Parallel Plate	10 nm/V	100 kHz

Thus far, only the first two constraints, static displacement and bandwidth, have been discussed. The third constraint, fly-height deviation, can easily be met by a proper design of the flexure geometry to achieve the correct directionality. The fourth constraint, however, that of the closed ABS, poses a problem for electrostatic actuators, as it does for nearly all actuation mechanisms. In order to maintain a closed ABS, the head cannot be fully separate from the rest of the slider body. There must at least be a shear wall or they may even be an elastomeric fill throughout the structure. Since this is a problem common to all actuation schemes, it will be discussed further in a latter section. The ABS constraint may be more stringent for electrostatic actuators, though, because they also need to be protected on all sides from particles in the HDD which can short-circuit fingers together and cause catastrophic failure. All of these details will be discussed later.

With regard to the last two constraints, electrostatic actuators have a clear benefit. Because they can be fabricated out of nearly any conductive material with a wide variety of flexure geometries, their fatigue properties are easily tuned for the device requirements. Furthermore, the relative simplicity of electrostatic actuators fabrication makes them much easier to implement along with subsequent processes as has been done in the past for merged MEMS and CMOS processes [58].

3.4 Piezoelectric Actuators

When a voltage is applied across a dielectric material, it can be polarized by electron cloud displacement and ionic displacement with respect to the rest of the material structure. Therefore, when a voltage is applied across a piezoelectric material, the material deforms in an attempt to minimize the Gibbs free energy according to the inverse piezoelectric effect. The polarization may also vary with temperature according to the pyroelectric effect. For many materials, spontaneous polarization occurs below a certain temperature, referred to as the Curie temperature. These ferroelectric materials tend to have relatively large piezoelectric responses but they also exhibit hysteresis and loss of piezoelectricity above the Curie temperature. In recent decades, however, there has been an explosion of available ferroelectric materials which have very large force constants and are increasingly stable at elevated temperatures as high as 350 °C [59]. Generally, these

materials are characterized according to the following constitutive equations in isothermal ($\Delta T \cong 0$) form [60]:

$$\Delta S_\alpha = \alpha_\alpha^E \, \Delta T + s_{\alpha\beta}^E \, \Delta T_\beta + d_{i\alpha} \, \Delta E_i \tag{3.21}$$

$$\Delta D_i = p_i^T \, \Delta T + d_{i\alpha} \, \Delta T_\alpha + \epsilon_{ik}^T \, \Delta E_k \tag{3.22}$$

On the left side, S_α and D_i are the strain and electric displacement vectors, respectively. On the right, T, $T_{\alpha\beta}$, and E_{ik} are the temperature, stress, and electric field vectors, respectively. The associated coefficient matrices are summarized in table 3.3.

Table 3.3: Table of dielectric coefficients

Coefficient	Description	Assumption
$\alpha_\alpha{}^E$	*Thermal expansion coefficient*	$\Delta E_{ik} = 0$
$s_{\alpha\beta}{}^E$	*Elastic compliance*	$\Delta E_{ik} = 0$
$d_{i\alpha}$	*Piezoelectric constants*	*None*
$p_i{}^T$	*Pyroelectric coefficients*	$\Delta T_{\alpha\beta} = 0$
$\varepsilon_{ik}{}^T$	*Permittivies*	$\Delta T_{\alpha\beta} = 0$

The coefficients which are of primary interest for microactuators are elastic compliances ($s_{\alpha\beta}{}^E$), piezoelectric constants ($d_{i\alpha}$), and directional permittivity ($\varepsilon_{ik}{}^T$). For a standard poled ferroelectric material at a constant temperature and when zero-force boundary conditions are assumed, Eq. (3.21) becomes,

$$\begin{Bmatrix} S_1 \\ S_2 \\ S_3 \\ S_4 \\ S_5 \\ S_6 \end{Bmatrix} = \begin{bmatrix} 0 & 0 & d_{31} \\ 0 & 0 & d_{32} \\ 0 & 0 & d_{33} \\ 0 & d_{24} & 0 \\ d_{15} & 0 & 0 \\ 0 & 0 & 0 \end{bmatrix} \begin{Bmatrix} E_1 \\ E_2 \\ E_3 \end{Bmatrix} \tag{3.23}$$

where S_α corresponds to the strain in the α^{th} direction and E_k corresponds to the electric field in the k$^{\text{th}}$ direction. These subscripts relate to the direction of remnant polarization, **P**, as shown in Fig. 3.8.

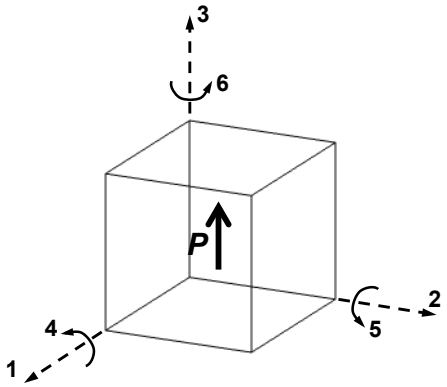

Figure 3.8: Numbered tensor directions with respect to remnant ferroelectric polarization vector ***P***

3.4.1 Transverse Mode (d_{31}) Piezoelectric Actuator

Very large strokes can be achieved with thin (3-direction) and long (1-direction) strips of piezoelectric material [61] [62] poled and driven from the top and bottom (3-direction), as schematically depicted in Fig. 3.9(a). When the top and bottom surfaces are unconstrained under these conditions, Eq. (3.21) can be simplified to find the change in length,

$$S_1 = d_{31}E_3 \tag{3.24}$$

Recall that axial strain, S_1, is defined as change in length divided by nominal length, $\frac{\Delta L}{L}$, and that for a uniform field, $E_3 = \frac{dV}{dx} = \frac{V}{t}$, and Eq. (3.24) becomes,

$$\Delta L = \frac{d_{31}L}{t}\, V \tag{3.25}$$

This is called the unblocked displacement because it is the displacement of the piezoelectric strip without any force applied. To determine the blocking force, which is the force required to keep the displacement at zero, the axial strain, S_1, must be set to zero in Eq. (3.21), resulting in the following relation:

$$T_1 = -\frac{d_{31}\,\Delta E_3}{s_{11}^E} \tag{3.26}$$

Recall that axial stress, T_1, is defined to be the axial force divided by the area and the compliance, s_{11}^E, is the inverse of the Young's modulus, therefore, the force can be shown to be:

$$F_1 = -wE_{pzt}d_{31}V \tag{3.27}$$

where w is the width of the strip (2-direction) and E_{pzt} is the Young's modulus for the piezoelectric material. For the design example considered here, this material will be lead zirconate titanate (PZT).

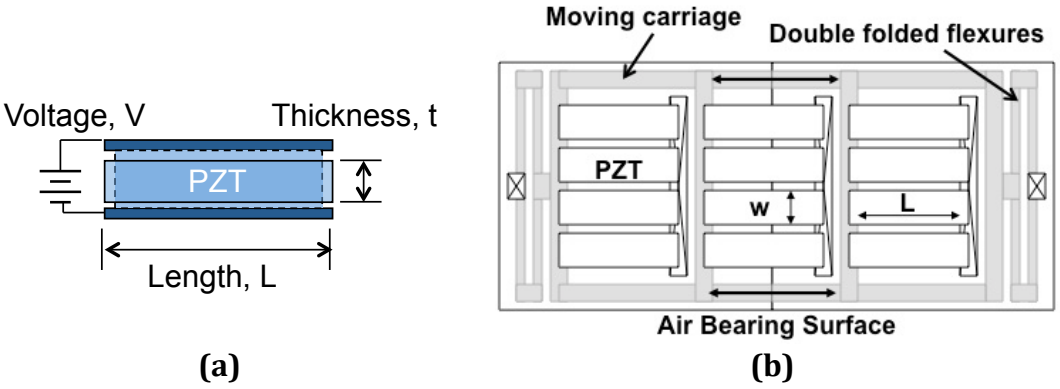

Figure 3.9: (a) Schematic depiction of d_{31} contraction and (b) example design for a d_{31} transverse mode piezoelectric actuator

As a design example, consider a head-based actuator similar to what is depicted in Fig. 3.9(b), with 12 strips of PZT-5H. Each strip is 10 μm wide, 200 μm long, and 3 μm thick. The material has a Young's modulus of 50 GPa and and a d_{31} constant of -265 pm/V. As with other actuators, the total mass of the moving carriage and head, m_{head}, is approximately 40 μg. For this example, the equation of motion will be given by:

$$m_{head}\ddot{x} = F_{pzt}(x, V) - k_{flex}x - b\dot{x} \tag{3.28}$$

where the net piezoelectric force, $F_{pzt}(x, V)$, can be found by interpolating between the unblocked displacement from Eq. (3.25) and the blocking force from Eq. (3.27) to obtain,

$$F_{pzt}(x, V) = F_1 - \frac{F_1}{\Delta L}x = -w\, E_{pzt} d_{31}\, V + \frac{wt}{L} E_{pzt}\, x \tag{3.29}$$

The resulting equation of motion is:

$$m_{head}\ddot{x} + b\dot{x} + (k_{flex} - C_1)x = C_2 V \tag{3.30}$$

where $C_1 = \frac{wt}{L} E_{pzt} N_s$, $C_2 = w\, E_{pzt} N_s d_{31}$, and N_s is the number of strips. Note that C_1 is simply the axial stiffness of the PZT strip. The actuator transfer function will be,

$$G_{cd} = \frac{C_2}{ms^2 + bs + (k_{flex} - C_1)} \tag{3.31}$$

and the static gain will be,

$$G_{static} = \frac{C_2}{(k_{flex} - C_1)} \tag{3.32}$$

For the example described above, k_{flex} must be increased from previous values by the value of C_1 in order to obtain the required 100 kHz bandwidth. This means the flexure stiffness must be 23.3 kN/m. The static gain will then be 100 nm/V which much higher than the target of 20 nm/V. With regard to ultra-high fatigue life, the peak dynamic tensile strength of PZT-5H is rated at 4000 psi, or 28 MPa [59]. The blocked tensile stress at 5V is given by Eq. (3.26) to be 22 MPa, therefore, the strips will always be below this high-cycle fatigue limit.

As with the aforementioned electrostatic actuators, the primary concern for transverse mode piezoelectric actuators is that they will require an open ABS. This can be overcome by adding a shear wall at the ABS or incorporating an elastomeric fill, as will be discussed later.

3.4.2 Shear Mode (d_{15}) Piezoelectric Actuator

It was first proposed that the portion of the ABS which must be sheared could be comprised of piezoelectric material driven in the d_{15} mode as depicted in Fig. 3.10(a). This concept was first proposed in a patent by TDK Corporation [41]. Preliminary testing, however, showed that the directionality of a d_{15} mode actuator will be less than 1:10, meaning that for a stroke of 20 nm/V, the fly-height deviation will be greater than 10 nm at 5V whereas industry has specified that it can be no greater than 0.3 nm. It was therefore proposed that dielectric flexures be incorporated into the design as shown in Fig. 3.10(b). These flexures can be designed to be many times more stiff in the fly-height direction than the piezoelectric material while remaining flexible in the actuation direction, yielding a very high directionality.

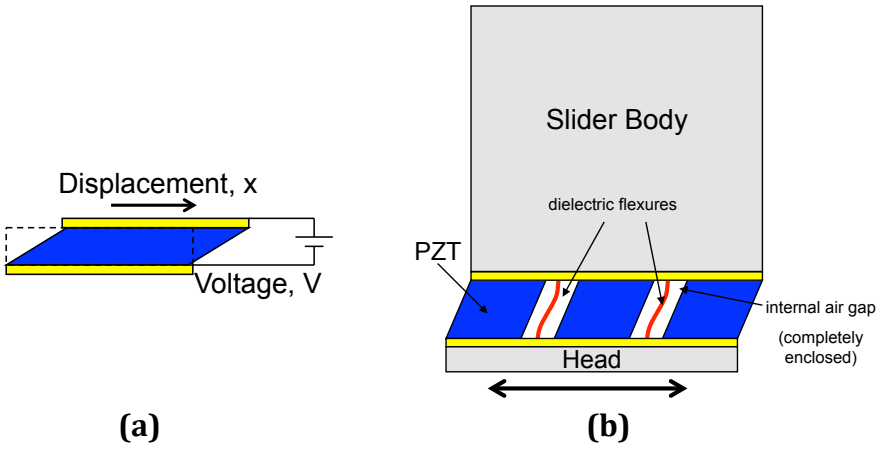

Figure 3.10: (a) Schematic depiction of d_{15} shear (b) example of shear-mode actuator design from the top view with internally buried flexures for directionality

When a uniform potential is applied along the poling direction and the piezoelectric material is allowed to deform freely with no force applied, then Eq. (3.21) can be simplified to,

$$S_5 = d_{15}E_1 \tag{3.33}$$

Recall that shear strain, S_5, can be defined as the ratio of deformation along the shear axis to the material thickness along the orthogonal axis, $\frac{x}{t}$, and that for a uniform field, $E_1 = \frac{dV}{dy} = \frac{V}{t}$, therefore, t cancels and Eq. (3.24) becomes,

$$\Delta L = d_{15}\, V \tag{3.34}$$

The result is that the displacement does not depend on the geometry of the piezoelectric element but solely on the applied voltage and material property, d_{15}. This result implies that for a shear-mode actuator, the static gain cannot be greater than the d_{15} constant, with reported values only as high as about 740 (0.740 nm/V) for PZT-5H [59]. This is significantly less than the target of 20 nm/V. One proposed method for increasing the static gain is by multi-stacking in such a way that with a stack of 30 stacks of PZT-5H, this target can be reached; however, this proves to be infeasible once wafer-scale manufacturing considerations are taken into account.

For wafer-scale manufacturing, the piezoelectric material must go through several high-temperature annealing processes in the subsequent head fabrication. Even for the materials with high temperature stability, Curie temperatures range around 350°C while the head fabrication requires annealing around 400°C. Consequently, the piezoelectric material must be poled after head-fabrication is completed. For d_{13} and d_{33} actuators, where the poling and the driving fields are aligned, the same electrodes can be used for poling as for actuation. In the case of

the d_{15} shear mode actuators, however, separate electrodes will need to be used, as shown in Fig. 3.11. As this figure shows, poling must occur much later than the deposition of driving electrodes and, hence, it is convenient to utilize the internal flexures as poling electrodes; however, finite-element analysis of the poling fields reveals that large portions of the material will either not be poled sufficiently or they will be poled in the wrong direction, as seen in Fig. 3.12(a). Based on the finite element mesh considered in Fig. 3.12(b) below, the unblocked displacement was estimated to be reduced from 0.74 nm to 0.2 nm/V.

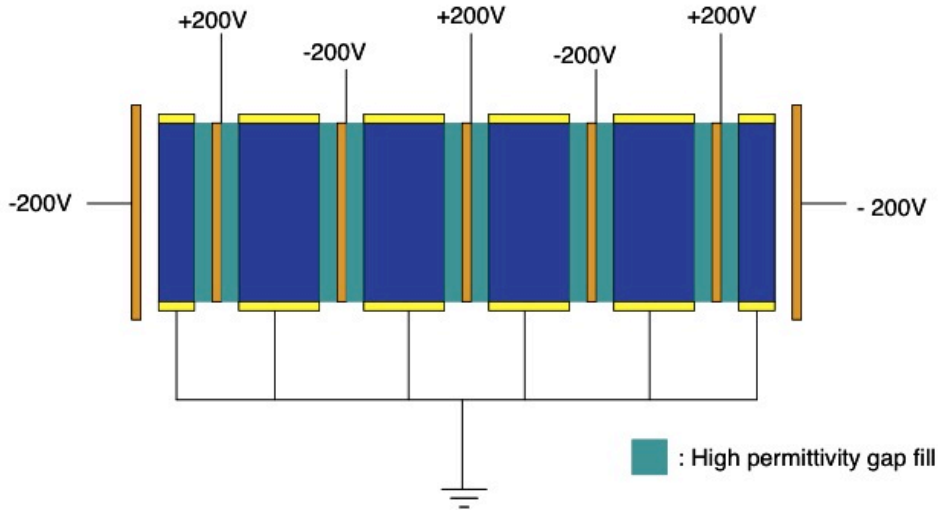

Figure 3.11: Using a high permittivity material, internally buried flexures can double as poling electrodes for the shear-mode actuator

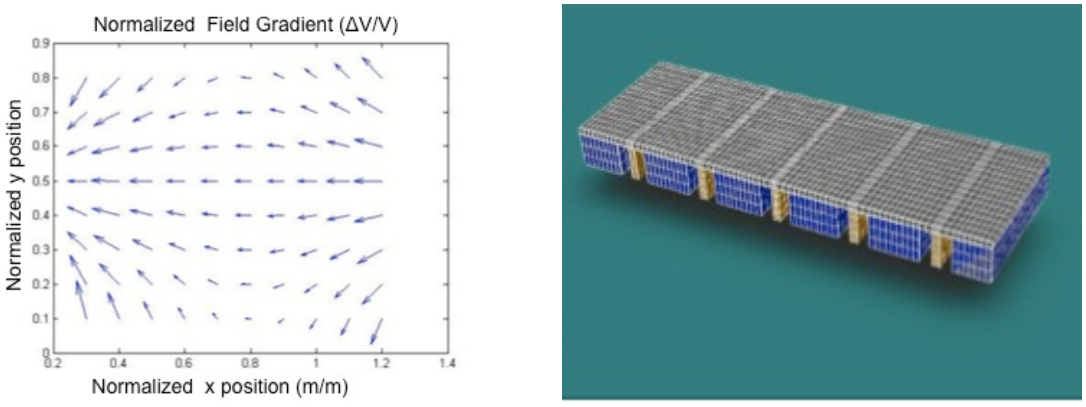

(a) **(b)**

Figure 3.12: (a) Non-ideal poling fields due to grounded top and bottom electrodes and (b) finite element model subdivided into different polarization regions

Overall, shear mode actuators appear to be infeasible for head-based actuation based on the piezoelectric materials which are currently available. This is due to the limited static displacement from d_{15} constants which are still too small. Also, the Curie temperatures are still too low for displacement to be increased by multi-layering because the poling step requires aspect ratios which are very close to a 1:1 aspect ratio. Until the d_{15} constant and the Curie temperature are increased significantly with new materials, the aforementioned design is unlikely to be implemented by industry.

3.4.3 Quasi-Shear Mode (d_{33}) Piezoelectric Actuator

The final piezoelectric actuation direction to be considered is the longitudinal direction, in which the poling field, driving field, and displacement are all aligned along the same axis (3 direction). Under these conditions and when the top and bottom surfaces are unconstrained, Eq. (3.21) simplifies to:

$$S_3 = d_{33} E_3 \tag{3.35}$$

Again, axial strain, S_3, is defined as change in length divided by nominal length, $\frac{\Delta L}{L}$, and for a uniform field, $E_3 = \frac{dV}{dx} = \frac{V}{L}$, therefore, L cancels and Eq. (3.24) becomes,

$$\Delta L = d_{33}\, V \tag{3.36}$$

As with the shear mode actuator, unblocked displacement will not be a function of the geometry of the piezoelectric material and the static displacement gain will only be a function of the d_{33} constant and the applied voltage. The largest d_{33} constants observed are, again, for PZT-5H, in the range of 590 pC/N , which results in a static displacement gain of 0.59 nm/V which is, again, much too small to meet the 20 nm/V target. Unlike the shear mode actuator, however, the poling electrodes can be the same as the driving electrodes; therefore, it is possible to use multi-stack of 33 stacks to reach the target displacement.

The primary difficulty in designing a head-based actuator using the longitudinal mode is that the actuation occurs in the incorrect direction. Generally, for thin-film fabrication methods, electrodes are deposited on the plane of the wafer and therefore the longitudinal direction is out-of-plane from the wafer, as depicted in Fig. 3.13(a). Accordingly, a hinge geometry was proposed to convert longitudinal motion into a quasi-shear motion as shown in Fig. 3.13(b)-(c).

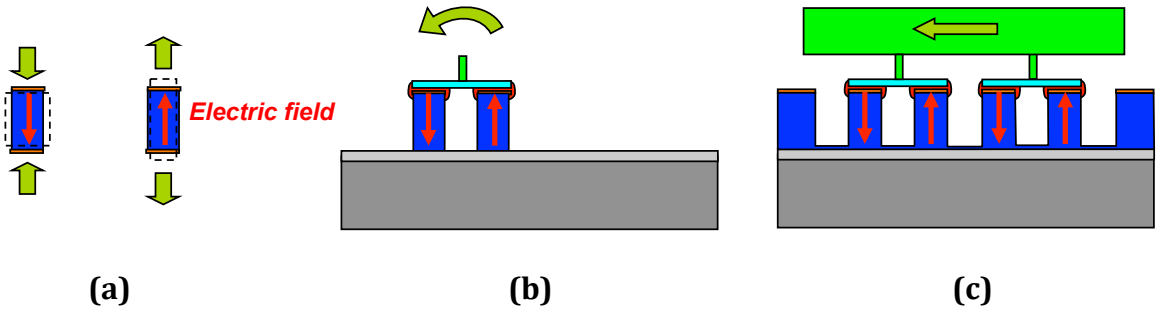

Figure 3.13: (a) Longitudinal mode produces displacement in the out-of-plane direction for which (b) a hinge structure was designed to convert displacement to rotational motion and then (c) to a quasi-shear motion

The shear displacement of this quasi-shear actuator will depend on the dimensions of the piezoelectric material and of the hinge structure. These dimensions can be optimized to achieve the maximum possible displacement for a given set of constraints. Such an optimization requires an analytical solution based on the mechanics of the entire structure. At the same time, an analytical solution will require many simplifying assumptions and, therefore, it is also useful to analyze this structure by the finite element method. Both of these will be demonstrated below and compared for model verification purposes.

3.4.3.1 Static Piezoelectric Beam Deflection Model

First, an analytical model will be derived with static beam equations based on strain energy equations modified to incorporate piezoelectric energy. The dynamic beam equations are unnecessary for this analysis because the mass of the device is much less than the 40 µg mass of the head. Static beam equations will henceforth be derived based on the sign convention shown in Fig. 3.14.

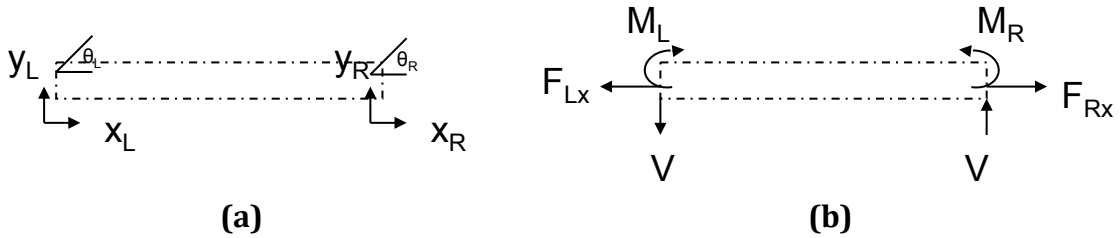

Figure 3.14: Schematic of beam elements with (a) translational/rotational deflections and (b) forces/moments

The static deflection energy associated with axial force, P, moment, M, and transverse force, V is given to be [63]:

$$du_{axial}(x) = \frac{1}{2}P\delta_x = \frac{1}{2}P\left(\frac{P\,dx}{AE}\right) = \frac{P^2}{2EA}dx \tag{3.37}$$

$$du_{bending}(x) = \frac{1}{2}M\theta = \frac{1}{2}M\left(\frac{Mdx}{EI}\right) = \frac{M^2}{2EI}dx \tag{3.38}$$

$$du_{transverse}(x) = \frac{1}{2}V\delta_y = \frac{1}{2}V\left(\frac{f_x\tau_{yz}}{G}\right) = \frac{1}{2}V\left(\frac{6}{5}\frac{V/A}{G}\right) = \frac{3V^2}{5GA}dx \tag{3.39}$$

Based on Eq. (3.22), the static piezoelectric energy associated with a longitudinally applied potential, V, can written,

$$du_{piezo}(x) = \frac{1}{2}D_3E_3A = \frac{1}{2}\left(\epsilon_{33}\frac{V}{L} + d_{33}\frac{F}{A}\right)\left(\frac{V}{L}\right)A = \frac{\epsilon_{33}AV^2}{2L^2} + \frac{d_{33}FV}{2L} \tag{3.40}$$

As expected, the piezoelectric constant acts as a cross-coupling coefficient between force and potential. According to Castigliano's Theorem, displacement in the i^{th} direction and location is equal to the partial derivative of strain energy with respect to a fictitious force, Q_i, applied in the corresponding location and direction. Accordingly, the axial, shear and rotational deflection are defined as follows:

$$\Delta_x = \frac{\partial}{\partial Q_x}\left(U_{axial} + U_{bending} + U_{transverse} + U_{piezo}\right) \tag{3.41}$$

$$\Delta_y = \frac{\partial}{\partial Q_y}\left(U_{axial} + U_{bending} + U_{transverse} + U_{piezo}\right) \tag{3.42}$$

$$\Delta_\theta = \frac{\partial}{\partial Q_\theta}\left(U_{axial} + U_{bending} + U_{transverse} + U_{piezo}\right) \tag{3.43}$$

where U_n is the total energy of deflection mode n which corresponds to the integral of $du_n(x)$ along the length of the beam. Consequently, the deflections will be:

$$\Delta_x = P\frac{L}{AE} + Vd_{33} \tag{3.44}$$

$$\Delta_y = V\frac{L^3}{3EI} + M_R\frac{L^2}{2EI} + V\frac{6L}{5GA} + L\theta_L \tag{3.45}$$

$$\Delta_\theta = V\frac{L^2}{2EI} + M_R\frac{L}{EI} \tag{3.46}$$

where integrals are taken from the left node, L, to the right node, R. M_R is the moment on the right and $L\theta_L$ is the transverse displacement due to the rotation of the beam. These equations are then each applied to the five beam elements in Fig. 3.15.

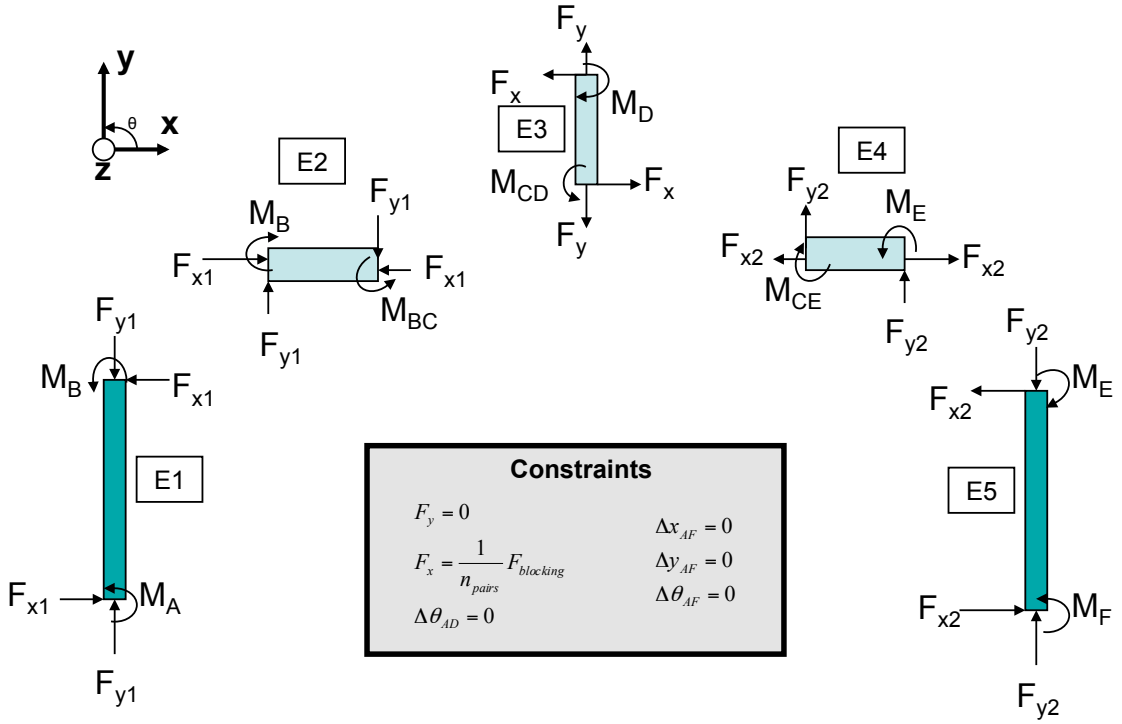

Figure 3.15: The hinge structure of the quasi shear mode actuator can be broken down into five beam elements with several global constraints

Given constraints in Fig. 3.15, the analytical solution for shear-mode deflection, δ_x was derived as a function of driving voltage V:

$$\delta_x = f\left(L_i, b_i, h_i, E_i, G_i, d_{33}^i, F_x, V\right)_{i=1:5} \tag{3.47}$$

where, for each element i, L_i is the length, b_i is the width, h_i is the height, E_i is the Young's modulus, G_i is the shear modulus, d^i_{33} is the longitudinal piezoelectric constant. With a blocking force, $F_x = 0$, the unblocked displacement was found using the symbolic equation solver in Mathematica.

As an illustrative design, parameters from table 3.4 were used to maximize the unblocked deflection with respect to h_2, the height of elements 2 and 4. The parameters in table 3.4 are based on the actual dimensions of the prototype discussed in chapter 4 and they are constrained by the prototype fabrication process; however, much more optimization can be performed on this design once constraints for large-scale manufacturing are identified more fully. The large d_{33} value is also based on the prototype, which uses the electrostrictive material, lead magnesium niobate lead titanate (PMN-PT), as will be discussed later.

Table 3.4: Quasi shear mode design parameters

Dimension	Value	Units	Property	Value	Units
L_1	250	µm	E_1	60	Gpa
L_2	20	µm	E_2	80	Gpa
L_3	12	µm	E_3	400	Gpa
L_4	20	µm	E_4	80	Gpa
L_5	250	µm	E_5	60	Gpa
b_1	300	µm	G_1	200	Gpa
b_2	300	µm	G_2	200	Gpa
b_3	300	µm	G_3	80	Gpa
b_4	300	µm	G_4	200	Gpa
b_5	300	µm	G_5	200	Gpa
h_1	70	µm	d_{33}^{5}	1500	pm/V
h_2	(h2)		d_{33}^{5}	1500	pm/V
h_3	4	µm	$d_{33}^{2\text{-}4}$	0	
h_4	(h2)				
h_5	70	µm			

For the given parameters, the unblocked displacement was found to increase monotonically with increasing h_2, therefore, the height of these beams were set to the practical fabrication limit of 15 µm, as discussed in chapter 4. The resulting unblocked displacement is 1.8 nm/V, which corresponds to a mechanical amplification factor of 1.2 from longitudinal displacement to shear motion. Furthermore, a stiffness of $k_x = 170\ kN/m$ is calculated from blocking force, F_x, when $\delta_x = 0$. This gives a first resonance at,

$$\omega_1 = \sqrt{\frac{nk_x}{m_{head}}} = 5\ MHz \tag{3.48}$$

where n is three, the number of pairs of pillars in the prototype. This gives an estimate of the bandwidth which well exceeds the targeted 100 kHz bandwidth. Thus, for the frequencies of interest, the static gain will simply be unblocked displacement of 1.8 nm/V. Again, this is much too low for the target of 20 nm/V and multilayers will be necessary in each pillar.

3.4.3.2 Electro-Mechanical Finite Element Model

The analytical solution was verified with a two-dimensional finite element model in COMSOL according to the parameters in table 3.4. The boundary conditions were applied as shown below in Fig. 3.16(a) and this yielded a shear displacement of 1.5 nm/V, shown in Fig. 3.16(b).

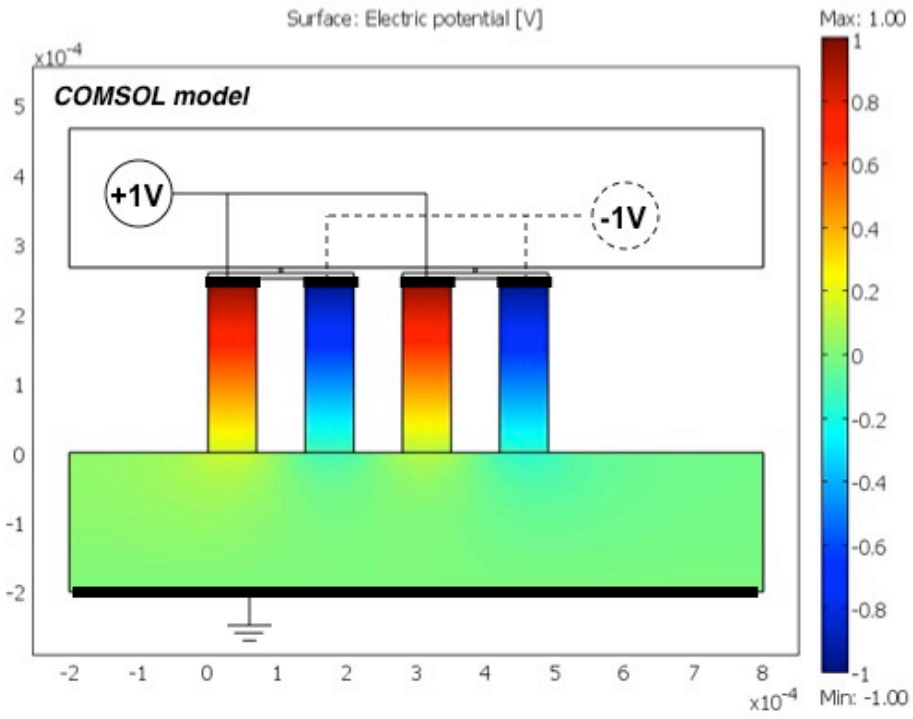

(a)

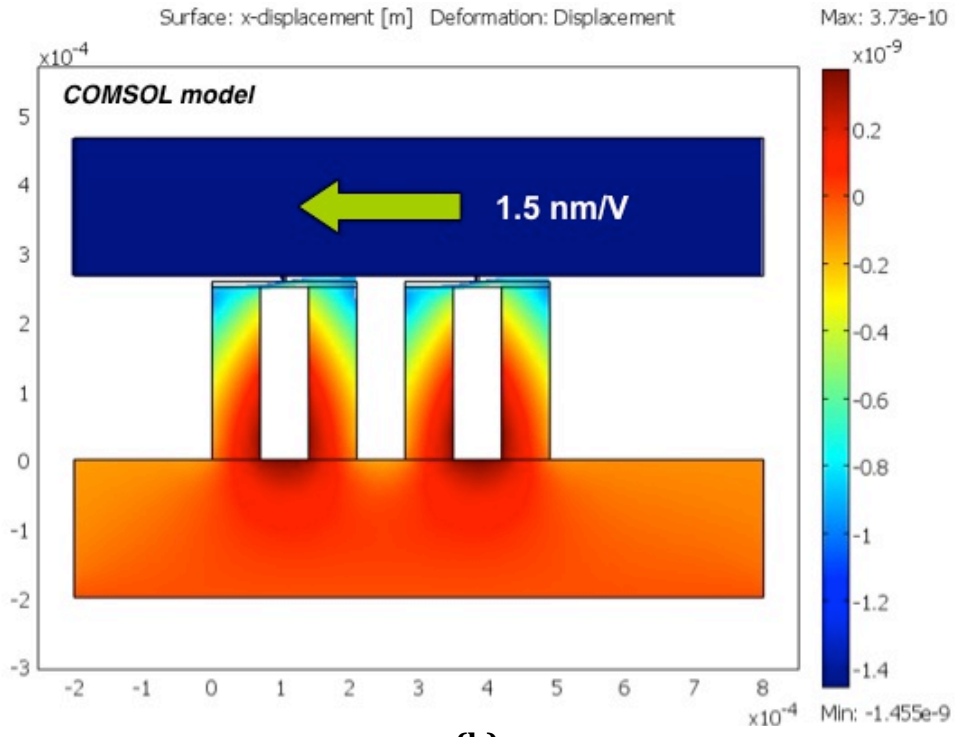

(b)

Figure 3.16: (a) Boundary conditions and (b) shear deformation of COMSOL Finite Element model of quasi shear mode actuator

3.5 Addressing the Air Bearing Surface Gap

One of the recurring flaws with the head-based actuators discussed thus far is that they introduce a gap in the ABS. The piezoelectric shear mode (d_{15}) actuator was the only actuator which did not introduce such a gap. As discussed previously, though, it does not meet the static gain target of 20 nm/V. And all of the remaining head-based microactuators that have been proposed thus far fail to meet this constraint. In this section, three options will be discussed to addressed the ABS gap constraint:

1. Depositing an elastomeric fill
2. Fabricating a shear wall on the ABS
3. Leaving a controlled nano-gap

3.5.1 Depositing an Elastomeric Fill

Perhaps the most straightforward approach, in terms of fabrication complexity, would be to completely fill all open gaps in the actuator with an ultra-low modulus fill material. Then, after wafers are diced into row bars and again into individual sliders, there will be no gap remaining in the ABS. Of course, this will lead to many complications such as patterning the ABS with an elastomeric film there, dicing such a material along with the AlTiC substrate, and the temperature stability of the fill material at annealing temperatures around 400°C. For this reason, it seems much more plausible to introduce the fill as a liquid via capillary action at the very last fabrication step, after annealing, ABS patterning, and final slider dicing. For conventional rubbers, this would require a high temperature vulcanization step which would damage the head but there are some materials, such as silicone, which can be vulcanized at room temperature. Moreover, many elastomeric MEMS compounds can be cross-linked with ultra-violet light. The first determining factor in determining a viable material will be maximum allowable modulus to allow for sufficient actuator motion.

Since an elastomeric film would interfere with the workings of an electrostatic actuator, only the transverse piezoelectric actuator was considered as a viable option for elastomeric filling. A three-dimensional model was created based on the design from section 3.4.1 and the open areas were filled with a very low-modulus material, vulcanized natural rubber, with Young's modulus of 1.5 MPa and shear modulus of 5 GPa. The resulting von Mises stress distribution is shown in Fig. 3.17. Note that for such a low-modulus fill, the stress is carried predominantly by the anchors and PZT strips and the compliance of natural rubber is sufficient to allow for unhindered actuation.

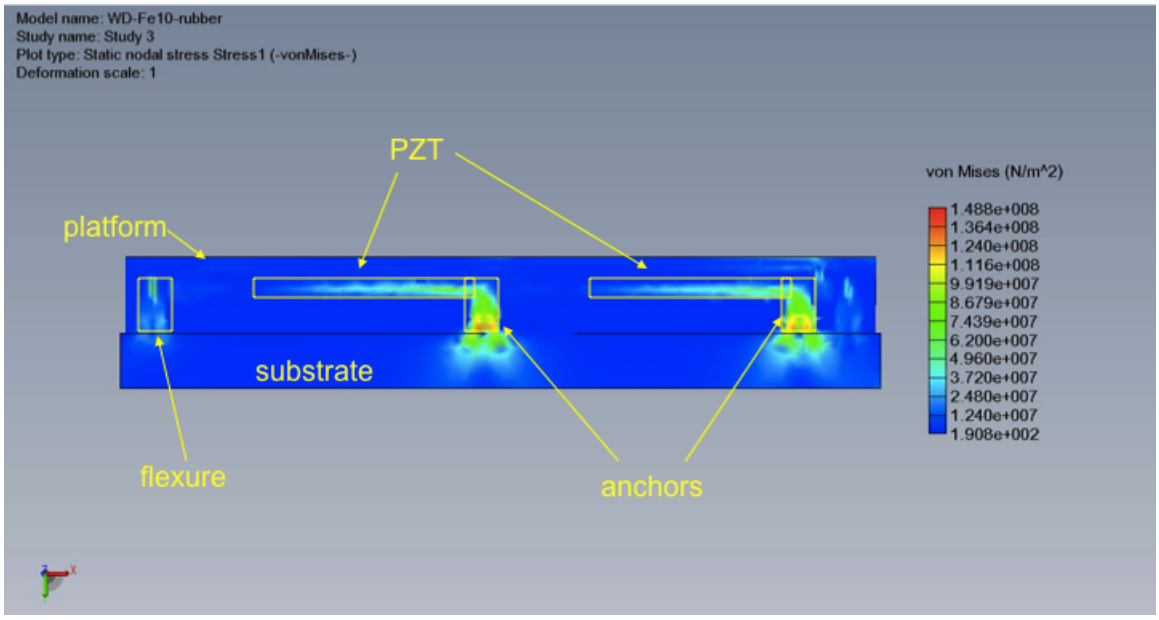

Figure 3.17: 3D finite element model of transverse piezoelectric actuator shows that natural rubber is sufficiently compliant to allow for actuation

The bulk modulus was increased until the von Mises stress in the elastomeric fill came to within about 10% of the stress in the PZT. At this point, with a Young's modulus of about 10 MPa, the displacement drops rapidly. Several materials were found which meet this criteria and which can be deposited with standard microfabrication techniques. As an example, one good candidate is SYLGARD 184 silicone rubber because it has a modulus of 0.37 to 0.89 MPa, depending on composition, and can adhere to an alumina substrate with DOW CORNING HV PRIMER 10 and can be UV cured. It also is stable at temperatures beyond 300°C. The drawback of this material, however, is outgassing at standard temperature and pressure. This was, in fact, the major limiting factor with all of the materials considered. Unfortunately, outgassing causes significant reliability problems at the head-disk interface and associated materials are usually put on the disallowed materials list. Because of stringent restrictions on outgassing in HDD's and the unavailability of sufficiently compliant non-outgassing materials, it was determined that the elastomeric fill concept is infeasible at this time.

3.5.2 Fabricating a Shear Wall on the ABS

The second solution considered was to fabricate an alumina wall in such a way that the ABS is completely closed, as illustrated in Fig. 3.18. Although this solution seems quite counterintuitive, as the direction of actuation is along the stiffest direction of the wall, it can be shown that for a very thin wall with high actuation force, sufficient actuation can be obtained.

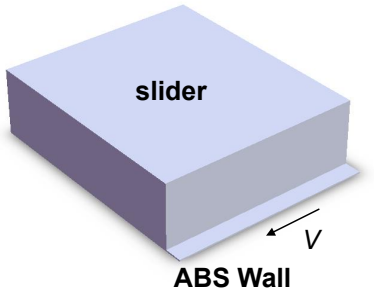

Figure 3.18: Illustration of shear wall concept

The displacement of the shear wall in the shear direction is given by [63]:

$$\Delta = \frac{6VL}{GA} \tag{3.49}$$

where L is the height of the wall, G is the shear modulus of alumina (150 GPa), and the cross-section area, $A = wt$, the width times the thickness. Rearranging Eq. (3.49) yields the wall stiffness,

$$k = \frac{5GA}{6L} \tag{3.50}$$

As an example, a shear wall which is 5 μm thick, 700 μm wide, and 60 μm tall, the shear stiffness will be 6,800 kN/m. This is over an order of magnitude higher than the stiffness of the flexures for electrostatic actuators or even the stiffness of the piezoelectric elements. Consequently, these dimensions would not be feasible. If the ABS wall is instead made 100 nm thick the shear stiffness will be 136 kN/m, just slightly less than the stiffness of the piezoelectric quasi shear mode actuator. A three-dimensional finite element model of the quasi shear mode actuator with a shear wall is shown in Fig. 3.19. As one might expect, the displacement of the actuator is reduced from 1.8 nm/V to about 1.0 nm/V at the trailing edge. Recall that this device can be multi-stacked to increase the gain to 20 nm/V as desired.

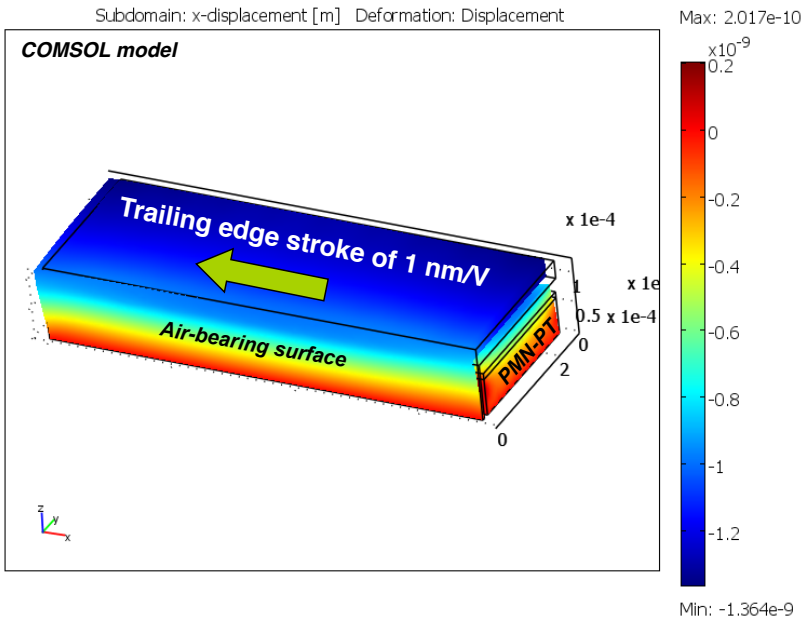

Figure 3.19: 3D finite element model showing that the quasi shear mode actuator has sufficient force to deform a thin ABS shear wall

Fabricating such a 100 nm thick shear wall during the head fabrication process proves to be quite difficult. Furthermore, the shear stresses at full stroke will be as high as 70 MPa. While the tensile strength of alumina is 300 MPa, one of the concerns is that non-uniformity in the thin film will causes stress concentrations in some regions and cause crack nucleation there. Also, the finite element solution reveals another disadvantage arising from the use of a shear wall. It produces a rotation of the head about the out-of-plane axis, potentially causing the edges to crash into the disk at full stroke. Fortunately, the edges of the slider are generally rounded during ABS patterning such that such rotations will not cause a crash. Also, the rest of the ABS usually flies several microns from the disk surface and only near the read/write elements is slider this close to the disk.

Overall, it appears that a shear wall remains a potential solution to the ABS gap problem for the quasi shear mode actuator. For electrostatic actuators, on the other hand, it requires too much force and it also does not protect them from particle contamination and resulting catastrophic failure. It also requires too much force for transverse piezoelectric actuators.

3.5.3 Leaving a Controlled Nano-Gap

Another potential solution to the ABS gap problem is to leave a controlled nano-gap which will allow the head to move freely over very small distances without opening up the gap sufficiently to disturb the underlying airflow or lubricant movement. According to computational fluid dynamic simulations, the peak

pressure at the read/write pole tip drops from approximately 20 atm to less than 2 atm across the slider by 100 μm upstream from the trailing edge [64]. This means that the ideal location to introduce an ABS gap is upstream from the trailing edge, as shown in Fig. 3.20. The pressure loss at this location will be much less than if the gap were located closer to the pole tip. Also, the gap should be smaller than the boundary layer at the bottom of the ABS, approximately 1 nm or less. If this is the case, flow through the gap will be negligible. Determination of the exact pressure loss, however, will require more intensive study.

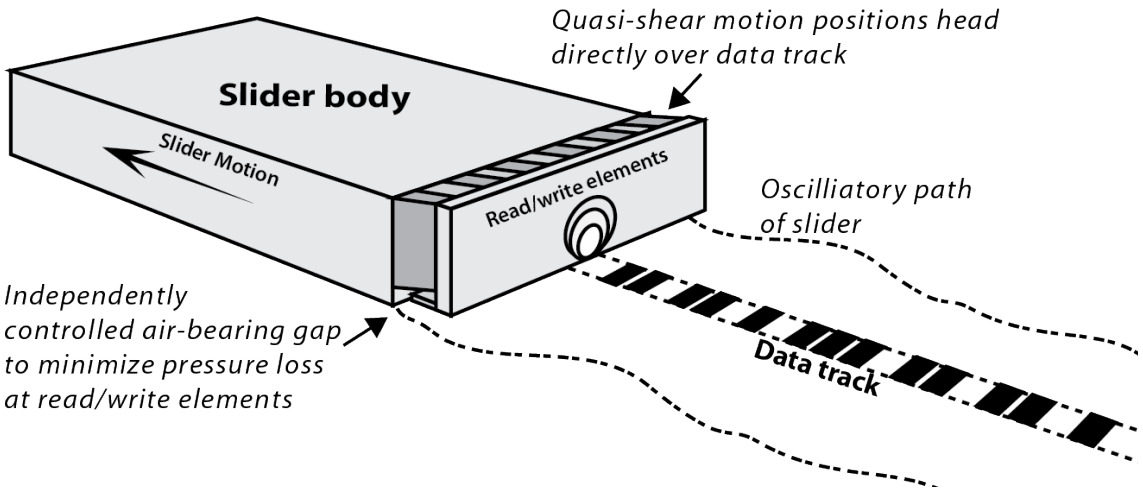

Figure 3.20: Illustration of piezoelectric quasi shear mode actuator with a controlled nano-gap

Clearly, the piezoelectric quasi shear mode actuator as shown in Fig. 3.20 is the most ideal actuator for achieving this controlled ABS gap out of all the actuators discussed thus far. This is because it inherently acts as a two-degree-of-freedom actuator where the two actuation modes can be achieved with the same three interconnects. The off-track mode is controlled by setting the voltage difference between top electrodes of opposing pillars while the ABS gap is controlled by setting the mean of the top electrodes with respect to the ground electrode.

Chapter 4

Prototype Fabrication and Testing

In chapter 4, a prototype fabrication process is developed for the novel piezoelectric quasi-shear mode actuator. Various methods for depositing piezoelectric material are investigated. Also, newly developed methods for planarizing PMN-PT and electroplated copper are presented along with techniques for fabricating high aspect-ratio sidewalls in PMN-PT. The completed prototype is shown and frequency response testing is presented for this completed prototype.

4.1 Simplified Design for Prototyping

The piezoelectric quasi-shear mode actuator was selected for further investigation due to its potential for high bandwidth actuation and high force for either closing the ABS gap with a shear wall or leaving an independently controlled sub-nanometer gap. Several simplifications had to be made in order to fabricate the first prototype. First, it would be unnecessarily difficult to fabricate the entire read and write head on top of the prototype and this would have required an infeasible level of collaboration with industry. Therefore, the prototype was designed to have a very large reflective surface on the head in order to measure actuation velocity with a laser doppler vibrometer (LDV). This also allows the measurement of actuation for ABS gap control as well as fly-height deviation on the other two surfaces.

Secondly, rather than fabricating the entire device at one time, it was divided into two components as shown in Fig. 4.1. Component A consists of the piezoelectric pillars with a ground electrode and top electrodes. Component B consists of the hinge geometry and a large head for measurement purposes. The two components are bonded with an epoxy bond with sufficient space left on top of each pillar for wire bonding to individual electrodes.

Finally, a single bulk material was used for the piezoelectric because fabricating piezoelectric multi-stack pillars would have required too much development time. Nevertheless, to increase the gain and make the system easier to characterize, the electrostrictive material lead magnesium niobate lead titanate was used. Bulk large crystal 0.67PMN-0.33PT grown by the Bridgman method and poled in either the <110> or the <001> direction has been reported to have a piezoelectric constant, d_{33}, in excess of 1800 pC/N [65] [66], which is equivalent to a stack of three or four layers of bulk PZT.

By dividing the device into two components, both components of the process flow could be developed simultaneously. Each individual component process flow will be

discussed along with the fabrication methods which were investigated but not included in the final prototype fabrication.

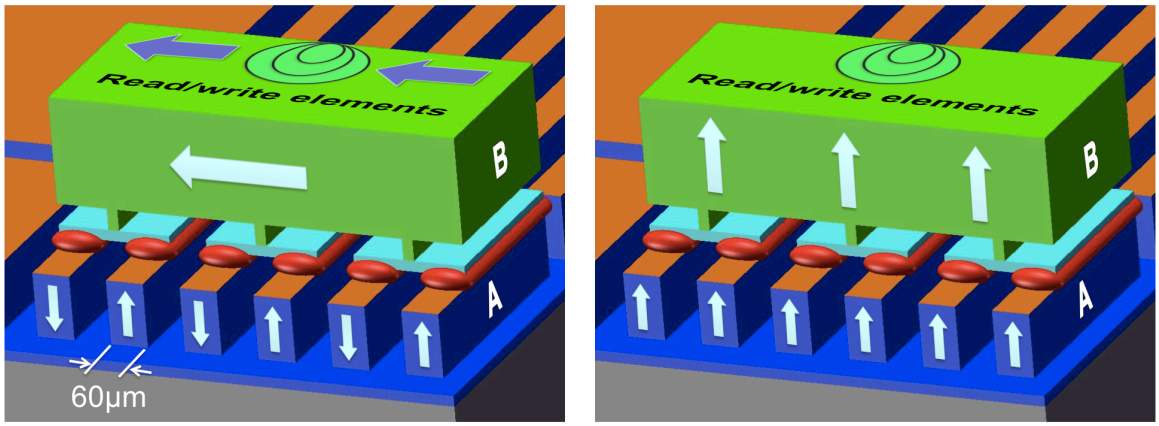

(a) (b)

Figure 4.1: The prototype quasi shear mode actuator is designed for actuation in either (a) the shear direction or (b) the gap control direction. The read/write elements are shown for illustrative purposes only. They are not part of the prototype fabrication process.

4.2 Bottom Component Fabrication

As shown in Fig. 4.1, the bottom component was designed to have 60 μm wide pillars of piezoelectric material bonded onto a silicon handle wafer. This configuration is unusual for several reasons. Firstly, it requires the deposition of a very thick film of piezoelectric material on a material with a significant thermal expansion mismatch. Secondly, the top electrodes must be smooth enough for a wire-bond connection for testing. Lastly, it requires structures which are taller than they are wide with highly vertical sidewalls.

4.2.1 Piezoelectric Material Deposition

The bottom of the piezoelectric material must be conductive, as shown in Fig. 4.2, meaning that the bond must be a conductive bond. Four methods of achieving this material configuration were investigated:

1. Deposit thin PZT layer by sol-gel method
2. Deposit bulk PZT by thermo-compression bonding
3. Deposit bulk PMN-PT by eutectic bonding
4. Deposit bulk PMN-PT with a conductive epoxy bond

4.2.1.1 Sol-Gel Method for PZT Deposition

The first deposition method investigated was the sol-gel method because it is the most easily transferred to large-scale manufacturing. Experiments were conducted with PZT Sol-Gel E-series solution purchased from Mitsubishi Materials Corporation along with a 1 wt. % solution of PT to be used as the seed layer. The coating process was then followed as specified by the manufacturer [67].

First, the Pt electrode layers were sputtered with a Ti adhesion layer onto Si test wafers. These wafers were then cleaned in O_2 plasma at 50 W for 2 minutes and then in an ultra-sonic bath with acetone followed by an IPA rinse and an N_2 dry. Next, 2 mL of PT seed was dispensed on an automated spinner at 500 RPM, followed by a 15 second ramp to 3000 RPM and hold for 30 seconds. The wafer was immediately pyrolized on a hotplate at 400°C for 1 minute. The wafer was cooled on a cooling block to room temperature.

Then, 6 mL of PZT Sol-Gel E-series was filtered and dispensed at 500 RPM with a 5 second ramp up to 2750 RPM followed by a 5 second ramp to 3000 RPM and a 20 second hold. The newly deposited layer was dried on a hotplate at 200°C for 5 minutes and then baked at 400°C to undergo pyrolysis and placed back on the 200°C hotplate for 2 minutes to minimize film stress during cooling. Finally, the PZT film was annealed in a rapid thermal anneal at 700°C in O_2 at 50-60 sccm. Note that the uniform cyan coloring of the film as seen in Fig. 4.2 indicates a high level of film thickness uniformity. For thicker layers, the PZT Sol-Gel E-series deposition process was repeated several times as summarized in table 4.1.

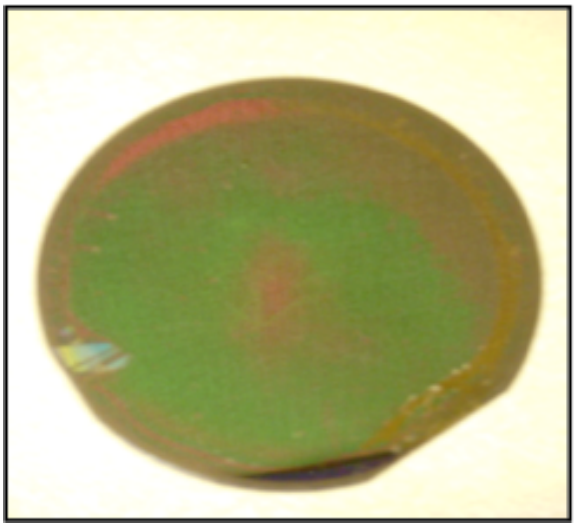

Figure 4.2: PZT Deposited by sol-gel method

Table 4.1. Maximum sol-gel film thickness experiments at 3000 RPM and 1000 RPM

	Single Film	Multiple	Multiple	Single Film	Multiple	Multiple
Peak Spin Speak	3000 RPM	3000 RPM	3000 RPM	1000 RPM	1000 RPM	1000 RPM
Num. Layers	1	7	8	1	2	3
Total thickness	0.1 um	0.5 um	delamination	0.2 um	0.4 um	delamination

As table 4.1 reveals, the maximum thickness of PZT sol-gel before delamination is far too small for the requirements of the prototype actuator. Although much thicker PZT films, up to 60 μm thick, have been demonstrated by dip coating [68], these processes are still not yet commercially available and are not directly applicable to the goals of this project. Therefore, the sol-gel deposition method was left as a process for further investigation during the productization stage.

4.2.1.2 Thermo-Compression Bonding with PZT

Preliminary experiments with bonding bulk unpoled PZT to AlTiC substrates were conducted. It was found that 1 cm chips with 1um of Au could be bonded with a bonding force of 20 kg over 20 minutes to the much larger AlTiC substrate, as shown in Fig. 4.3. The bond strength was found to be greater than the tensile strength of the PZT. Although this size of PZT chip is much too small for large-scale manufacturing, it is sufficient for the 1x1 mm footprint of the prototype device and, therefore, bulk PZT remains a feasible option for prototyping. In the end, however, PMN-PT was selected as the piezoelectric material for implementation due to its high d_{33} constant.

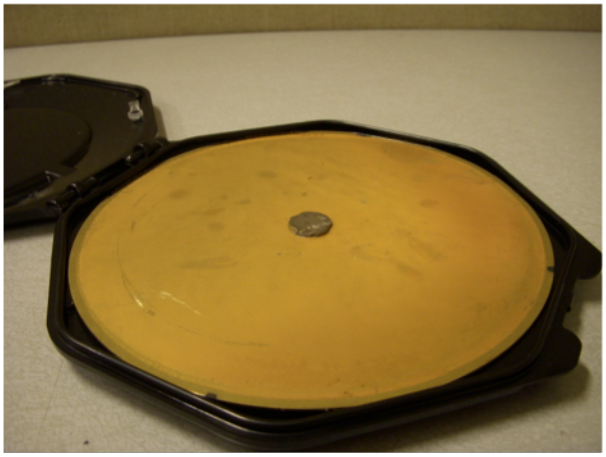

Figure 4.3: Thermo-compression bond of PZT with AlTiC substrate

4.2.1.3 Thermo-Compression Bonding with PMN-PT

Bulk large-crystal PMN-PT chips of dimension 10x10x0.5mm were obtained from Sinoceramics in the [001] orientation. The piezoelectric constant was measured to be approximately 1900 pC/N. The standard Au electrodes which were included with these chips were then removed in Transene TFA Gold Etchant and the adhesion layer was removed with a standard Chrome Mask Etchant, CR-14. Then, a 20 nm Cr adhesion layer was sputtered to the PMN-PT chips to obtain a stronger adhesion layer and 1 μm of Au was evaporated on top.

Thermo-compression bonding experiments were then carried out using a Karl-Suss FC 150 flipchip bonder, capable of up to 40 kg of bond force and 400°C bonding temperature with sub-micron alignment accuracy and laser alignment. Even with this 4 GPa of bonding pressure, however, reliable bonds did not form over the surface of the chip because the roughness was still too high. The measured surface roughness was R_q=*354* nm, which is 100 times higher than what is reported for reliable PZT to Si wafer bonding, about R_q=*3.4* nm [69].

Other experiments were performed with smaller Au thicknesses and decreased temperatures of 350°C to match the parameters for silicon thermo-compression bonding in literature [70]. Also, one set of wafers was prepared for Cu/Cu bonding at 400°C; however, the film stress was too high at this temperature and the films delaminated. Overall, the results, shown in table 4.2, all pointed to the need for decreased surface roughness, which will be discussed in section 4.2.2; however, even with the decreased surface roughness, a reliable thermo-compression bond was not formed. It is thought that this can be attributed to the bowing resulting from the polishing process acting more heavily on the chip edges than in the center.

Table 4.2. Parameters and results of thermo-compression experiments with PMN-PT chips and silicon handle wafer

	Test 1	**Test 2**	**Test 3**	**Test 4**
Substrate Surface	150 nm Au	150 nm Au	400 nm Au	300 nm Cu
Chip Surface	200 nm Au	200 nm Au	1 um Au	300 nm Cu
Bonding Temperature	350 °C	350 °C	400 °C	400 °C
Bond Force	25 kg	40 kg	40 kg	40 kg
Bond Time	20 min	20 min	20 min	20 min
Pre-Bond Cleaning	IPA	O_2, IPA	IPA	IPA
Autocollimation	No	Yes	Yes	Yes
Result	Au/Substrate interface failed	Partial adhesion, failed in U/S cleaning process	No adhesion	Cu delamination

4.2.1.4 Eutectic Bonding with PMN-PT

Eutectic bonding is a very attractive work-around for large surface roughness because a liquid is formed which can fill in the gaps and created a uniform bond across the substrate. Provided the roughness is low enough to allow enough Au to diffuse into the Si sufficiently, a Au-Si eutectic mixture will tend to nucleate. The aforementioned PMN-PT chips were sputtered with a 20 nm Cr adhesion layer and an additional 1 μm of Au was evaporated.

The chips were bonded to a Si handle wafer at 400°C with the Karl-Suss FC150 but, in the first experiment, no eutectic formation occurred. This was because the native oxide acted as a diffusion barrier for the Au. In the second experiment, this native oxide was removed in 5:1 buffered hydrofluoric acid (BHF) and a eutectic solution was observed. But even though a eutectic solution was formed, the chips did not adhere to the silicon handle wafer, as summarized by the experiments in table 4.3. While the eutectic solution was indeed formed, it did not wet the PMN-PT surface but only remained as droplets on the Si surface. This phenomenon is seen from the cross-sectional SEM in Fig. 4.4, where the Au has completely been removed from the PMN-PT surface. This suggests that the PMN-PT is still too rough in that the roughness is not allowing the eutectic mixture to wet the PMN-PT surface. To reduce the surface energy, a process was developed for chemical mechanical planarization (CMP) of PMN-PT as presented in section 4.2.2.

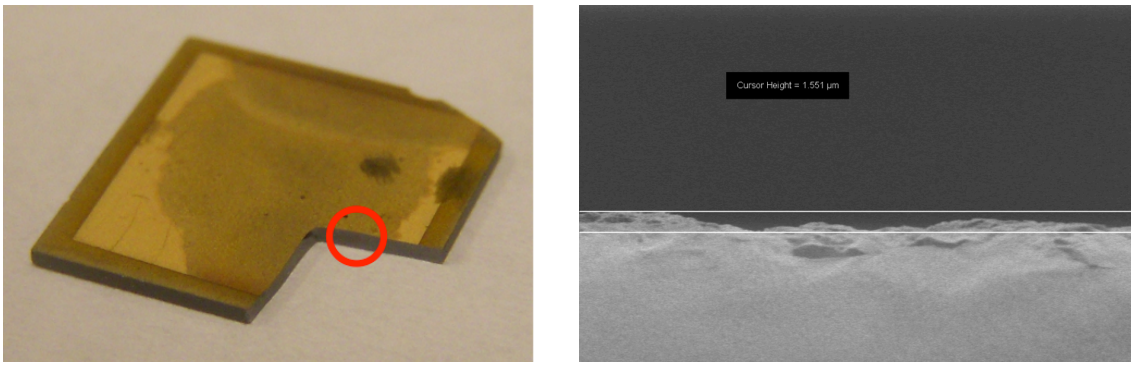

(a) **(b)**

Figure 4.4: (a) Photograph of PMN-PT chip after eutectic bonding and (b) SEM image of cross-section at the location indicated by the circle

Table 4.3. Parameters and results of Au-Si eutectic bonding experiments performed with chemically-mechanically polished PMN-PT and a silicon handle wafer

	Test 1	Test 2	Test 3	Test 4	Test 5
Substrate Surface	Native oxide	Si	Si	Si	Si
Chip Surface	200 nm Au	200 nm Au	1 um Au	1 um Au	150 nm Au
Bonding Temperature	400 °C	400 °C	400 °C	380 °C	380 °C
Bond Force	40 kg	40 kg	40 kg	40 kg	40 kg
Bond Time	20 min	20 min.	20 min	10 min	10 min
Pre-Bond Cleaning	IPA	5:1 BHF	5:1 BHF	5:1 BHF	5:1 BHF
Autocollimation	Yes	Yes	Yes	Yes	Yes
Result	No adhesion	No adhesion	No adhesion	No adhesion	No adhesion

After the CMP was optimized to reduce the roughness from R_q=*354* nm down to R_q=*19.4* nm, a reliable eutectic bond was consistently formed over three trials using the parameters in table 4.4 with bond areas of 9%, 12% and 18%. Although this is not sufficient for production, it provides more than enough bond area for prototyping.

Table 4.4. Final eutectic bond parameters (after CMP)

Substrate Surface	Si/Cr/1um Au
Chip Surface	1 um Au
Bonding Temperature	350 °C
Bond Force	40 kg
Bond Time	40 min
Pre-Bond Cleaning	5:1 BHF
Autocollimation	Yes
Result	Strong adhesion over 18% of chip

Fig. 4.5 shows and SEM images of the resulting uniform bond interface between Si and PMN-PT. Note that the Si-Au eutectic mixture now wets the entire surface of the PMN-PT, as made more evident by the close-up SEM image in Fig. 4.6.

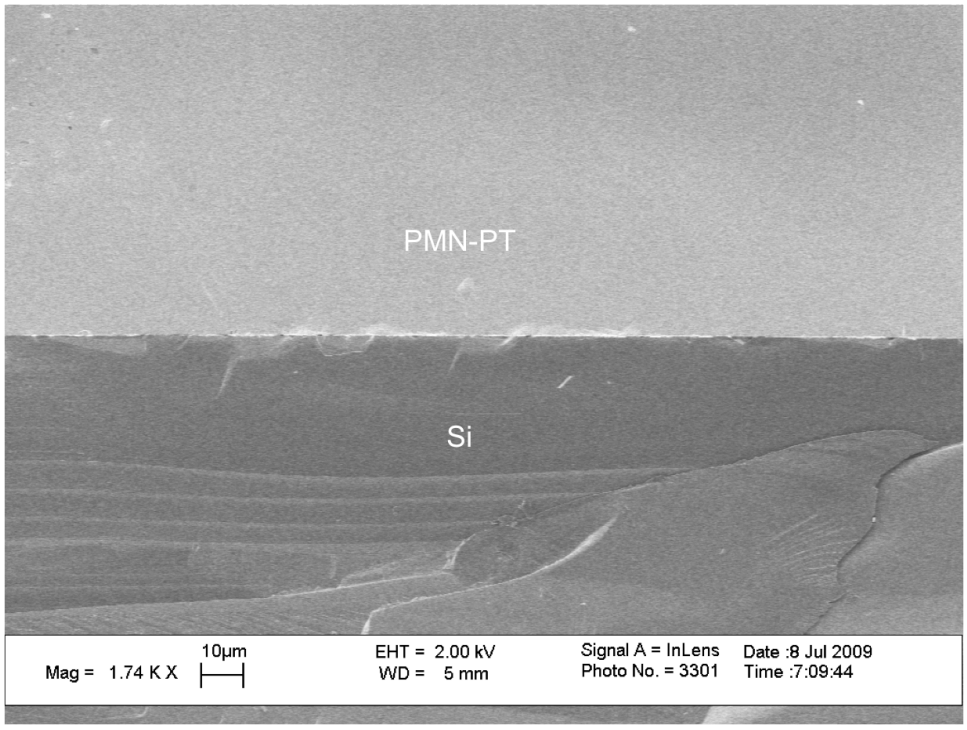

Figure 4.5: SEM image of Si/PMN-PT interface shows that a uniform Au-Si eutectic bond has formed across the interface

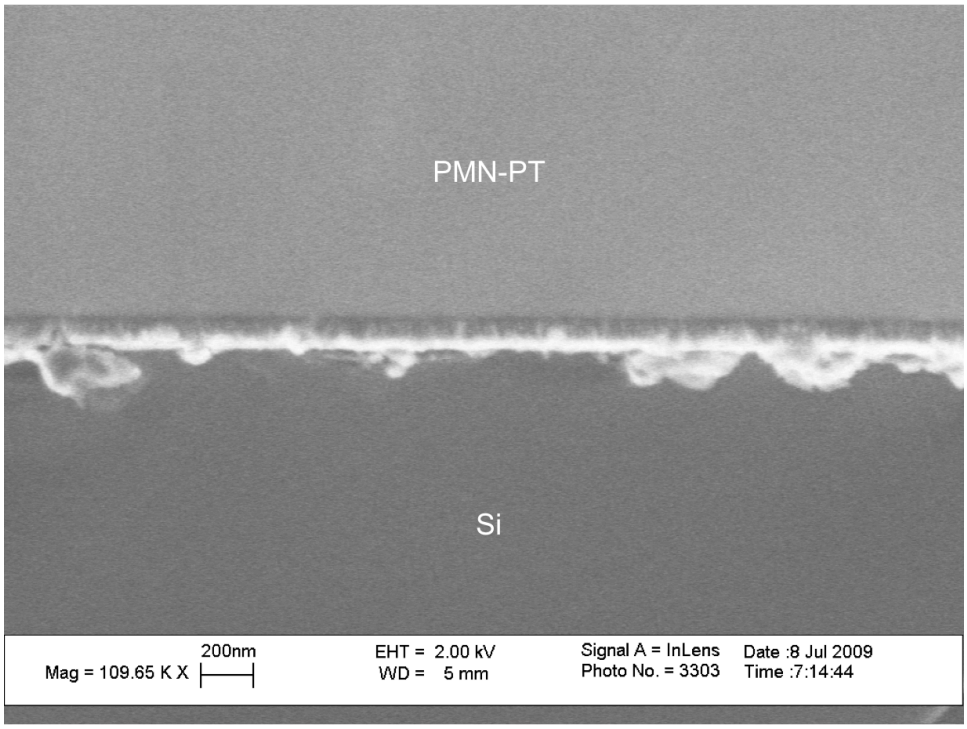

Figure 4.6: Close-up SEM image of Si/PMN-PT interface shows that the Au has diffused into Si but not into PMN-PT

4.2.1.5 Conductive Epoxy Bond with PMN-PT

The final bonding method considered for use in the prototype was an epoxy bond, as has been previously demonstrated for use with PZT [71]. The key benefit of using an epoxy bond is that the surface does not need to be polished. In fact, the conductive epoxy bond was successful from the very first attempt. Unfortunately, it can only be used for prototyping and not in production because of its temperature instability and outgassing properties.

4.2.2 Chemical Mechanical Polishing of PMN-PT

Chemical Mechanical Polishing has already been demonstrated for PZT thin films using silica-based slurry to achieve a roughness as low as R_q*=32* nm [72]. Given that the mechanical and chemical properties of PMN-PT are very similar, it was reasoned that a silica slurry would also be effective for PMN-PT. A premixed silica slurry, D7000, was purchased from Cabot Microelectronics which consists of DI water, KOH, and 200 nm silica particles. This slurry was dispensed onto the pad at a flowrate of 300mL/min. The table speed and head speed were varied as were the downforce and polishing time. Since the PMN-PT chips measure only 1cm x 1cm and most CMP tools are built for either 4" or 6" wafers, these chips must be mounted in a dummy wafer as shown in Fig. 4.7. The PMN-PT chips are held in the dummy wafer by a water bond to the soft tech-cloth cushion (white) in the center of the dummy wafer.

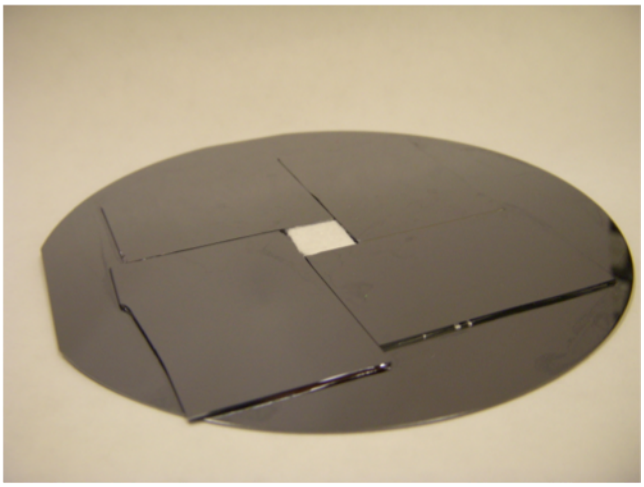

Figure 4.7: Dummy wafer used for CMP of PMN-PT

In order to reduce cracking in the PMN-PT chips, the downforce had to be reduced to the minimum value of 300 gf/cm^2. Likewise, the table speed could not be any higher that 50 RPM with a head speed of 50 RPM or cracking would occur. The primary parameter left to tune was the CMP time. Surprisingly, as table 4.5 shows,

the roughness actually increases with time. This may be explained by the fact that polishing occurs at a very fast material removal rate because the area of the chip is very small compared to a 4" wafer while the downforce is set to a value which is generally used for a 4" wafer. Therefore, with such a high material removal rate, the initial polishing creates a very smooth and shiny surface but subsequent surface damage causes non-uniform material removal again and the chip becomes more and more rough and, as was visually observed, increasingly dull. Fig. 4.8 shows an SEM image of the PMN-PT material before and after the 2 minute CMP process.

Table 4.5 Table comparing CMP time versus roughness

	2 Minutes	4 Minutes	6 Minutes
R_a without Au	76.8 nm	159 nm	179 nm
R_q without Au	101 nm	199 nm	220 nm
R_a with Au	14.7 nm	25.3 nm	35.6 nm
R_q with Au	19.4 nm	32.5 nm	45.7 nm
Bond Area (%)	18%	9%	12 %

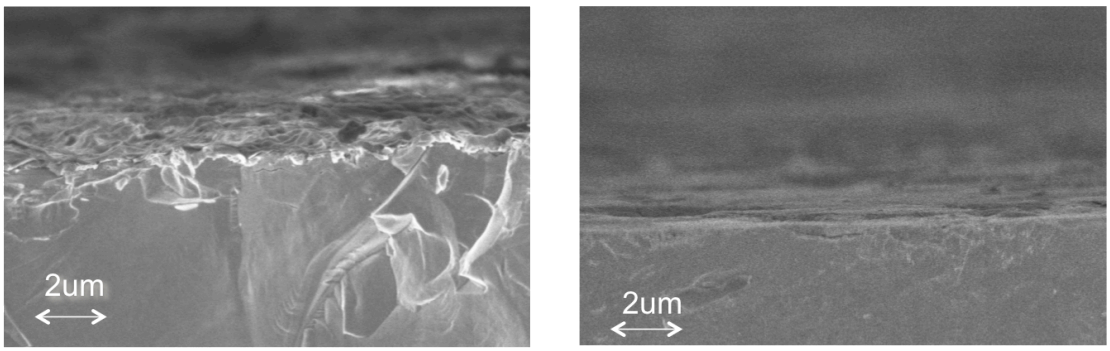

Figure 4.8: SEM image of PMN-PT (a) prior to CMP and (b) after 2 minute CMP

4.2.3 Scribing of PMN-PT

Once the PMN-PT has been bonded to the handle wafer, the pillar geometry must be defined with a very high aspect ratio of 250:70 as shown in table 3.4. High aspect ratios of 5:1 have been demonstrated for PZT using 2000W inductively coupled plasmas with SF_6 and Ar gas [73] [74]. These processes, however, require a special MEMS clean chamber in which Pb is allowed. At the Berkeley Nanofabrication Laboratory, there are very tight restrictions on what can be etched in the STS Advanced Silicon Etch systems and the Centura Deep Silicon Etch system [75]. Since these are the only systems with inductively coupled plasmas with high enough

power for such a high aspect ratio etch, such a process would need to be conducted elsewhere. For this reason, wafer scribing was considered as a prototyping alternative because of the reported high aspect ratios of PZT with ultra-thin dicing blades [76]. A similar process was developed for the wafersaw at the Berkeley Nanofabrication Laboratory with an ultra-thin dicing blade purchased from Asahi Blades, H405JS-T4-030080, which has a grit size of 2-4 μm, a 35 μm kerf, and a blade exposure depth of 800 μm. The blade was used at a feedrate of 1 mm/s and a cutting depth of 250 μm to obtain the structures shown in Fig. 4.9 below.

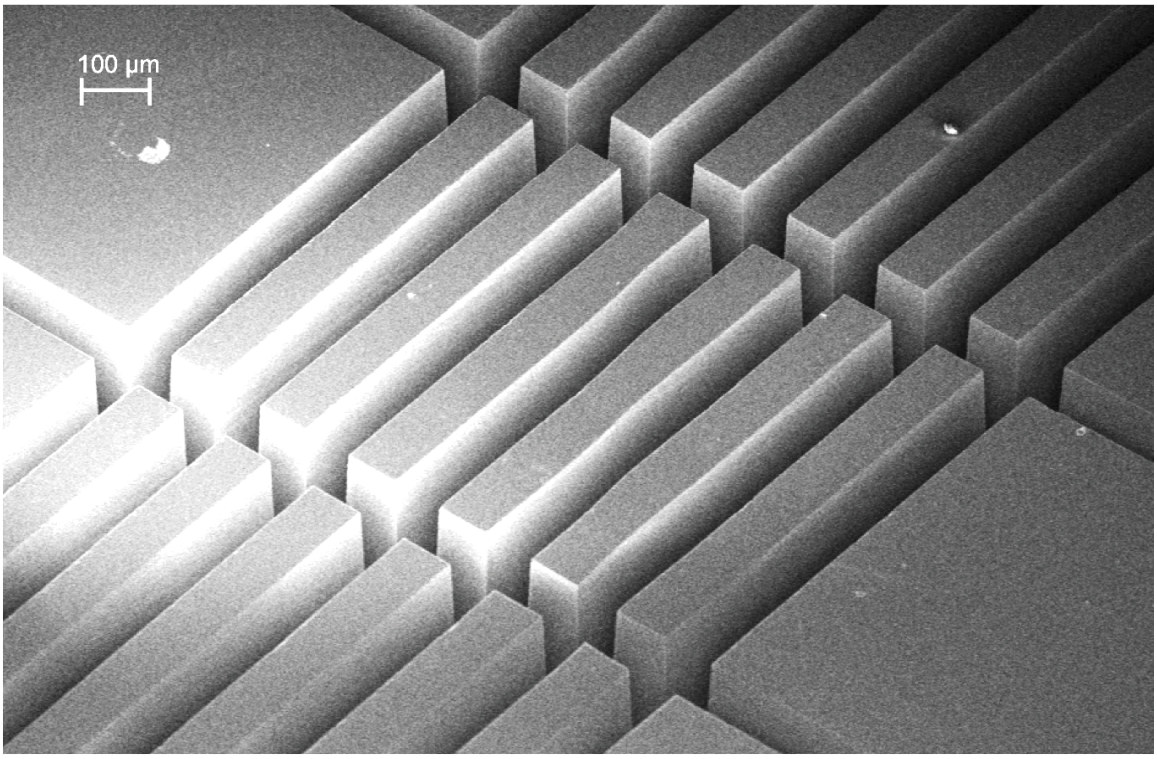

Figure 4.9: SEM image of completed PMN-PT structures patterned by wafer scribing

4.3 Top Component Fabrication

The top component of the prototype was fabricated on a 6" silicon handle wafer according to the process flow depicted in Fig. 4.10. Each device was fabricated within a 1.2mm x 1.2mm footprint to leave room for a 200 μm dicing kerf. The final block shown as Fig. 4.10(j) is therefore 1mm x 1mm x 0.5mm, where the LDV beam is just under 0.5mm in diameter.

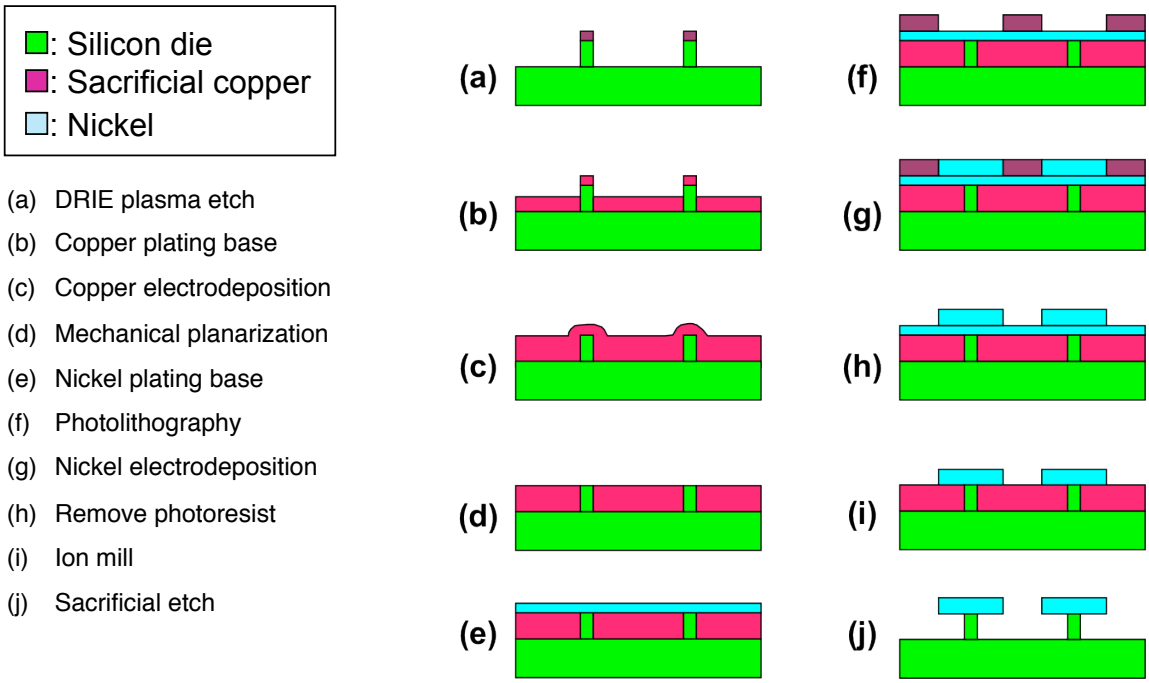

Figure 4.10: Top Component Fabrication Process

The first step in the top component fabrication process is to pattern 8x4 μm pillars with 0.3 μm OiR 10i photoresist which has been hard-baked for 120 seconds at 120°C. This was used for an 8 μm deep reactive ion etch with a 4 second etch cycle followed by a 6 second passivation cycle and repeated at 600 W of inductively coupled plasma and 14 W on the platen. Because of the high ratio of bare silicon to patterned surface, the etching load was much higher than normal and, thus, the bull's-eye effect became very pronounced and devices in the center of the wafer were unusable because of the buildup up scum from the etch byproducts in this region.

After deep reactive ion etching, the photoresist was removed in a bath of PRS-3000 at 80°C followed by an acetone and IPA clean and an N_2 dry. The wafers were then sputtered with an adhesion layer of Ti at 100 W RF for 10 minutes and a plating base of Cu at 300 W DC for 10 minutes. Each wafer was diced into 2.5cm x 2.5cm squares for electroplating sacrificial copper and cleaned once again in an ultra-sonic acetone bath and IPA clean and an N_2 dry. Immediately after this cleaning step, the chips were placed in a premixed copper sulfate bath purchased from Technic Inc., Techni Copper FB Bath RTU, with 10 mL of brightener added for every Amp-hour of plating. Solid Cu plating anodes were purchased from Otto Frei such that a new anode could be used for each plating run. The plating current was recorded on a computer and is shown in Fig. 4.11. Note the plating current gradually converges as the Cu anode is eroded to create a solution flux equilibrium for the applied potential of 16 mV. After an hour of plating, the plating height was measured on a profilometer to be 1.9 μm.

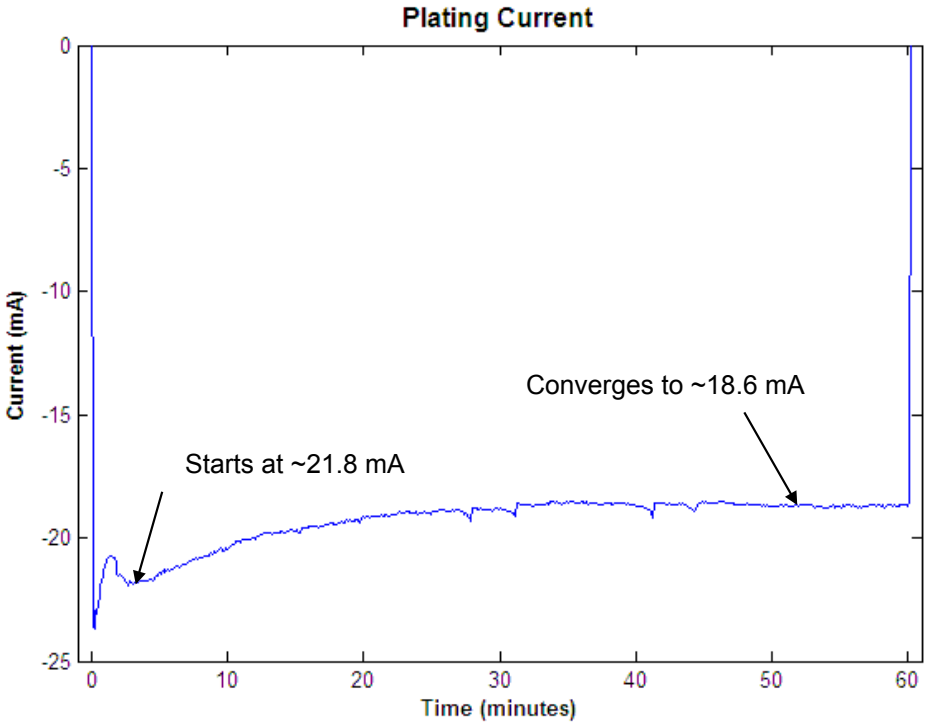

Figure 4.11: Plating current for Cu FB Bath RTU converges, over time to a constant value once solution reaches equilibrium for the driving potential

With the data obtained in Fig. 4.11, the plating coefficient can be estimated based on the following equation:

$$k_{Cu} = \frac{\Delta h}{(AF)(A)\sum_{t=0}^{t_f} i(t)\Delta t} \tag{4.1}$$

where AF is the fraction of area exposed, which is approximately 1, A is the area of the chip, 2.5x2.5 cm^2, $i(t)\Delta t$ comes from the plating current data above, and Δh is the 1.9 μm plating thickness. Based on this data, the plating coefficient was estimated to be -44x10^{-6} $A^{-1}s^{-1}m^{-1}$ for this bath. This coefficient was used for subsequent chips to estimate the time necessary for plating the full sacrificial layer up to a thickness of 13 μm as depicted in Fig. 4.10(c).

After electroplating the Cu sacrificial layer, the top surface needed to be planarized to reveal the Si posts and prepare it for electroforming the Ni beams. Because this needed to be done at the chip level rather than across a wafer, electrochemical CMP would be very difficult. Therefore, planarization was done with Dicro SCR polishing compound on a cotton wheel mounted to a dremel tool and operated at 10,000 RPM. The surface was polished until the Si posts were revealed as shown in Fig. 4.12. The polishing particles, seen in Fig. 4.12, were then removed with detergent and water in an ultra-sonic acetone bath.

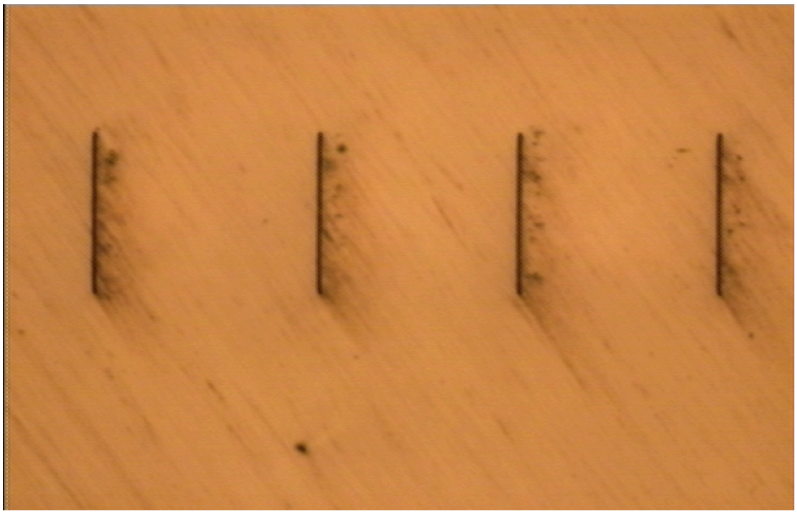

Figure 4.12: Polished Cu surface with Si posts revealed

After the ultra-sonic bath, the moisture was removed with an N_2 dry and 100°C hotplate bake. Then a 300 nm Cr/Ni plating based was sputtered at 100 W DC and 250 W RF, respectively, as depicted in Fig. 4.10(e). The adhesion strength of this plating base was tested by applying kapton tape with mild pressure to a test corner and peeling the plating base off. While the plating base come off of the Cu very easily, it remained firmly attached to the Si pillars.

The Ni crossbeams depicted were electroplated as shown in Fig. 4.10(f)-(h). First, 10 μm thick Shipley SPR 220 was spun on and baked on a hotplate at 115°C, exposed for 30 seconds, and developed for 16 minutes until the electroforming pattern was fully defined. Next, the chips were placed in Technic Ni Bath plating solution held at 70°C with a pure Ni anode purchased from Otto Frei. These chips were electroplated for 30 minutes at 50 mA to achieve a thickness of 10 μm. Then, the Cr/Ni plating base removed by ion milling over 10 minute intervals for a total of 40 minutes. Also, Cool Grease was used between the chip and the chuck in order to reduce the temperature and avoid delamination.

The final step, depicted in Fig. 4.10(j), consisted of dicing the chips into smaller die pieces and then removing the sacrificial Cu in Cu APS 100. In this solution, Cu is reported to have an etch rate of 2500 nm/min while Ni and Si do not etch at all [77] [78]. An SEM of the final structure is shown in Fig. 4.13. Note that the Ni beam stiffness is high enough and the clearance between the structure and wafer is large enough such that stiction does not occur, as is often the case for many free-standing MEMS structures of this geometry.

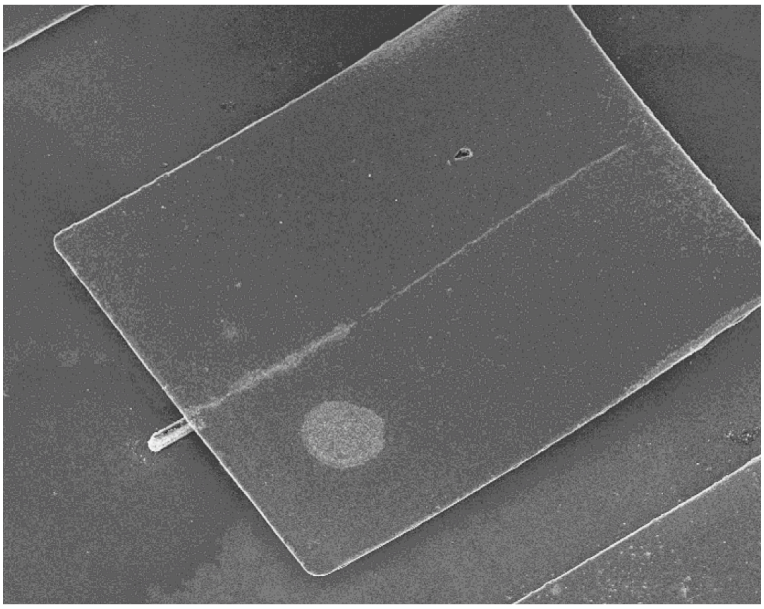

Figure 4.13: SEM of final hinge structure after Cu sacrificial release

4.4 Prototype Assembly

The completed top and bottom components were assembled with a flip-chip bonder using an epoxy bond. The device was then mounted on a printed circuit board and connected electrically by wire-bonding to the PMN-PT pillars. The details of this process will be discussed.

4.4.1 Flip-chip Bonding

The top and bottom components were bonded with an epoxy bond using High Strength 5-Ton Devcon Epoxy. This epoxy was selected because it has a high viscosity and a long setting time of about 30 minutes at room temperature. The high viscosity allows the epoxy to be dispensed as droplets directly onto individual Ni beams without wetting the entire surface of the top die. Fig. 4.14 shows how a low-viscosity epoxy droplet will begin to wet the rest of the surface. This is undesirable because it will block the rotation of the Ni beam structure during actuation. The setting time of 30 minutes allowed for mixing and depositing the epoxy followed by aligning the top and bottom die prior to bringing them into contact. Since the epoxy was more viscous, it had to be deposited by forming a needle into a loop shape to hold individual epoxy droplets and then transferring them to the die surface to be deposited by capillary action. The top and bottom were brought into contact and then backed off by 2 μm to allow the droplets to form a thick and solid bond between the PMN-PT pillars and Ni beams. This tight alignment and position control was obtained using a Karl Suss FC150 flipchip bonder.

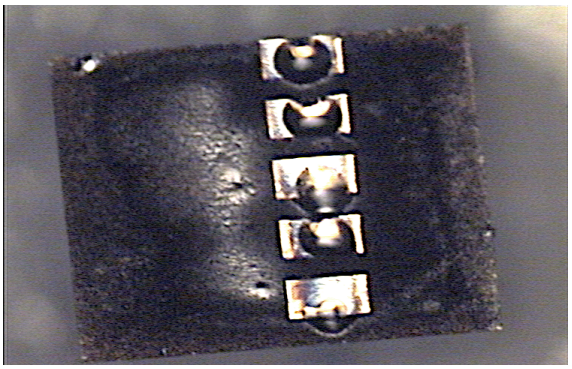

Figure 4.14: Low-viscosity epoxy droplets beginning to wet the rest of the die surface

4.4.2 Wire Bonding

After completing the flipchip bond, the entire device was mounted on a printed circuit board and gold wire-bonds were attached to the top of each PMN-PT pillar, as shown in Fig. 4.15.

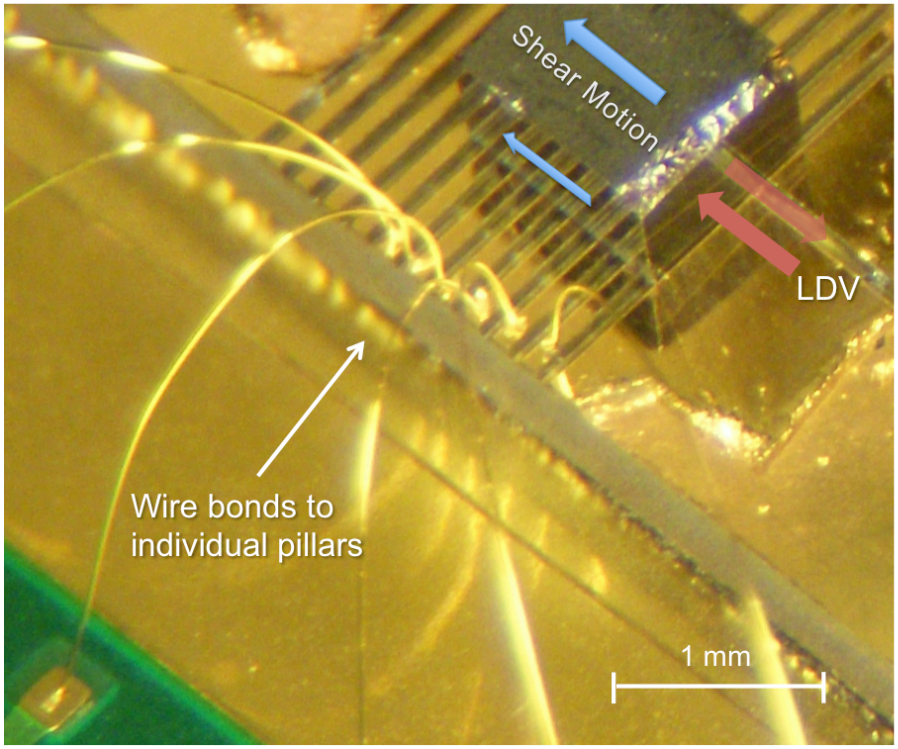

Figure 4.15: Completed device with gold wire-bonds from the printed circuit board. The direction of shear motion is indicated (blue arrows) and the location of LDV velocity measurement is also indicated (red arrows)

4.5 Testing and Characterization

Next, the completed prototype was tested and characterized by laser doppler vibrometry. Recall that the primary motion of interest is in the shear direction. In order to measure this motion, the LDV beam was placed in line with this direction and focused on the perpendicular face as depicted in Fig. 4.15.

4.5.1 Experimental Setup

In order to increase the d_{33} constant and linearize the actuation of the PMN-PT material, an offset voltage was introduced. Note that because it is an electrostrictor, unpoled PMN-PT has a d_{33} piezoelectric constant of approximately zero [79]. The material in this prototype, however, has been poled at a very high electric field to achieve $d_{33}=1900$ pm/V. There is, however, an inflection point reported in the *P-E* poling curve at zero field for 0.67PMN-0.33PT and, therefore, it is preferable to avoid crossing this point to avoid hysteretic effects. Such a DC bias voltage has also been shown to increase the d_{33} constant up to some maximum point for 0.9PMN-0.1PT [80]. Hence, it appears that it is quite advantageous to utilize a bias voltage to ensure that the driving field never cross zero.

Fig. 4.16 shows a schematic representation of the experimental setup used for testing the completed prototype. First, the base of the device is biased with a DC voltage of $V_b=18$ *VDC*. Then, the driving signal is generated by a dynamic frequency analyzer. Two operational amplifiers (op-amps) are used in the test circuit. The first op-amp is used to boost the 1.5 VAC driving signal to 15 VAC with $R_1=5k\Omega$ and $R_2=50k\Omega$. The second amplifier is used to invert the 15 VAC driving signal such that two sinusoidal signals are generated with a 180° phase offset between them. These signals are then connected to interconnects on the printed circuit board corresponding to the alternating pillars.

The frequency response of the device is then measured with an LDV set at a gain of 0.5 μm/V and focused on the side of the dummy read/write head as shown in Fig. 4.16. The reconstructed displacement signal is then fed back into the dynamic frequency analyzer to obtain frequency response data which is transferred to a computer for further analysis. Since the read/write head is only 500 μm tall and the laser beam is approximately 300-500 μm, depending on how well it is focused, a micro-positioning stage must be used to accurately position the prototype dummy head with respect to the LDV. Also, the position of the laser beam tends to drift with time. Hence, the position of the head must be checked and repositioned approximately once every 10 minutes. A very smooth and flat surface is required to reflect a reliable LDV beam and this beam must be focused back into the LDV objective lens by properly rotating the prototype head.

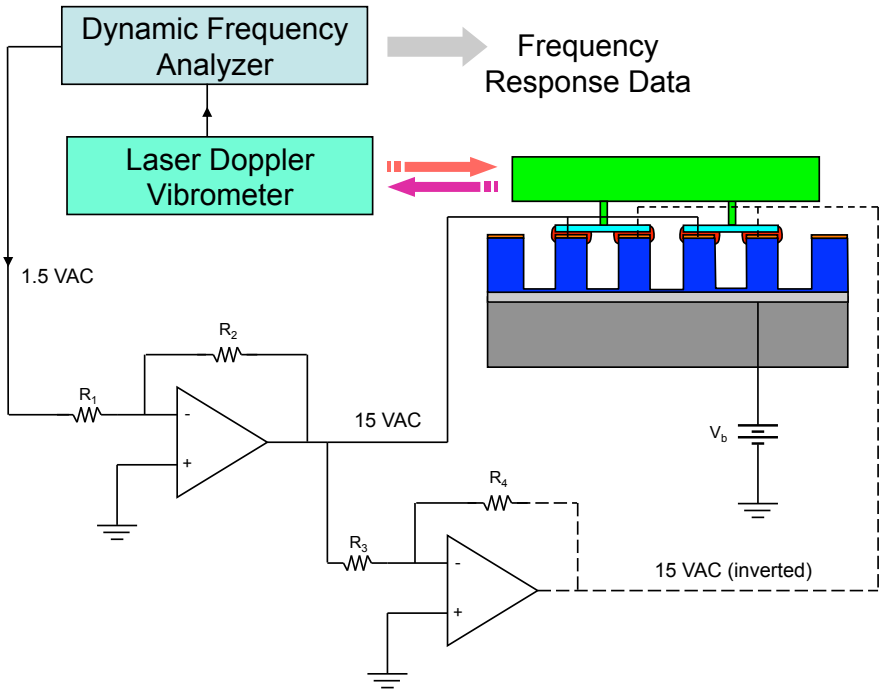

Figure 4.16: Experimental setup for piezoelectric quasi shear mode prototype testing

4.5.2 Frequency Response Measurements

In order to characterize the prototype performance, the actuation stroke was measured for frequencies over the entire range of the dynamic frequency analyzer and LDV setup. The dynamic frequency analyzer has an upper limit of 50 kHz and this was, therefore, the maximum frequency at which the actuator stroke was measured. Although the LDV can measure frequencies much higher than 50 kHz, it is limited in the low frequencies by static drift which increases roughly 20 dB/dec with decreasing voltage. Because the actuation signal is only 20dB above the noise floor already, below 5 kHz, this measurement noise overtakes the actuation signal and useful frequency response data is not obtained. Therefore, the working frequency response range for this setup is 5 to 50 kHz.

One of the confounding factors in measuring the actual stroke is that the dynamic frequency analyzer is matched to a nominal 50Ω impedance; however, the actual impedance of the test circuit is much higher and the actual device driving signal was measured to be only 6.8 VAC. For an LDV feedback gain of 500 nm/V and a frequency analyzer output of 1.5 VAC, this corresponds to a displacement of 110 nm/unit of gain from the output to the input of the dynamic frequency analyzer.

First, the shear motion was characterized by comparing measurements of the desired shear direction of motion with the undesired fly-height and out-of-plane deviation. This was done by actuating the pillars in the antiparallel configuration

and measuring with the LDV beam along the respective direction of motion, as shown in Fig. 4.17. Note that this configuration ensures that there is no Abbe offset and the measurement resolution will only be limited by electrical noise and LDV resolution, not by any mechanical distortion. The measured frequency response is plotted in Fig. 4.19.

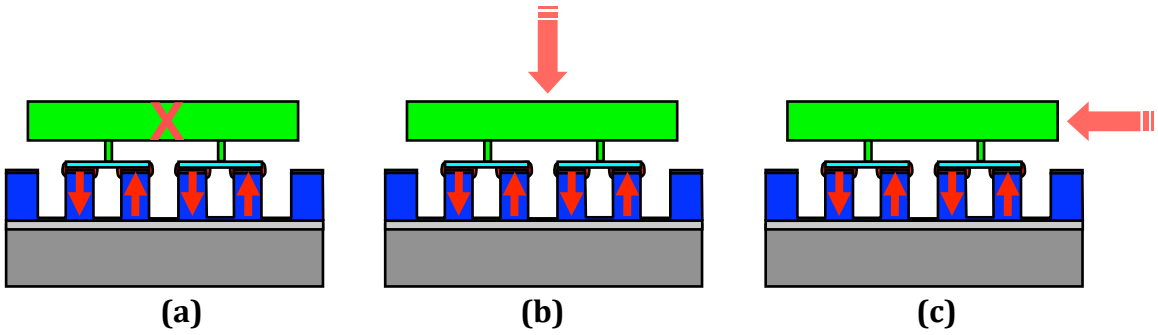

Figure 4.17: Measurement scheme for (a) Fly-height deviation (b) ABS Gap deviation and (c) shear mode motion

The set of measurements were intended to characterize the ABS gap performance and determine if the directionality of the device is sufficient. Measurements were taken from the top surface and pillars were actuated in the parallel (ABS gap direction) and antiparallel (shear mode direction) configurations, as shown in Fig. 4.18. The frequency response results are plotted in Fig. 4.20.

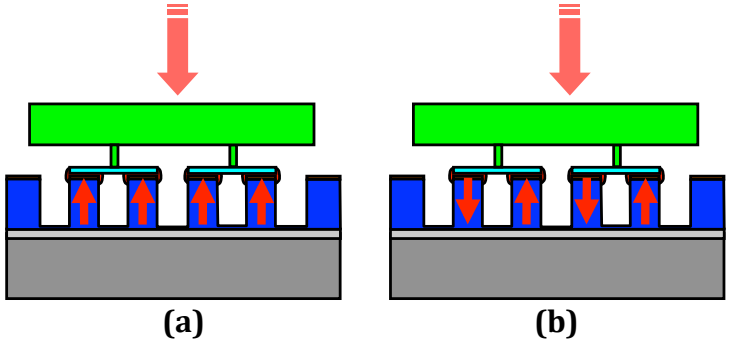

Figure 4.18: Measurement scheme for (a) ABS gap actuation (b) Shear mode actuation

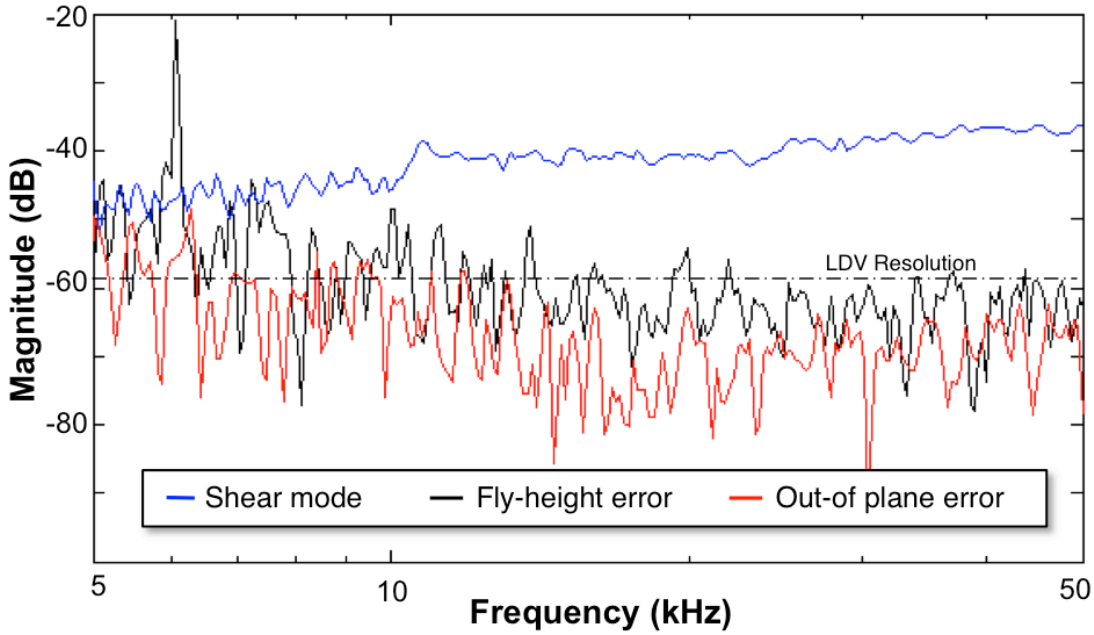

Figure 4.19: Frequency response plot of shear mode actuation (parallel mode) and its effect on fly-height and ABS gap height

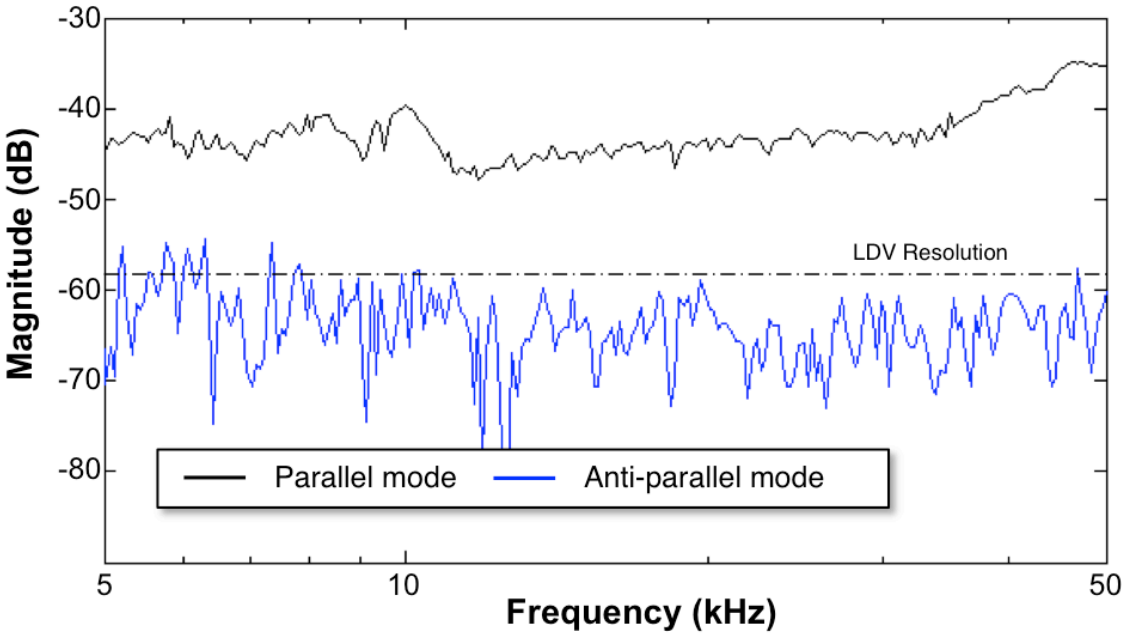

Figure 4.20: Frequency response plot comparing ABS gap actuation (parallel mode) and ABS gap error due to shear mode actuation (anti-parallel mode)

4.6 Discussion of Results

As a first working prototype, the completed device performed very close to what was predicted from the analytical model and the FEM model, as summarized in table 4.6. Recall that the analytical model predicted a shear mode displacement of 1.8 nm/V and the FEM model refined this prediction to 1.5 nm/V due to losses from deformations in the substrate and joints. The actual displacement is then expected to be even further decrease by losses due to the compliance of the epoxy bond. The actual shear mode displacement shown in Fig. 4.19 ranges from 0.4 nm/V at 5 kHz to 1.6 nm/V at 50 kHz.

Table 4.6. Comparison of prototype and predicted displacement

	Shear Mode Displacement	**ABS Gap Control Gain**
Analytical Model	1.8 nm/V	1.5 nm/V
FEM Model	1.5 nm/V	1.5 nm/V
Prototype Device	0.4 - 1.6 nm/V	0.5 - 2.0 nm/V

The upward trend with respect to frequency is rather difficult to explain because the phase remains at a constant 0±5° and, therefore, it is clear that there is no primary mechanical system mode. The general upward trend may be related to a hysteretic increase in remnant polarization of the material due to the asymmetry introduced by the DC bias voltage at the base; however, this phenomenon was not observed in the bulk PMN-PT with a DC bias, in which the frequency response magnitude was a constant 1.9 nm/V across the entire range from 5 to 50 kHz. One point to note is that there appears to be a marked transition at 10 kHz in both the shear mode and the ABS gap control mode. The magnitude of the shear mode increases and the magnitude of the gap control mode decreases at this point by roughly the same magnitude. This observation suggests that there is a difference between pillars actuated by the 15 VAC signal and the pillars actuated by the inverted 15 VAC signal. For some reason, this difference is only seen at 10 kHz and, as Fig. 4.20 reveals, this does not cause any change in the device's directionality above 10 kHz.

These results show that the device has a directionality greater than 1:10 for both actuation axes. In both cases, however, the off-axis motion measurement drops below the ±0.1 nm LDV resolution limit. This makes it very difficult to determine the directionality with the current experimental setup. The LDV resolution cannot be increased without purchasing a new LDV unit, therefore, the displacement must be increased to determine the off axis displacements; however, a 20 dB increase in actuation would require a driving signal of 150 VAC with a DC bias voltage of 180 V. The resulting actuation fields range from 1.2 to 7.2 kV/cm. Unfortunately, this covers a very large and nonlinear part of the *P-E* curve for PMN-PT and hysteretic

effects will be significant [79]. A better solution would be to fabricate a new d_{33} stack actuator to increase the stroke. This makes more sense in light of the final goal of the project, as well, in that the actual static displacement gain needs to be increased for the second prototype.

Chapter 5

Conclusion

Single stage actuation has been used in hard disk drives for over 50 years. On this timescale, dual-stage actuation definitely appears to be a very undeveloped technology. At one point, the single stage actuator went through a development process through which it was finally transformed from a linear to a rotational swinging actuator. One might imagine a similar change on the horizon for suspension-based actuators. And indeed, the case was made in chapter 2 that slider and head-based actuators offer significant performance benefits from an optimal control standpoint, without even considering the manifold robustness issues associated with ever-moving suspension modes. At the beginning of chapter 3, an argument was made for directly transitioning to head-based actuation based on the potential cost benefits of wafer-level integration. Chapter 2 has already shown that head-based actuation can act as a complete replacement for suspension-based actuation. And it therefore seems inevitable that head-based actuation will eventually be adopted if areal density continues to increase according to Kryder's Law. The question which now remains is to determine what these actuators will look like and when this transition needs to take place.

Knowing that the HDD industry is changing on a month to month basis, I have attempted to develop a methodology for tackling the challenging problems associated with head-based actuation rather than merely proposing and promoting a single solution. For this reason, a large portion of chapter 2 is dedicated to a methodology for using beam elements to reconcile mechanical and servo design concepts. Chapter 3 was intended to provide a basic framework for analyzing various candidate actuation mechanisms, although, I realize it is by no means an exhaustive treatment of the subject. While the entirety of chapter 4 is dedicated to the piezoelectric quasi-shear mode actuator, the purpose of this has been to present the interesting results of this project and provide a way to think about head-based actuation as a two degree-of-freedom actuator. Certainly it is not a fully matured concept and the actuator gain will need to be increased significantly before it can be considered for productization. But perhaps this concept will inspire further innovation toward the goal of eventually incorporating head-based actuation into HDDs.

There are two directions in which the actuator gain of the piezoelectric quasi-shear mode actuator can be improved. The first is from a purely materials science perspective; if a new piezoelectric material were found which has a d_{33} constant which is 10 times that of PMN-PT and if it satisfied all of the other necessary material constraints such as temperature stability, then the device would have

sufficient static gain. The more likely scenario, however, would be that a method is developed for fabricating a sol-gel based stack of piezoelectric films with a total displacement of 20 nm/V. This would then make the quasi-shear mode actuator a viable option.

There are currently two key technological breakthroughs on the horizon: heat-assisted magnetic recording (HAMR) and bit patterned magnetic recording (BPMR). If popular technology reviews are any sort of indication, then it appears that HAMR is nearest on the horizon, perhaps by 2015 [81]. With respect to head-based actuation, these technologies have some interesting implications. First, HAMR technologies with movable spots could reduce the requirements for track-following PES. Although these moving spots would be of no advantage in terms of reading data, it would essentially add a second stage of actuation during the writing process and writing processes are generally the ones with higher PES requirements. Therefore, it is possible that HAMR will delay the need for head-based actuation several generations. At the same time, HAMR will probably add more mass to the head and the actuator force will need to be even higher. At the same time, the PES restrictions will need to be even tighter once BPMR is implemented. In the distant horizon, there are many complications and challenges ahead for head-based actuators.

A word must also be said regarding position sensing. My work and the work of many before me have suggested that sensing may actually play a more important role in reducing PES than actuator bandwidth. Specifically, it is the sampling frequency which continues to limit the performance of current HDDs. The main problem is that increasing the sampling frequency implies an increase in number of servo sectors and, consequentially, a decrease in HDD capacity. Previous work by Felix demonstrated that arbitrary sample rates can be obtained for relative PES sensing with suspension-mounted strain gauges and that this leads to a boost in performance [54]. Another option is to implement relative position error sensing with inter-sector servo bursts. A typical servo burst can require a lot of space on a disk because there is a significant amount of information contained with regard to track ID. A relative position error signal, however, does not contain all of this information and it assumes that the head has not move very far from the absolute location. The ultimate form of relative position signal would be based upon the readback signal of the bits themselves. Some work has been done to show that if the head is offset half a track from center, a continuous and reliable signal can be obtained from the difference in amplitude between the prior track and the next track, so long as there are sufficient positively magnetized bits.

HDDs are a fascinating and exciting technology, unparalleled by most other high-volume manufactured technologies with regard to their longevity and the degree to which they have been researched and developed. They are an exciting field for servo engineers because their high-volume market requires careful performance characterization with highly repeatable processes. Hence, industry has strived to continually meet the ever-increasing need for mechanical hardware and servo

methodological improvement. Hopefully, this trend will continue with head-based actuators as industry seeks to push the performance limits with increasing areal density and bitrate.

References

[1] Fischer, S., *A History of Writing*, Reaktion Books, 319-20, 2001

[2] Ibid. 270-72

[3] Hilbert, M. and P. Lopez, The World's Technological Capacity to Store, Communicate, and Compute Information, *Science*, 62, 2011

[4] Ibid. 64

[5] Fang, P., H. Qingyun, and Q. Zhaopeng, The Research on Hadoop and Cloud computing-based mass data storage model of computation, *Applied Mechanics and Materials*, 2899-902, 2012

[6] Walter, C., Kryder's Law, *Scientific American*, 32-3, 2005

[7] Wood, R., Y. Hsu, and M. Schultz, *Perpendicular Magnetic Recording Technology*, White Paper, Hitachi Global Storage Technologies, 2007

[8] Grochowski, E. and R. Hoyt, Future Trends in Hard Disk Drives, *IEEE Trans. Magn.*, 1996.

[9] Baibich, M., J. Broto, A. Fert, et al., Giant Magnetoresistance of (001)Fe/(001)Cr Magnetic Superlattices, *Physical Review Letters*, 2472-5, 1988

[10] Mamun, A., G. Guo, C. Bi, *Hard Disk Drive Mechatronics and Control*, CRC Press, 31-82, 2007

[11] Coughlin, T., High Density Hard Disk Drive Trends in the USA, *Journal of Magnetics Society of Japan*, 2001

[12] IBM, *2314 Manual*, First published 1965

[13] IBM, *3340 Winchester Manual*, First published 1973

[14] Seagate Technology, *ST 504/412 OEM Manual*, First published 1980

[15] IBM, *3390 Manual*, First published 1989

[16] Seagate Technology, *Barracuda ES.2 Serial ATA Product Manual*, 2009

[17] Kirpekar, S., D. Bogy, An Alternative to CFD: Piecewise Linear Models for Frequency Spectra of Flow Induced Drag in Hard Disk Drives, *Microsyst. Technology*, 1271-9, 2007

[18] Aruga, K., M. Suwa, K. Shimizu, T. Watanabe, A Study on Position Error Caused by Flow Induced Vibration Using Helium-Filled Hard Disk Drives, *IEEE Transactions on Magnetics*, 3750-5, 2007

[19] Heath, J., Design of a Swinging Arm Actuator for a Disk File, *IBM Journal of Research and Development*, 389-97, 1976

[20] Yen, J., K. Hallamasek, R. Horowitz, Track-Following Controller Design for a Compound Disk Drive Actuator, *Journal of Dynamic Systems, Measurement, and Control*, 391-402, 1990

[21] H. Zappe, "The 2-stage control concept for magnetic recording: Technology challenges in magnetic recording," *presented at IEEE Micro Electro Mechanical Systems*, 1990.

[22] Fujita, H., K. Gabriel, New opportunities for micro actuators, Digest of Technical Papers, *Transducers*, 14-20, 1991

[23] Mori, K., T. Munemoto, H. Otsuki, Y. Yamaguchi, K. Akagi, A Dual-Stage Magnetic Disk Drive Actuator Using A Piezoelectric Device for a High Track Density," *IEEE Trans. on Magnetics*, 5298-330, 1991.

[24] Takaishi, K., et al., Microactuator Control for Disk Drive, IEEE *Transactions on Magnetics*, 1863-6, 1996

[25] Evans, R., J. Griesbach, W. Messner, Piezoelectric Microactuator for Dual Stage Control, *Trans. on Magnetics*, 977-82, 1999

[26] Kobayashi, M., T. Yamaguchi, R. Horowitz, Track-Seeking Controller Design for Dual-Stage Actuator in Magnetic Disk Drives, *Proc. of American Control Conference*, 2610-4, 2000

[27] Naniwa et al., Low Voltage Driven Piggy-Back Actuator of Hard Disk Drives, *IEEE Micro Electro Mechanical Systems*, 45-52, 1999

[28] Soeno, Y., et al., Piezoelectric Piggy-Back Microactuator for Hard Disk Drive, *Trans. on Magnetics*, 983-87, 1999

[29] Nakamura, S., K. Suzuki, M. Ataka, K. Mukasa, An Electrostatic Microactuator for a Magnetic Head Tracking System of Hard Disk Drives, *Advances in Information Storage Systems*, 83-99, 1997

[30] Koganezawa, S., Y. Uematsu, T. Yamada, Dual-Stage Actuator System for Magnetic Disk Drives, *IEEE Trans. on Magnetics*, 988-92, 1999

[31] Jing, Y., J. Luo, W. Yang, G. Ju, Fabrication of Piezoelectric Ceramic Micro-Actuator and Its Reliability for Hard Disk Drives, *IEEE Trans. on Ultrasonics, Ferroelectrics, and Frequency Control*, 1470-6, 2004

[32] Hawwa, M., E. Fanslau, K. Young, *Shear Mode Multilayered Collocated Micro-Actuator for Dual-Stage Servo Controllers in Disk Drives*, U.S. Patent 6,704,158 BS, 2004

[33] Tang, W., V. Temesvary, J. Yao, Y.-C. Tai, D. Miu, Silicon Microactuators for Computer Disk Drives, *Japanese Journal of Applied Physics*, 350-6, 1996

[34] Horowitz, R., P. Cheung, R. Howe, Position Sensing And Control Of Electrostatically-driven Polysilicon Microactuators, *Magnetic Recording Conference*, 1995

[35] Horsley, D., N. Wongkomet, R. Horowitz, A. Pisano, Precision Positioning Using a Microfabricated Electrostatic Actuator, *Trans. on Magnetics*, 993-9, 1999

[36] Oldham, K., X. Huang, A. Chahwan, R. Horowitz, Design, Fabrication, and Control of a High-Aspect Ratio Microactuator for Vibration Supression in a Hard Disk Drive, *Proc. of the 16th IFAC*, 2005

[37] Fan, L., H. Ottensen, R. Reiley, R. Wood, Magnetic Recording Head Positioning at Very High Track Densities Using a Microactuator-Based Two-Stage Servo System, *IEEE Transactions on Industrial Electronics*, 222-33, 1995

[38] Horsley, D., A. Singh, A. Pisano, R. Horowitz, Angular Micropositioner for Disk Drives*, IEEE Micro Electro Mechanical Systems*, 454-9, 1997

[39] Kim, B., K. Chun, Fabrication of an Electrostatic Track-Following Micro Actuator for Hard Disk Drives using SOI Wafer, *J. Micromechanics and Microengineering*, 12880-9, 2001

[40] Imamura, T., T. Koshikawa, M. Katayama, Transverse Mode Electrostatic Microactuator for MEMS-Based HDD Slider, *IEEE Micro Electro Mechanical Systems*, 216-21, 1996

[41] Yanagisawa, M., *Magnetic Disc Apparatus and Magnetic Head in which a Recording/Reproduction Element is Mounted on a Slider Via a Piezoelectric Element*. U.S. Patent 6 928 722 B2, 2005

[42] Genta, G. *Vibration of Structures and Machines*. Springer, 35, 1993

[43] Oldham, K., S. Kon, R. Horowitz, Fabrication and Optimal Strain Sensor Placement in an Instrumented Disk Drive Suspension for Vibration Suppression, *Proc. 2004 American Control Conference*, 1855-61, 2004

[44] Ginsberg, J., *Mechanical and Structural Vibrations*, John Wiley and Sons, 432, 2001

[45] Hutton, D., *Fundamentals of Finite Element Analysis*, McGraw Hill, 409, 2004

[46] Pilkey, D., *Ph.D. Dissertation: Computation of a Damping Matrix for Finite Element Model Updating*, Virginia Polytechnic Institute, 1998

[47] Ginsberg, 270

[48] Ogata, K., *System Dynamics*, Pearson Prentice-Hall, 69, 1978

[49] Juvinall, R., K. Marshek, *Fundamentals of Machine Component Design*, John Wiley and Sons, 184, 2006

[50] Liu, X., J. Liu, and C. Lim, FEM and Experimental Analysis of the Actuator 'Butterfly Mode' in a Hard-Disk Drive, *Mechanical Systems and Signal Processing*, 955-964, 2003

[51] Ginsberg, 484-5

[52] Li, Y., and R. Horowitz, Design and testing of track-following controllers for dual-stage servo systems with PZT actuated suspensions, *Microsystem Technologies*, Springer, 194-205, 2002

[53] Conway, R., *M.S. Thesis: Multi-Objective Control Design for Discrete Time Periodic Systems via Convex Optimization*, University of California, Berkeley, 2008

[54] Felix, S., J. Nie, and R. Horowitz, Enhanced Vibration Suppression in Hard Disk Drives Using Instrumented Suspensions, *IEEE Transactions on Magnetics*, 5119-22, 2009

[55] Wu, L., and D. Bogy, Numerical Simulation of the Slider Air Bearing Problem of Hard Disk Drives by Two Multidimensional Upwind Residual Distribution Schemes over Unstructured Triangular Meshes, *Journal of Computational Physics*, 640-657, 2001

[56] Oldham, K., *Ph.D. Dissertation: Microdevices for Vibration Suppression in Computer Hard Disk Drives*, University of California, Berkeley, 2006

[57] Vinokur, R., Feasible Analytical Solutions for Electrostatic Parallel-Plate Actuator or Sensor, *Journal of Vibration and Control*, 359-369, 2004

[58] Parameswaran, L., C. Hsu and M. Schmidt, A Merged MEMS-CMOS Process using Silicon Wafer Bonding, *International Electron Devices Meeting*, 613-616, 1995

[59] Berlincourt, D., H. Krueger, and C. Near, *Technical Publication TP-226: Properties of Piezoelectricity Ceramics*, Morgan Electro Ceramics, Accessed online: April 14, 2012, www.morgan-electroceramics.com

[60] Heywang, W., K. Lubitz, and W. Versing, *Piezoelectricity*, Springer, 424, 2008

[61] Kueppers, H., et al., PZT Thin Films for Piezoelectric Microactuator Applications, *Sensors and Actuators*, 680-4, 2002

[62] Liu, R., Q. Wang, Q. Zhang, and L. Cross, Piezoelectric Psuedo-Shear Mode Actuator Made by L-Shape Joint Bonding, *Journal of Materials Science: Materials in Electronics*, 453-456, 1998

[63] Juvinal, 191

[64] Juang, J. and D. Bogy, Air-Bearing Effects on Actuated Thermal Pole-Tip Protrusion for Hard Disk Drives, *Journal of Tribology*, 570-8, 2007

[65] Zhao, X., B. Fang, H. Cao, Y. Guo, and H. Luo, Dielectric and Piezoelectric Performance of PMN-PT Single Crystals with Compositions Around the MPB: Influence of Composition, Poling Field and Crystal Orientation, *Materials Science and Engineering*, 254-62, 2002

[66] Benayad, A., G. Sebal, B. Guiffard, L. Lebrun, D. Guyomar, and E. Pleska, Temperature Dependance of Piezoelectric Properties of PMN-PT and PZTN-PT Single Crystals, *J. Phys. IV France*, 53-7, 2005

[67] Mitsubishi Materials Corporation, PZT SOLGEL SOLUTION for Over-1um-THICK FILMS, Accessed online: http://www.mmc.co.jp/adv/ele/english/electric5-2.html, June 2008

[68] Barrow, D., T. Petroff, R. Tandon, and M. Sayer, Characterization of thick lead zirconate titanate films fabricated using a new sol gel based process, *J. Appl. Phys.*, 876-81, 1997

[69] Tanaka, K., T. Konishis, M. Ide, and S. Sugiyama, Wafer Bonding of Lead Zirconate Titanate to Si Using an Intermediate Gold Layer for Microdevice Application, *J. Micromech. Microeng.*, 815-20, 2006

[70] Park, G., Y. Kim, K. Paek, J. Kim, J. Lee, and B. Ju, Low-Temperature Silicon Wafer-Scale Thermocompression Bonding Using Electroplated Gold Layers in Hermetic Packaging, 330-2, 2005

[71] Xu, X., B. Li, Y. Feng, J. Chu, Design, Fabrication and Characterization of a Bulk-PZT-Actuated MEMS Deformable Mirror, *J. Micromech. Microeng.*, 2439-46, 2007

[72] Seo, J., J. Park, W. Lee, Chemical Mechanical Polishing of PZT Thin Films for FRAM Applications, *Microelectronic Engineering*, 2238-42, 2006

[73] Wang, S., X. Li, K. Wakabayashi, and M. Esashi, Deep Reactive Ion Etching of Lead Zirconate Titanate Using Sulfur Hexafluoride Gas, *J. Am. Ceram. Soc.*, 1339-41, 1999

[74] Subasinghe, S., A. Goyal, and S. Tadigadapa, High Aspect Ratio Plasma Etching of Bulk Lead Zirconate Titanate, *Micromachining and Microfabrication Process Technology XI*, 61090D1-9, 2006

[75] Bustillo, J. and M. Wasilik, STS Poly/Si Etcher, *Marvell Nanofabrication Laboratory Manual*, 7.21, 2000, Accessed online: http://nanolab.berkeley.edu/labmanual/chap7/7.21sts.pdf

[76] Tanaka, K., T. Konishi, M. Ide, Z. Meng, and S. Sugiyama, Fabrication of Microdevices Using Bulk Ceramics of Lead Zirconate Titanate, *Japanese Journal of Applied Physics*, 7068-71, 2005

[77] Williams, K., K. Gupta, and M. Wasilik, Etch Rates for Micromachining Processing—Part II, *Journal of Microelectromechanical Systems*, 761-77, 2003

[78] Transene Company Inc, *Etchant/Metal Compatibility Chart*, 2010, Accessed online: http://www.transene.com/etch_compatibility.html

[79] Turik, A., A. Yesis, and L. Reznitchenko, Negative Longitudinal Electrostriction in Polycrystalline Ferroelectrics: A Nonlinear Approach, *Journal of Physics: Condensed Matter*, 4839-43, 2006

[80] Pan, W., W. Gu, D. Taylor, and L. Cross, Large Piezoelectric Effect Induced by Direct Bias in PMN:PT Relaxor Ferroelectric Ceramics, *Japanese Journal of Applied Physics*, 653-61, 1989

[81] Patel, P. How Seagate's Terabit-Per-Square-Inch Hard Drive Works: Heat-Assisted Magnetic Recording Promises 60-Terabyte Hard Disks, *Technology Review*, 2012

Appendix

Multi-Stage Beam Model Code

```
% Derivation of Plant Model Based on Finite Element Method
%
% Purpose: to create a bottom-up model of plant structural modes and
%      gain insight into the origin and nature of the plant structure.
%
%
%
% Josiah Wernow
% Computer Mechanics Lab
% UC Berkeley
%
% (copyright 2012)
%


              % \\BEGIN HEADER\\
                clear all;
                load('FreqRespFrom50To40kHz.mat'); % Load experimental data

                standardbode                    = bodeoptions;
                standardbode.Grid               = 'on';
                standardbode.FreqUnits          = 'Hz';
                standardbode.FreqScale          = 'log';
                standardbode.MagUnits           = 'dB';
                standardbode.Title.FontSize     = 14;
                standardbode.XLabel.FontSize    = 12;
                standardbode.YLabel.FontSize    = 12;
                standardbode.TickLabel.FontSize = 10;
              % \\END HEADER\\


% Fast access
MODES_TO_PLOT = [];



%%%%%%%%%%%%%%%%%%%%%%%%%%%%%%%%%%%%%%%%%%%%%%%%%%%%%%%%%%%%%%%%%%%%%%%%%%%%%%%
%  ELEMENT STRUCTURE: Define and store element structure properties
%%%%%%%%%%%%%%%%%%%%%%%%%%%%%%%%%%%%%%%%%%%%%%%%%%%%%%%%%%%%%%%%%%%%%%%%%%%%%%%

% Element (0) PIVOT

PivotProperties.SpringConstant      =           1e13; % N/m
PivotProperties.DampingConstant     =           1e1; % N-s/m
PivotProperties.RotationalDamping   =           2e-4; % N-s
PivotProperties.RotationalSpring    =           6e-1; % N/rad
PivotProperties.RotSpring           =           7e9;
PivotProperties.RotDamping          =           1e-20;



% Element (1) COILS
n = 1;

StructElement(n).Length            =            20e-3; % m
StructElement(n).Height            =            5e-3; % m
StructElement(n).Width             =            10e-3; % m
StructElement(n).Area              =
```

```
StructElement(n).Height*StructElement(n).Width; % m x m
StructElement(n).Rho               =            7850; % kg/m^3

StructElement(n).Modulus           =            200e9; % Pa
StructElement(n).Irel              =            30;
StructElement(n).MomentInertia     =
StructElement(n).Irel*1/12*(StructElement(n).Height)*(StructElement(n).Width)^3; % m^4

StructElement(n).RayleighAlpha     =            1e-8; % multiply by me
StructElement(n).RayleighBeta      =            1e-8; % multiply by ke

StructElement(n).ShearModulus      =            StructElement(n).Modulus/(2*(1+0.29)); %
From poisson ratio
StructElement(n).Jrel              =            1;
StructElement(n).RotationalMoment  =
StructElement(n).Width*StructElement(n).Height/12 *
(StructElement(n).Width^2+StructElement(n).Height^2);
StructElement(n).Eps               =            2.e23;
StructElement(n).AlphaRot          =            5e-7;
StructElement(n).BetaRot           =            5e-7;


% Element (2) ARM PART
n = 2;

StructElement(n).Length            =            25e-3; % m
StructElement(n).Height            =            2e-3; % m
StructElement(n).Width             =            5e-3; % m
StructElement(n).Area              =
StructElement(n).Height*StructElement(n).Width; % m x m
StructElement(n).Rho               =            7850; % kg/m^3

StructElement(n).Modulus           =            200e9; % Pa
StructElement(n).Irel              =            3e1;
StructElement(n).MomentInertia     =
StructElement(n).Irel*1/12*(StructElement(n).Height)*(StructElement(n).Width)^3; % m^4

StructElement(n).RayleighAlpha     =            1e-7;
StructElement(n).RayleighBeta      =            1e-7;

StructElement(n).ShearModulus      =            StructElement(n).Modulus/(2*(1+0.29)); %
From poisson ratio
StructElement(n).Jrel              =            1;
StructElement(n).RotationalMoment  =
StructElement(n).Width*StructElement(n).Height/12 *
(StructElement(n).Width^2+StructElement(n).Height^2);
StructElement(n).Eps               =            1e25;
StructElement(n).AlphaRot          =            1e-20;
StructElement(n).BetaRot           =            1e-20;


% Element (3) SUSPENSION
n = 3;

StructElement(n).Length            =            10e-3; % m
StructElement(n).Height            =            1e-3; % m
StructElement(n).Width             =            2.e-3; % m
StructElement(n).Area              =
StructElement(n).Height*StructElement(n).Width; % m x m
StructElement(n).Rho               =            7850; % kg/m^3

StructElement(n).Modulus           =            200e9; % Pa
StructElement(n).Irel              =            0.16;
StructElement(n).MomentInertia     =
StructElement(n).Irel*1/12*(StructElement(n).Height)*(StructElement(n).Width)^3; % m^4

StructElement(n).RayleighAlpha     =            1e-6;
StructElement(n).RayleighBeta      =            1e-6;

StructElement(n).ShearModulus      =            StructElement(n).Modulus/(2*(1+0.29)); %
From poisson ratio
StructElement(n).Jrel              =            1;
StructElement(n).RotationalMoment  =
```

```
StructElement(n).Width*StructElement(n).Height/12 *
(StructElement(n).Width^2+StructElement(n).Height^2);
StructElement(n).Eps                =            3.85e17;
StructElement(n).AlphaRot           =            0.4e-6;
StructElement(n).BetaRot            =            0.4e-6;


% Element (4) HEAD/GIMBAL ASSEMBLY
n = 4;

StructElement(n).Length             =            5e-3; % m
StructElement(n).Height             =            0.2e-3; % m
StructElement(n).Width              =            0.25e-3; % m
StructElement(n).Area               =
StructElement(n).Height*StructElement(n).Width; % m x m
StructElement(n).Rho                =            4100; % kg/m^3

StructElement(n).Modulus            =            370e9; % Pa
StructElement(n).Irel               =            0.45;
StructElement(n).MomentInertia      =
StructElement(n).Irel*1/12*(StructElement(n).Height)*(StructElement(n).Width)^3; % m^4

StructElement(n).RayleighAlpha      =            9e-8;
StructElement(n).RayleighBeta       =            9e-8;

StructElement(n).ShearModulus       =            StructElement(n).Modulus/(2*(1+0.29)); %
From poisson ratio
StructElement(n).Jrel               =            1;
StructElement(n).RotationalMoment   =
StructElement(n).Width*StructElement(n).Height/12 *
(StructElement(n).Width^2+StructElement(n).Height^2);
StructElement(n).Eps                =            1.3e21;
StructElement(n).AlphaRot           =            1e-20;
StructElement(n).BetaRot            =            1e-20;


LengthStructElement = length(StructElement);




%%%%%%%%%%%%%%%%%%%%%%%%%%%%%%%%%%%%%%%%%%%%%%%%%%%%%%%%%%%%%%%%%%%%%%%%%%%%%%%
%  ELEMENT ASSEMBLY: Assemble element property matrices
%%%%%%%%%%%%%%%%%%%%%%%%%%%%%%%%%%%%%%%%%%%%%%%%%%%%%%%%%%%%%%%%%%%%%%%%%%%%%%%

for i = 1:LengthStructElement
    L       = StructElement(i).Length;
    A       = StructElement(i).Area;
    r       = StructElement(i).Rho;
    E       = StructElement(i).Modulus;
    Iz      = StructElement(i).MomentInertia;
    Alpha   = StructElement(i).RayleighAlpha;
    Beta    = StructElement(i).RayleighBeta;

    [me ce ke]      =   assemble_element(L,A,r,E,Iz,Alpha,Beta,1);

    StructElement(i).me = me; StructElement(i).ke = ke; StructElement(i).ce = ce;


    L       = StructElement(i).Length;
    r       = StructElement(i).Rho;
    G       = StructElement(i).ShearModulus;
    J       = StructElement(i).RotationalMoment*StructElement(i).Jrel;
    Eps     = StructElement(i).Eps;
    Alpha   = StructElement(i).AlphaRot;
    Beta    = StructElement(i).BetaRot;

    [mrot crot krot]      =   assemble_torsion(L,r,G,J,Eps,Alpha,Beta,1);

    StructElement(i).mrot = mrot; StructElement(i).krot = krot; StructElement(i).crot =
crot;
```

```
end


%%%%%%%%%%%%%%%%%%%%%%%%%%%%%%%%%%%%%%%%%%%%%%%%%%%%%%%%%%%%%%%%%%%%%%%%%%%%
%  GLOBAL ASSEMBLY: Assemble global property matrices
%%%%%%%%%%%%%%%%%%%%%%%%%%%%%%%%%%%%%%%%%%%%%%%%%%%%%%%%%%%%%%%%%%%%%%%%%%%%

% Pack me, ce and ke into matrix X
    for i = 1:LengthStructElement
        X(:,:,i)    = [StructElement(i).me StructElement(i).ce StructElement(i).ke];
        Xrot(:,:,i) = [StructElement(i).mrot StructElement(i).crot
StructElement(i).krot];
    end

    [mG cG kG]  = assemble_global(X);
    [mrotG crotG krotG] = assemble_global(Xrot);

    [mG_dsa3 cG_dsa3 kG_dsa3]  = assemble_global_dsa(X,3);
    [mG_dsa4 cG_dsa4 kG_dsa4]  = assemble_global_dsa(X,4);

% Assemble pivot model
    c_pivot = zeros(size(cG));
        c_pivot(3,3) = -PivotProperties.DampingConstant;
        c_pivot(4,4) = -PivotProperties.RotationalDamping;

    k_pivot = zeros(size(kG));
        k_pivot(3,3) = -PivotProperties.SpringConstant;
        k_pivot(4,4) = -PivotProperties.RotationalSpring;

    crot_pivot = zeros(size(crotG));
        crot_pivot(3,3) = -PivotProperties.RotDamping;

    krot_pivot = zeros(size(krotG));
        krot_pivot(3,3) = -PivotProperties.RotSpring;
        krot_pivot(4,4) = -PivotProperties.RotSpring;

    c_pivot_dsa3 = zeros(size(cG_dsa3));
        c_pivot_dsa3(3,3) = -PivotProperties.DampingConstant;
        c_pivot_dsa3(4,4) = -PivotProperties.RotationalDamping;

    k_pivot_dsa3 = zeros(size(kG_dsa3));
        k_pivot_dsa3(3,3) = -PivotProperties.SpringConstant;
        k_pivot_dsa3(4,4) = -PivotProperties.RotationalSpring;

    c_pivot_dsa4 = zeros(size(cG_dsa4));
        c_pivot_dsa3(3,3) = -PivotProperties.DampingConstant;
        c_pivot_dsa3(4,4) = -PivotProperties.RotationalDamping;

    k_pivot_dsa4 = zeros(size(kG_dsa4));
        k_pivot_dsa3(3,3) = -PivotProperties.SpringConstant;
        k_pivot_dsa3(4,4) = -PivotProperties.RotationalSpring;

% Add pivot model
    mGp = mG; % No change (massless pivot assumed)
    cGp = cG - c_pivot;
    kGp = kG - k_pivot;

    mrotGp = mrotG; % No change (massless pivot assumed)
    crotGp = crotG - crot_pivot;
    krotGp = krotG - krot_pivot;

    mGp_dsa3 = mG_dsa3; % No change (massless pivot assumed)
    cGp_dsa3 = cG_dsa3 - c_pivot_dsa3;
    kGp_dsa3 = kG_dsa3 - k_pivot_dsa3;

    mGp_dsa4 = mG_dsa4; % No change (massless pivot assumed)
    cGp_dsa4 = cG_dsa4 - c_pivot_dsa4;
    kGp_dsa4 = kG_dsa4 - k_pivot_dsa4;


%%%%%%%%%%%%%%%%%%%%%%%%%%%%%%%%%%%%%%%%%%%%%%%%%%%%%%%%%%%%%%%%%%%%%%%%%%%%
%  SOLUTION: Formulate transfer function, G, in Laplace domain
```

```
%%%%%%%%%%%%%%%%%%%%%%%%%%%%%%%%%%%%%%%%%%%%%%%%%%%%%%%%%%%%%%%%%%%%%%%%%%%%%%%

% Global GDE Matrix
    syms s;
    P = s^2*mGp + s*cGp + kGp;
    Prot = s^2*mrotGp + s*crotGp + krotGp;

    % DSA 3&4 Matrices
    P_dsa3 = s^2*mG_dsa3 + s*cG_dsa3 + kG_dsa3;
    P_dsa4 = s^2*mG_dsa4 + s*cG_dsa4 + kG_dsa4;

% Select where vi and thetai nodes are located
    index_v     = 1:2:2*(length(StructElement)+1);
    index_theta = 2:2:2*(length(StructElement)+1);

% Assemble global Q vectors (for each transfer function)

    %---------------------------
    % VCM => PES (states 1,2)
    %---------------------------
        V1 = 1;
        M1 = 0;
        T1 = 1;
        T5 = 0;

        Qvcm(1:length(mG),1)=0; Qvcm(1,1)=V1; Qvcm(2,1)=M1;
        Tvcm(1:length(mrotG),1)=0; Tvcm(1,1)=T1; Tvcm(5,1)=T5;

    %---------------------------
    % MA => PES (states 5,6b)
    %---------------------------
        V3 = 0;
        M3 = 1;
        T3 = 0;

        Qma(1:length(mG_dsa3),1)=0; Qma(5,1)=V3; Qma(6,1)=-M3; Qma(7,1)=M3;
        Tma(1:length(mrotG),1)=0; Tma(5,1)=T3;

    %---------------------------
    % Slider => PES (states 7,8b)
    %---------------------------
        V4 = 1;
        M4 = 1;
        T4 = 0;

        Qslider(1:length(mG_dsa4),1)=0; Qslider(7,1)=V4; Qslider(8,1)=-M4;
Qslider(9,1)=M4;
        Tslider(1:length(mrotG),1)=0; Tslider(7,1)=T4;

    %---------------------------
    % Windage => PES (states 9,10)
    %---------------------------
        V5 = -1;
        M5 = 0;
        T5 = 0;

        Qw(1:length(mG),1)=0; Qw(9,1)=V5; Qw(10,1)=M5;
        Tw(1:length(mrotG),1)=0; Tw(9,1)=T5;



% Assemble reduced global P and Q matrices
    P_reduced = P;
    Prot_reduced = Prot;

    Qvcm_reduced = Qvcm;
    Tvcm_reduced = Tvcm;
    Qma_reduced = Qma;
    Tma_reduced = Tma;
    Qslider_reduced = Qslider;
    Tslider_reduced = Tslider;
    Qw_reduced = Qw;
    Tw_reduced = Tw;
```

```
% Solve FLEX-SHEAR equation by reduced row echelon form
    vcm_solution = rref([P_reduced Qvcm_reduced]);     q_vcm = vcm_solution(1:end,end);
    ma_solution = rref([P_dsa3 Qma_reduced]);     q_ma = ma_solution(1:end,end);
    slider_solution = rref([P_dsa4 Qslider_reduced]);     q_slider =
slider_solution(1:end,end);
    w_solution = rref([P_reduced Qw_reduced]);     q_w = w_solution(1:end,end);

    [n,d]=numden(vpa(q_vcm(end-1,1),30)); RF=1; num=sym2poly(n/RF); den=sym2poly(d/RF);
    Gvcm_flex = tf(num,den);

    [n,d]=numden(vpa(q_ma(end-1,1),30)); RF=1; num=sym2poly(n/RF); den=sym2poly(d/RF);
    Gma_flex = tf(num,den);

    [n,d]=numden(vpa(q_slider(end-1,1),30)); RF=1; num=sym2poly(n/RF);
den=sym2poly(d/RF);
    Gslider_flex = tf(num,den);

    [n,d]=numden(vpa(q_w(end-1,1),30)); RF=1; num=sym2poly(n/RF); den=sym2poly(d/RF);
    Gw_flex = tf(num,den);



% Solve TORSION equation by reduced row echelon form
    vcm_solution = rref([Prot_reduced Tvcm_reduced]);     nu_vcm =
vcm_solution(1:end,end);
    ma_solution = rref([Prot_reduced Tma_reduced]);     nu_ma = ma_solution(1:end,end);
    slider_solution = rref([Prot_reduced Tslider_reduced]);     nu_slider =
slider_solution(1:end,end);
    w_solution = rref([Prot_reduced Tw_reduced]);     nu_w = w_solution(1:end,end);

    [n,d]=numden(vpa(nu_vcm(end-1,1),30)); RF=1e200; num=sym2poly(n/RF);
den=sym2poly(d/RF);
    Gvcm_torsion = tf(num,den);

    [n,d]=numden(vpa(nu_ma(end-1,1),30)); RF=1e200; num=sym2poly(n/RF);
den=sym2poly(d/RF);
    Gma_torsion = tf(num,den);

    [n,d]=numden(vpa(nu_slider(end-1,1),30)); RF=1e200; num=sym2poly(n/RF);
den=sym2poly(d/RF);
    Gslider_torsion = tf(num,den);

    [n,d]=numden(vpa(nu_w(end-1,1),30)); RF=1e200; num=sym2poly(n/RF);
den=sym2poly(d/RF);
    Gw_torsion = tf(num,den);



%%



%%%%%%%%%%%%%%%%%%%%%%%%%%%%%%%%%%%%%%%%%%%%%%%%%%%%%%%%%%%%%%%%%%%%%%%%%%%%%%%
%  MODE SHAPE: Create a plot of the resultant beam shape (for VCM)
%%%%%%%%%%%%%%%%%%%%%%%%%%%%%%%%%%%%%%%%%%%%%%%%%%%%%%%%%%%%%%%%%%%%%%%%%%%%%%%


% Solve FLEX-SHEAR equation from VCM to each node
    for i=1:length(q_vcm)
        node = i;
        [n,d]=numden(vpa(q_vcm(node,1),30));

        reduction_factor = 1;%1*10^(228+39); % Use reduction factor to rescale num/den
        num = sym2poly(n/reduction_factor); den = sym2poly(d/reduction_factor);

        Gvcm_flex_full(i,1) = tf(num,den);
    end

Gvcm_flex_zeros = zero(Gvcm_flex); Gvcm_flex_poles = pole(Gvcm_flex);
```

```
imag_poles  = imag(Gvcm_flex_poles(find(imag(Gvcm_flex_poles))));
f_poles     = imag_poles(1:2:end);
imag_zeros  = imag(Gvcm_flex_zeros(find(imag(Gvcm_flex_zeros))));
f_zeros     = imag_zeros(1:2:end);

offset = 0.999; %bump over slightly for numberical stability
f = offset*1/(2*pi)*[f_poles(end:-1:1)];%;f_zeros(end:-1:1)];
%f = f_zeros(1:end)/2/pi; %selected mode

plot_mode = MODES_TO_PLOT; %see top
n_modes_to_plot = length(plot_mode);
t_ii = [0:pi/6:2*pi]; % Time points at which to plot


PlotColor = 'krgbmcyyyyyyyyyy';
if n_modes_to_plot>0
    figure(912); clf(912);
end

for n=1:n_modes_to_plot

    mode = plot_mode(n);
    figure(912); subplot(n_modes_to_plot,1,n); hold on; grid on;
    xlabel('Distance along actuator length (m)');
    ylabel('Normalized displacement (m/Adc)');

    qi          = freqresp(Gvcm_flex_full,f(mode),'Hz');
    qi_mag      = abs(qi);
    qi_pha      = angle(qi);

    %vi     = qi(1:2:end);
    %thetai =  qi(2:2:end);

    for ii=1:length(index_v)
        vii(ii,:)     = qi_mag(index_v(ii))*cos(t_ii+qi_pha(index_v(ii)));
    end

    for ii=1:length(index_theta);
        thetaii(ii,:)  = qi_mag(index_theta(ii))*cos(t_ii+qi_pha(index_theta(ii)));
    end

    for k=1:length(t_ii) % Plot for each time step

        x0=0; x=[];v=[];

        vi = vii(:,k);
        thetai = thetaii(:,k);

        for i=1:length(StructElement)
            L = StructElement(i).Length;
            x_rel = [0:1/100:1].*L;

            for j=1:length(x_rel)
                a0          = vi(i);
                a1          = thetai(i);
                a2          = -(3*vi(i) - 3*vi(i+1) + 2*L*thetai(i) + L*thetai(i+1))/L^2;
                a3          = (2*vi(i) - 2*vi(i+1) + L*thetai(i) + L*thetai(i+1))/L^3;
                v_x(j)      = a0 + a1*x_rel(j) + a2*x_rel(j)^2 + a3*x_rel(j)^3;
            end

            x = [x x_rel+x0];
            v = [v v_x];
            x0 = x0 + L;
        end

        plot(x,v,'Color',[1,1,1]-k/length(t_ii).*[1,1,1]);%,'Color',PlotColor(mode));
    end

end
```

```
% Stabilize FLEX modes by removing unstable poles and fixing the gain
[z,p,k] = zpkdata(Gw_flex);p_s=p{1}(find(p{1}<0));p_u=p{1}(find(p{1}>0));Gw_flex_s =
zpk(z,p_s,k/prod(p_u));
[z,p,k] = zpkdata(Gvcm_flex);p_s=p{1}(find(p{1}<0));p_u = p{1}(find(p{1}>0));Gvcm_flex_s
= zpk(z,p_s,k/prod(p_u));
[z,p,k] = zpkdata(Gma_flex);p_s=p{1}(find(p{1}<0));p_u = p{1}(find(p{1}>0));Gma_flex_s =
zpk(z,p_s,k/prod(p_u));
[z,p,k] = zpkdata(Gslider_flex);p_s=p{1}(find(p{1}<0));p_u =
p{1}(find(p{1}>0));Gslider_flex_s = zpk(z,p_s,k/prod(p_u));

% Stabilize TORSION modes by removing unstable poles (manually adjust gain)
[z,p,k] = zpkdata(Gw_torsion);p_s=p{1}(find(p{1}<0));Gw_torsion_s = zpk(z,p_s,k);
[z,p,k] = zpkdata(Gvcm_torsion);p_s=p{1}(find(p{1}<0));Gvcm_torsion_s = zpk(z,p_s,k);
[z,p,k] = zpkdata(Gma_torsion);p_s=p{1}(find(p{1}<0));Gma_torsion_s = zpk(z,p_s,k);
[z,p,k] = zpkdata(Gslider_torsion);p_s=p{1}(find(p{1}<0));Gslider_torsion_s =
zpk(z,p_s,k);


[z,p,k] =
zpkdata(Gw_torsion);p_s=p{1}(find(p{1}<0));p_u=p{1}(find(p{1}>=0));Gw_torsion_s=zpk(z,[p_
s;-p_u],k);
[z,p,k] =
zpkdata(Gvcm_torsion);p_s=p{1}(find(p{1}<0));p_u=p{1}(find(p{1}>=0));Gvcm_torsion_s =
zpk(z,[p_s;-p_u],k);
[z,p,k] =
zpkdata(Gma_torsion);p_s=p{1}(find(p{1}<0));p_u=p{1}(find(p{1}>=0));Gma_torsion_s =
zpk(z,[p_s;-p_u],k);
[z,p,k] =
zpkdata(Gslider_torsion);p_s=p{1}(find(p{1}<0));p_u=p{1}(find(p{1}>=0));Gslider_torsion_s
= zpk(z,[p_s;-p_u],k);



%%%%%%%%%%%%%%%%%%%%%%%%%%%%%%%%%%%%%%%%%%%%%%%%%%%%%%%%%%%%%%%%%%%%%%%%%%%%
%  AMPLIFIER DYNAMICS: Model current amplifier circuit
%%%%%%%%%%%%%%%%%%%%%%%%%%%%%%%%%%%%%%%%%%%%%%%%%%%%%%%%%%%%%%%%%%%%%%%%%%%%

s = tf('s');


    %---------------------------
    % VCM => PES (states 1,2)
    %---------------------------

        % Power amplifier dynamics (CT)
           Tamp    = 15e-6;50.0e-6; % (seconds)     Time constant of amplifier
           Td      = 1e-8;1.5e-6; % (seconds)    Computational delay
           Pc      = 1/((Tamp)*s+1)*exp(-(Td)*s);


        % Sample Time (DT)
            N_sectors   = 800;1.0e3;
            Disk_RPM    = 10e3; % kRPM
            Ts          = 60/(N_sectors*Disk_RPM); % Sample Time


%%%%%%%%%%%%%%%%%%%%%%%%%%%%%%%%%%%%%%%%%%%%%%%%%%%%%%%%%%%%%%%%%%%%%%%%%%%%
%  CALIBRATE SYSTEM: Calibrate to reasonable SS gains from literature
%%%%%%%%%%%%%%%%%%%%%%%%%%%%%%%%%%%%%%%%%%%%%%%%%%%%%%%%%%%%%%%%%%%%%%%%%%%%

        %//////////////////////////////////////////////////////////////////////
        %////////////// DON'T CHANGE THESE VALUES! ///////////////////////////////
        %//////////////////////////////////////////////////////////////////////
        % Calibrate (constant) values for actuator magnitude
            cw          =   13.7e3*10^(-15/20); %   -> source: @ 10^0 rad/s, Kirpekar_01
        %                           %       5,400 RPM corresponds to:
        %                           %         1 sigma ~= 5nm (14dB)
        %                           %    so we can calibrate 10,000 RPM to
        %                           %    be 1 sigma = 14dB+10dB = 24 dB =
        %                           %    16nm in open loop (or 48nm
        %                           %    @3sigma)
        %                           %    windage constant gain response of
```

```
%                           %    14dB/unit variance input (i.e. sigma~=5nm)
%                           %         RPM        cw      3-sigma
%                           %       10,000      6.9e3      48 nm
%                           %       15,000      10.5e3     99 nm
%                           %       20,000      13.7e3    168 nm
%////////////////////////////////////////////////////////////////////////////
    cvcm        = 1.4962e7*10^(-80/20); %   -> source: @ 200Hz, Nie_01 reports:
%                           %         0dB measured gain w/ LDV gain=500nm/V
%                           %         so calibrate 500nm/V @ 200Hz with a
%                           %         40dB/decade double-integrator drop
%////////////////////////////////////////////////////////////////////////////
    cma         =   6.9e3*10^(-250/20);  %  -> source: Kobayashi_01 reports
%                           %         measured PZT suspension actuator with
%                           %         static gain of 300nm/V
%////////////////////////////////////////////////////////////////////////////
    cslider     =   1.3e3*10^(-285/20);  %  -> source: results of Oldham_01
%                           %         where he reports a stroke of 24um/V
%////////////////////////////////////////////////////////////////////////////
%////////////////////////////////////////////////////////////////////////////



% HDD Gains
    kw          = (10/10)^2*  (1.0)*cw;    % [nm]/unit variance @ 1 rad/s
    kvcm        =   (500)*cvcm;     % nm/Vac @ 200Hz [calibrated value]
    kma         =   (300)*cma;      % nm/V [calibrated value]
    kslider     =   (25e3)*cslider; % nm/V [calibrated value]

Gw_flex_s=kw*Gw_flex_s;Gvcm_flex_s=kvcm*Gvcm_flex_s;Gma_flex_s=kma*Gma_flex_s;Gslider_fle
x_s=kslider*Gslider_flex_s;

Gw_torsion_s=kw*Gw_torsion_s;Gvcm_torsion_s=kvcm*Gvcm_torsion_s;Gma_torsion_s=kma*Gma_tor
sion_s;Gslider_torsion_s=kslider*Gslider_torsion_s;

% Torsion mode (determined by R/W element position/geometry, 12:1)
    stable_torsion_ratio = -12;

%%%%%%%%%%%%%%%%%%%%%%%%%%%%%%%%%%%%%%%%%%%%%%%%%%%%%%%%%%%%%%%%%%%%%%%%%%%%
%  STATE SPACE MODAL FORM: Perform a modal decomposition
%%%%%%%%%%%%%%%%%%%%%%%%%%%%%%%%%%%%%%%%%%%%%%%%%%%%%%%%%%%%%%%%%%%%%%%%%%%%

G_flex              = [Gw_flex_s Gvcm_flex_s Gma_flex_s Gslider_flex_s];
G_flex_modal        = canon(G_flex,'modal');

G_torsion           = stable_torsion_ratio*[Gw_torsion_s Gvcm_torsion_s Gma_torsion_s
Gslider_torsion_s];
G_torsion_modal     = canon(G_torsion,'modal');

G_ct(1)    = (G_flex_modal(1,1)+G_torsion_modal(1,1));
G_ct(2:4)  = Pc*(G_flex_modal(1,2:4)+G_torsion_modal(1,2:4));

G_dt    = c2d(G_ct,Ts,'zoh');

% Verify that the VCM transfer function is correct
figure(990);clf(990);bode(G_ct(2),'r',{2*pi*1e2,2*pi*1e6},standardbode); hold on;

% View torsion component
figure(990);bode(G_torsion(2),'--g')

% Check final discrete time system
figure(990);bode(G_dt(2),'k');



%%%%%%%%%%%%%%%%%%%%%%%%%%%%%%%%%%%%%%%%%%%%%%%%%%%%%%%%%%%%%%%%%%%%%%%%%%%%
%  EXPERIMENTAL DATA: Compare with real experimental data
%%%%%%%%%%%%%%%%%%%%%%%%%%%%%%%%%%%%%%%%%%%%%%%%%%%%%%%%%%%%%%%%%%%%%%%%%%%%
%%
Experimental_Gain_Offset_dB = 82-25; %dB

freq=o2i1x;      %convert the linear space frequncy to log scale frequncy.
lin_mag=abs(o2i1);          %get the linear magnitude of frequncy response.
phase_angle=angle(o2i1)*180/3.14159;    %compute the phase angle of frequncy response.
```

```
figure(991);clf(991); subplot(2,1,1);
dB_mag=20*log(lin_mag)/log(10)+Experimental_Gain_Offset_dB;

data_end = length(freq);

dB_mag_reduced = dB_mag(1:data_end);
freq_reduced = freq(1:data_end);
phase_reduced=phase_angle(1:data_end);

semilogx(freq_reduced,dB_mag_reduced,'k','LineWidth',1.);hold on;
title('Magnitude-frequency response');grid
on;ylabel('Magnitude/dB');xlabel('frequency/log(f)');
subplot(2,1,2);
%semilogx(freq,phase_angle); hold on;
semilogx(freq_reduced,180/pi*unwrap(pi/180*phase_reduced,1.65*pi),'k','LineWidth',1.);
hold on;%1.85*pi)); hold on;
title('Phase angle-frequency response'); grid on;ylabel('Phase angle/');

[M_ct P_ct]=bode(G_ct(2),freq_reduced*2*pi);
[M_torsion P_torsion]=bode(G_torsion(2),freq_reduced*2*pi);
[M_dt P_dt]=bode(G_dt(2),freq_reduced*2*pi);

M_ct_2(1:size(M_ct,3),1,1)=20*log(M_ct(1,1,1:end))/log(10);
M_torsion_2(1:size(M_torsion,3),1,1)=20*log(M_torsion(1,1,1:end))/log(10);
M_dt_2(1:size(M_dt,3),1,1)=20*log(M_dt(1,1,1:end))/log(10);

P_ct_2(1:size(P_ct,3),1,1)=P_ct(1,1,1:end);
P_torsion_2(1:size(P_torsion,3),1,1)=P_torsion(1,1,1:end);
P_dt_2(1:size(P_dt,3),1,1)=P_dt(1,1,1:end);

subplot(2,1,1);
semilogx(freq_reduced,M_ct_2,'r','LineWidth',1.0);
%semilogx(freq_reduced,M_torsion_2,'--g');
%semilogx(freq_reduced,M_dt_2,'k');

legend('Experiment','CT Plant','Torsion Mode','DT Plant');

subplot(2,1,2);
%semilogx(freq,mod(P_ct_2+180,360)-180,'r');
semilogx(freq_reduced,P_ct_2-1440,'r','LineWidth',1.0);
%semilogx(freq,P_torsion_2,'--g');
%semilogx(freq,P_dt_2,'k');
%%

%%%%%%%%%%%%%%%%%%%%%%%%%%%%%%%%%%%%%%%%%%%%%%%%%%%%%%%%%%%%%%%%%%%%%%%%%%%%
%  PLOT SYSTEM RESPONSE: Bode plots of 4 inputs to 1 output (PES)
%%%%%%%%%%%%%%%%%%%%%%%%%%%%%%%%%%%%%%%%%%%%%%%%%%%%%%%%%%%%%%%%%%%%%%%%%%%%


    %----------------------------
    % Windage => PES
    %----------------------------
        figure(992);clf(992);subplot(2,2,1);
        bode(Gw_flex_s,{2*pi*1e2,2*pi*1e6},'--m',standardbode); hold on;
        %bode(stable_torsion_ratio*Gw_torsion_s,'--c');
        bode(G_dt(1),'k');
        legend('Flexure-Shear Modes','Combined DT Plant');
        title('Response from Windage to PES');

    %----------------------------
    % VCM => PES
    %----------------------------
        figure(992);subplot(2,2,2);
        bode(Gvcm_flex_s,{2*pi*1e2,2*pi*1e6},'--m',standardbode); hold on;
        %bode(stable_torsion_ratio*Gvcm_torsion_s,'--c');
        bode(G_dt(2),'k');
        legend('Flexure-Shear Modes','Combined DT Plant');
        title('Response from VCM to PES');

    %----------------------------
    % MA => PES
    %----------------------------
```

```
    figure(992);subplot(2,2,3);
    bode(Gma_flex_s,{2*pi*1e2,2*pi*1e6},'--m',standardbode); hold on;
    %bode(stable_torsion_ratio*Gma_torsion_s,'--c');
    bode(G_dt(3),'k');
    legend('Flexure-Shear Modes','Combined DT Plant');
    title('Response from Suspension Actuator to PES');

%---------------------------
% Slider => PES
%---------------------------
    figure(992);subplot(2,2,4);
    bode(Gslider_flex_s,{2*pi*1e2,2*pi*1e6},'--m',standardbode); hold on;
    %bode(stable_torsion_ratio*Gslider_torsion_s,'--c');
    bode(G_dt(4),'k');
    legend('Flexure-Shear Modes','Combined DT Plant');
    title('Response from Slider Actuator to PES');
```

Multi-Stage Optimal Performance Code

```
% Optimal HDD Performance
%
% Purpose: to use the HDD model developed from beam elements to assess the
% nominal system closed-loop performance using stationary LQG.
%
%
%
% Josiah Wernow
% Computer Mechanics Lab
% UC Berkeley
%
% (copyright 2012)
%


              % \\BEGIN HEADER\\

                clear H;

                standardbode                    = bodeoptions;
                standardbode.Grid               = 'on';
                standardbode.FreqUnits          = 'Hz';
                standardbode.FreqScale          = 'log';
                standardbode.MagUnits           = 'dB';
                standardbode.Title.FontSize     = 14;
                standardbode.XLabel.FontSize    = 12;
                standardbode.YLabel.FontSize    = 12;
                standardbode.TickLabel.FontSize = 10;
              % \\END HEADER\\

display('       ');
display(' // CONSTRLQG Simulation //');
display('       ');


%%%%%%%%%%%%%%%%%%%%%%%%%%%%%%%%%%%%%%%%%%%%%%%%%%%%%%%%%%%%%%%%%%%%%%%%%%%%%%%
%  SIMULATION CONSTRAINTS
%%%%%%%%%%%%%%%%%%%%%%%%%%%%%%%%%%%%%%%%%%%%%%%%%%%%%%%%%%%%%%%%%%%%%%%%%%%%%%%


% Standard Deviation of Measurement Noise (wrt. PES)
    sigma_n = 0.1; % [nm]

% Actuation power constraints
    gamma_2   = 2; % V (1*sigma) --V-- (for max. VCM power)
    gamma_3   = 5; % V (1*sigma) --M-- (for max. MA power)
    gamma_4   = 5; % V (1*sigma) --S-- (for max. Slider power)
    gamma_hba = 5; % V (1*sigma)  (for power reduction)


%%%%%%%%%%%%%%%%%%%%%%%%%%%%%%%%%%%%%%%%%%%%%%%%%%%%%%%%%%%%%%%%%%%%%%%%%%%%%%%
%  SINGLE STAGE SYSTEM
%%%%%%%%%%%%%%%%%%%%%%%%%%%%%%%%%%%%%%%%%%%%%%%%%%%%%%%%%%%%%%%%%%%%%%%%%%%%%%%

display('*** SINGLE STAGE SYSTEM ***');

 Ghat = [ [1;1]*G_dt(1:2) [0; sigma_n];
          0 1 0];
Ggen1 = Ghat([1 3 2],[1 3 2]);
    L = {[1 0],[0 1]};
    R = cell(1,2);
    C = [1 0];
 type = [2 2];
    M = [0 1/gamma_2];
 prob = mobsynprob(L,R,type,C,M);

[K,cost] = constrlqg(Ggen1, 1, 1, prob);
```

```
display('       ');
display('Single Stage');three_sigma=3*cost
display('       ');


%%%%%%%%%%%%%%%%%%%%%%%%%%%%%%%%%%%%%%%%%%%%%%%%%%%%%%%%%%%%%%%%%%%%%%%%%%%%%%%
%  DUAL STAGE SYSTEM
%%%%%%%%%%%%%%%%%%%%%%%%%%%%%%%%%%%%%%%%%%%%%%%%%%%%%%%%%%%%%%%%%%%%%%%%%%%%%%%

display('*** TWO STAGE SYSTEM ***');

 Ghat = [ [1;1]*G_dt(1:3) [0; sigma_n];
          0 1 0 0;
          0 0 1 0];
Ggen2 = Ghat([1 3:4 2],[1 4 2:3]);
    L = {[1 0 0],[0 1 0],[0 0 1]};
    R = cell(1,3);
    C = [1 0 0];
 type = [2 2 2];
    M = [0 1/gamma_2    0;
         0    0      1/gamma_3];
 prob = mobsynprob(L,R,type,C,M);

[K,cost] = constrlqg(Ggen2, 1, 2, prob);

display('       ');
display('Dual Stage');three_sigma=3*cost
display('       ');


%%%%%%%%%%%%%%%%%%%%%%%%%%%%%%%%%%%%%%%%%%%%%%%%%%%%%%%%%%%%%%%%%%%%%%%%%%%%%%%
%  THREE STAGE SYSTEM
%%%%%%%%%%%%%%%%%%%%%%%%%%%%%%%%%%%%%%%%%%%%%%%%%%%%%%%%%%%%%%%%%%%%%%%%%%%%%%%

display('*** THREE STAGE SYSTEM ***');

 Ghat = [ [1;1]*G_dt [0; sigma_n];
          0 1 0 0 0;
          0 0 1 0 0;
          0 0 0 1 0];
Ggen3 = Ghat([1 3:5 2],[1 5 2:4]);
    L = {[1 0 0 0],[0 1 0 0],[0 0 1 0],[0 0 0 1]};
    R = cell(1,4);
    C = [1 0 0 0];
 type = [2 2 2 2];
    M = [0 1/gamma_2    0           0     ;
         0    0      1/gamma_3     0     ;
         0    0           0     1/gamma_4];
 prob = mobsynprob(L,R,type,C,M);

[K,cost] = constrlqg(Ggen3, 1, 3, prob);

display('       ');
display('Three Stage');three_sigma=3*cost
display('       ');


%%%%%%%%%%%%%%%%%%%%%%%%%%%%%%%%%%%%%%%%%%%%%%%%%%%%%%%%%%%%%%%%%%%%%%%%%%%%%%%
%  HEAD-BASED MICROACTUATOR
%%%%%%%%%%%%%%%%%%%%%%%%%%%%%%%%%%%%%%%%%%%%%%%%%%%%%%%%%%%%%%%%%%%%%%%%%%%%%%%

display('*** HEAD-BASED ACTUATOR ***');
k_hba               = 20; % nm/V (gain)
bandwidth_hba       = 100e3; % kHz (bandwidth)

G_hba_ct            = zpk([],[-bandwidth_hba*2*pi],k_hba*bandwidth_hba*2*pi);
G_hba_dt            = c2d(G_hba_ct,Ts,'zoh');
G_hba               = [G_dt(1:2) G_hba_dt];

 Ghat = [ [1;1]*G_hba(1:3) [0; sigma_n];
          0 1 0 0;
          0 0 1 0];
Ggen2 = Ghat([1 3:4 2],[1 4 2:3]);
```

```
    L = {[1 0 0],[0 1 0],[0 0 1]};
    R = cell(1,3);
    C = [1 0 0];
 type = [2 2 2];
    M = [0 1/gamma_2    0;
         0    0      1/gamma_hba];
 prob = mobsynprob(L,R,type,C,M);

[K,cost] = constrlqg(Ggen2, 1, 2, prob);

display('       ');
display('HBA Dual-Stage');three_sigma=3*cost
display('       ');


%%%%%%%%%%%%%%%%%%%%%%%%%%%%%%%%%%%%%%%%%%%%%%%%%%%%%%%%%%%%%%%%%%%%%%%%%%%%
%  THREE STAGE w/ HEAD-BASED ACTUATOR
%%%%%%%%%%%%%%%%%%%%%%%%%%%%%%%%%%%%%%%%%%%%%%%%%%%%%%%%%%%%%%%%%%%%%%%%%%%%

display('*** HEAD-BASED THREE STAGE SYSTEM ***');

 G_hba  = [G_dt(1:3) G_hba_dt];

 Ghat = [ [1;1]*[G_dt(1:3) G_hba_dt] [0; sigma_n];
         0 1 0 0 0;
         0 0 1 0 0;
         0 0 0 1 0];
Ggen3 = Ghat([1 3:5 2],[1 5 2:4]);
    L = {[1 0 0 0],[0 1 0 0],[0 0 1 0],[0 0 0 1]};
    R = cell(1,4);
    C = [1 0 0 0];
 type = [2 2 2 2];
    M = [0 1/gamma_2    0          0     ;
         0    0      1/gamma_3     0     ;
         0    0          0     1/gamma_hba];
 prob = mobsynprob(L,R,type,C,M);

[K,cost] = constrlqg(Ggen3, 1, 3, prob);

display('       ');
display('HBA Three-Stage');three_sigma=3*cost
display('       ');
```